Technische Universität München
TUM School of Natural Sciences

Hosing of a Long Relativistic Proton Bunch Induced by an Electron Bunch in Plasma

Tatiana Nechaeva

Vollständiger Abdruck der von der TUM School of Natural Sciences der Technischen Universität München zur Erlangung des akademischen Grades einer

Doktorin der Naturwissenschaften (Dr. rer. nat.)

genehmigten Dissertation.

Vorsitz: Prof. Dr. Andreas Weiler

Prüfer*innen der Dissertation:

1. Hon.-Prof. Dr. Allen C. Caldwell
2. Prof. Dr. Laura Fabbietti

Die Dissertation wurde am 29.11.2023 bei der Technischen Universität München eingereicht und durch die TUM School of Natural Sciences am 15.12.2023 angenommen.

Technische Universität München
TUM School of Natural Sciences

Max-Planck-Institut für Physik
(Werner-Heisenberg-Institut)

Doctoral Thesis

Hosing of a Long Relativistic Proton Bunch Induced by an Electron Bunch in Plasma

Tatiana Nechaeva

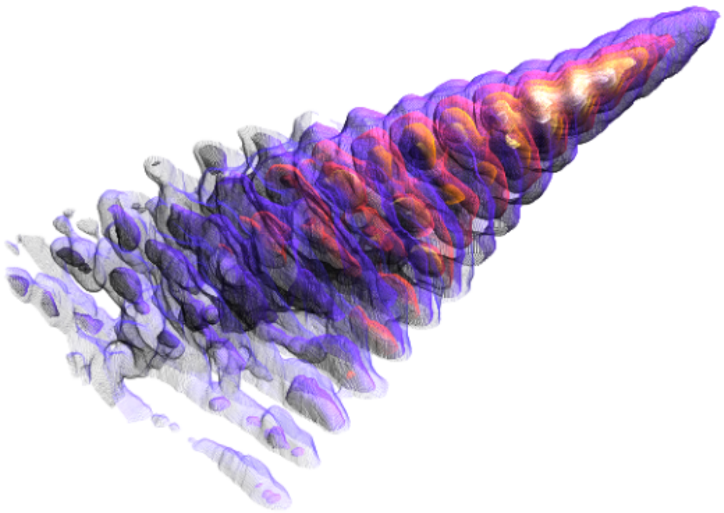

Abstract

Hosing is one of the instabilities that can develop in a beam-plasma system. It represents a fundamental mode of interaction of such a system. Hosing is discussed in different contexts across several fields of research. In plasma-based acceleration, it is a detrimental phenomenon, that negatively impacts the quality of the beams and might disrupt the acceleration process. Studying and understanding hosing is therefore important.

In this thesis, we present, to date, the most comprehensive characterization of hosing in the context of plasma-based acceleration. We report for the first time that hosing of a long, relativistic (proton) bunch that propagates in an over-dense plasma, can be induced and thus observed in a reproducible way. Hosing is induced by relative misalignment between the trajectory of a short electron bunch, hence the seed wakefields it drives, and that of the trailing proton bunch. Hosing develops simultaneously with self-modulation (SM), in perpendicular planes. With no electron bunch, SM develops as an instability and no hosing is observed, indicating that seed wakefields induce hosing. Hosing manifests itself as an oscillation of the proton bunch centroid position that grows along the bunch and the plasma, due to its resonant coupling to the wakefields. The centroid position in case of SM has no periodic pattern and remains close to the bunch propagation axis. The electron bunch drives wakefields at the plasma electron frequency, therefore the frequency of hosing is close to that of SM, both close to the plasma electron frequency, determined at two plasma electron densities, $n_{pe} = 0.96 \times 10^{14}$ cm^{-3} and $n_{pe} = 2.03 \times 10^{14}$ cm^{-3}. The development of hosing depends on the direction of misalignment, that is, when the direction is inverted, the centroid position oscillation is reflected with respect to the bunch propagation axis. As the amplitude of the seed wakefields depends on the distance from the bunch propagation axis, the amplitude of hosing depends on the electron-proton beams misalignment extent. With misalignment extents larger than 0.5 c/ω_{pe} (c/ω_{pe} – cold plasma skin depth), the amplitude of hosing decreases, following the decrease in the wakefields amplitude determined from numerical simulations. When the misalignment extent is larger than 2.5 c/ω_{pe}, SM develops as an instability and no hosing is observed. When not induced by a sufficient level of seed wakefields, hosing develops as an instability and was observed only at low plasma densities $n_{pe} \leq 0.5 \times 10^{14}$ cm^{-3}. The amplitude of hosing increases with the proton bunch density, i.e., its charge (fixed misalignment extent), as predicted by theoretical findings. We find good general agreement between hosing we observe and a theoretical model of a long-beam, early-time regime hosing, despite differences between assumptions of the model and the experimental conditions. We introduce a method to reconstruct the time-resolved 3D proton bunch charge density distribution. We apply it to the case of simultaneous development of hosing and SM. We show that the method indeed allows for reproducing the two perpendicular planes of the bunch, that is, for unambiguous observation of the two processes of interest.

Contents

Chapter 1

Introduction

First and foremost, I would like to note that all along this thesis I choose to use "we" instead of "I", to acknowledge that, despite the study presented being my work, many people have contributed to make it possible.

In this chapter, we give a brief historical overview of the conventional particle acceleration technology and outline the motivation for the plasma-based technology. We describe the principle of plasma-based accelerators and give an overview of laser-driven and particle-driven schemes. We outline the context and the motivation for the topic of the study presented here. We conclude by introducing the layout of this thesis.

1.1 Conventional acceleration technology

The history of particle acceleration begins from the end of 19th century, when the cathode ray tube was introduced [1]. In this tube, electrons emitted from a cathode are accelerated in a strong static electric field between the cathode and the anode. This illustrates the main principle of particle acceleration: interaction of charged particles with static or dynamic electromagnetic fields, that results in particles reaching higher velocities, thus, gaining more energy.

The first large-scale linear accelerators reaching MeV-range particle energies were based on the Van-der-Graaff [2] and the Cockcroft-Walton generators [3], introduced in the early 1930s. These machines represent electrostatic accelerators, where particles are accelerated in the potential difference between the two electrodes. At the same time, the first circular machines, starting from the cyclotron, were developed, in order to further increase the energies up to hundreds of MeV. This was achieved by using a high-frequency alternating voltage (denoted as radio-frequency, RF), to accelerate and circulate the particles in the accelerating structure multiple times. The particles in the cyclotron followed a spiral-like path. To reach even higher energies, cyclotrons evolved into synchrocyclotrons, and those – into synchrotrons, that are currently used. In synchrotrons, magnetic fields are applied to keep the particles circulating in a path with a fixed radius. That means, the field strength of the magnets has to increase with increasing particle energy. Synchrotrons can be used not only as accelerators, but also as storage rings for collider applications. The notable examples of synchrotrons are the Proton Synchrotron (PS, 1959) and the Super Proton Synchrotron (SPS, 1976) at CERN. With these machines, major discoveries in the Standard Model physics, such as discovery of W and Z bosons, were made. Then the 27 km-circumference Large Electron-Positron Collider (LEP) [4] at CERN started operation in 1989. In its final stage, center-of-mass collision energy of 209 GeV was reached. After LEP, the Large Hadron Collider (LHC) [5], that has the same circumference, was built. It accelerates proton bunches supplied to it by the preceding accelerator chain (that includes the PS and the SPS). Center-of-mass collision energy of up to 14 TeV is possible. At the LHC, the Higgs boson was discovered in 2012 [6], completing the Standard Model.

There still remain numerous open questions in physics, such as the nature of dark matter, matter-antimatter asymmetry etc., that might profit from further increase in particle collision energy. Current trend in particle physics is focusing on the precision of the measurements, therefore, a lepton collider could be a future machine. Hadrons are composite particles subject to strong interaction, thus, their collisions have a significant background level. Event reconstruction that includes complex hadronic cascade processes is therefore required. Leptons, on the other hand, are elementary particles, that are not subject to strong interaction. Lepton collisions thus have much clearer signatures, allowing for the desired precision measurements. The most considered (and well-studied) option for a lepton machine is an electron-positron collider. It would come with the following limitations. If the machine is to be circular, it would have a significant limitation of synchrotron radiation. The energy loss per turn is expressed as [1]:

$$\Delta E_S \propto \frac{E^4}{r_S m_0^4 c^8}, \tag{1.1}$$

where r_S is the radius of the turn and m_0 – the rest mass of the particle. Therefore, the lower the mass of the particle, the higher the energy loss. For protons, that are $\sim$ 2000 times heavier than electrons, that does not constitute a significant limitation. For example, at the LEP the center-of mass collision energy was in the GeV range, while at the LHC, with the same machine size, TeV-range energy is reached. For the electron (and positron) acceleration, if TeV energy range is desired, linear machines are preferred. So far, the largest and the most powerful linear accelerator was the 3.2 km-long Stanford Linear Collider (SLC) [7] constructed at SLAC, USA, that started operation in 1989. The electron (positron) center-of-mass collision energy of 90 GeV was reached. However, linear machines currently have a limit of the accelerating gradient of about 100 MeV/m, due to electric breakdown in RF cavities. Before a technology is developed to overcome this limitation, the only way to increase the energy of the particles is to increase the acceleration length. For example, the Compact Linear Collider (CLIC), proposed at CERN, would aim to accelerate electrons and positrons to up to 3 TeV in 48 km length, with an average accelerating field of 100 MV/m [8].

An overall limitation of the circular machines is the strength of the magnetic field required to keep the particles on their trajectory: the higher the energy (with the same machine size), the stronger the required field. That, again, results in a need of a new technology to overcome this limitation, and, until available, in the increase of the machine size. The Future Circular Collider (FCC) [9] – a 100 km-circumference ring also proposed at CERN, would first be used as an electron-positron collider (FCC-ee), with the center-of-mass collision energy of 350 GeV, and then it would accelerate hadrons to the center-of-mass energy of 100 TeV (FCC-hh).

The technological limitations, the complexity and size of the machines, and cost, of both construction and operation, result in a slowdown in the initially exponential increase of the beam energy with time (Fig. 1.1.1). Therefore, the need of new and fundamentally different concepts, e.g., plasma-based acceleration, arises. A linear particle accelerator based on this technology is a promising alternative to its conventional counterpart.

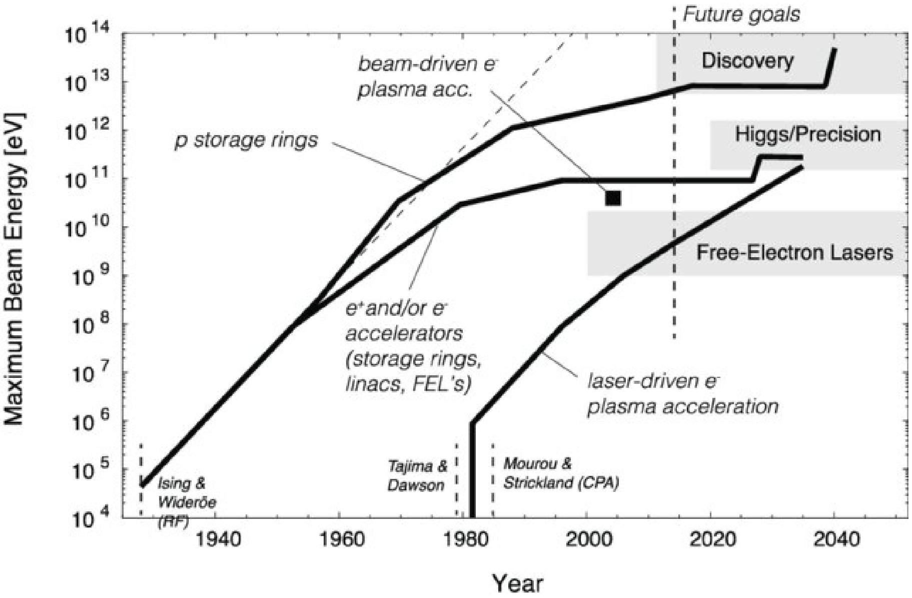

Figure 1.1.1: Livingston plot for accelerators [10], showing the maximum beam energy as a function of the construction year. Left curve shows the progress in conventional accelerators from 1920s and splits into two lines corresponding to the electron/positron (precision) machines and to the proton (discovery) machines. Right curve shows the progress in the laser-driven plasma wakefield acceleration from 1980s. Currently this technology makes it possible to accelerate electrons to multi-GeV energies. Particle-driven plasma acceleration technology is shown by the square point. Vertical dashed lines indicate future goals for the technologies displayed.

1.2 Plasma-based acceleration

The principle of plasma-based acceleration is to utilize the ability of plasma to sustain plasma electron waves, which result in generation of electric and magnetic fields. Using plasma as an accelerating medium makes it possible to overcome the breakdown limit of the conventional RF structures, as plasma is already ionized. The upper limit of the electric field that can be sustained in plasma is on the order of the wavebreaking field E_{WB} [11], defined as:

$$E_{WB} = \frac{m_e c \omega_{pe}}{e}, \tag{1.2}$$

where m_e is the electron mass, c – the speed of light, e – the elementary charge, and ω_{pe} – the plasma electron angular frequency, given by:

$$\omega_{pe} = \sqrt{\frac{n_{pe}e^2}{\epsilon_0 m_e}}. \tag{1.3}$$

In this expression, n_{pe} is the plasma electron density and ϵ_0 is the vacuum permittivity. We therefore can estimate the wavebreaking field as

$$E_{WB} \approx 96\frac{\mathrm{V}}{\mathrm{m}}\sqrt{n_{pe}[\mathrm{cm}^{-3}]}. \tag{1.4}$$

Currently, plasma-based wakefield experiments operate at n_{pe} in range of $(10^{14} - 10^{18})$ cm^{-3}, that is, the possible maximum accelerating fields are in range of (1 – 100) GV/m. Compared to the conventional accelerators, this represents an increase in accelerating field of up to three orders of magnitude. Moreover, the fields in plasma are not only accelerating, but also focusing, acting like magnets in conventional accelerators. Consequently, plasma-based accelerators could reach the same energies as their conventional counterparts, but in a smaller acceleration length. That is supposed to decrease the construction and operation costs, making these machines widely available. The applications of these accelerators range from smaller facilities for medical usage, e.g., cancer therapy, to high-energy electron sources for free-electron lasers (FELs), to accelerators for particle physics studies.

The working principle of all plasma-based accelerators is shown in Fig. 1.2.1. The setup consists of a driver, that can be either an ultra-short, high-intensity laser pulse, or a short relativistic bunch of negatively or positively charged particles (Fig. 1.2.1, red cylinder). In order to efficiently drive wakefields, the longitudinal size of the driver has to be smaller than the plasma wavelength $\sigma_z < \lambda_{pe} = 2\pi c/\omega_{pe}$ [13]. The transverse size of the driver has to be smaller than the cold plasma skin depth $\sigma_r < c/\omega_{pe}$, in order to avoid the possible onset of current filamentation instability (CFI, see Section 2.3.3). The driver, entering the initially neutral plasma, generates a transverse force and either radially expels (laser pulse, negatively charged particle bunch) or attracts (positively charged particle bunch) the light plasma electrons (blue minus signs) towards its propagation axis. In case of a laser pulse, this force is ponderomotive, while in case of a particle bunch it is a space-charge force. In

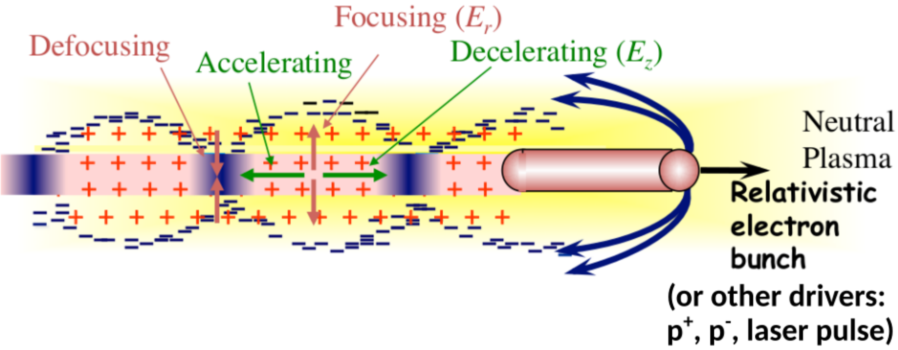

Figure 1.2.1: Schematic of a plasma-based acceleration [12]. The driver, here – a short relativistic electron bunch, enters an initially neutral plasma and expels plasma electrons from its propagation axis, due to the space-charge force effect. These electrons are then attracted back to the axis by the remaining there positively-charged ions, and then, due to the negative charge density on axis and the sufficient kinetic energy, the electrons cross the axis and continue moving. This leads to a periodic oscillation of the plasma electrons around the driver propagation axis. Due to the resulting charge separation, there appear high-amplitude electric and magnetic fields – wakefields.

this approach, we assume that the plasma ions are immobile on the time scales considered, due to their higher mass. When the plasma electrons are expelled from the propagation axis of the driver, there appears a surplus of ions on-axis (red plus signs). This results in the uncompensated positive charge that, after the driver has passed, attracts the plasma electrons back to the axis. When these electrons reach the axis, the negative charge density on-axis increases, and, due to their kinetic energy, the electrons continue to move and cross the axis. Overall, this leads to a periodic oscillation around the driver propagation axis at the plasma electron frequency. In the co-moving frame of the driver, a plasma wave is formed behind it. The "bubbles" (Fig. 1.2.1) represent the accelerating and focusing structures, in which, due to charge separation, high-amplitude electric and magnetic fields (wakefields) appear. The longitudinal component of the wakefields is accelerating and decelerating, transverse – focusing and defocusing. A witness bunch to be accelerated (not shown) has to be injected into the focusing and accelerating phase of the wakefields.

In plasma-based acceleration, plasma acts as a medium that transfers energy from the driver to the witness bunch, thus, the energy of the driver sets a limitation of the maximum energy gain. That is due to the energy depletion of the driver [14], when its phase velocity decreases and its particles transition to the defocusing phase of the wakefields. Those, along with the preservation of the witness bunch quality (low energy spread and emittance, etc.) are the main challenges of plasma-based acceleration.

1.2.1 Laser-driven wakefield acceleration

The first proposal of a laser-driven wakefield accelerator (LWFA), presented by Tajima and Dawson in 1979 [15], started the development of all plasma-based acceleration schemes. It suggested that the plasma waves, or wakefields, could be excited by the ponderomotive force of a laser pulse. The injected electrons are trapped and accelerated by the wakefields, with multi-GeV/m accelerating gradients. Until sufficiently short laser pulses became available, large-amplitude wakefields were resonantly driven by the beating of two long laser pulses [16–18] or by the pulses that were self-modulated through Raman scattering [14]. Those were the first experimental realizations of the laser-driven acceleration schemes. They showed acceleration of the externally injected electrons in gradients of about 0.7 GeV/m. After the demonstration of Chirped Pulse Amplification (CPA) by Strickland and Mourou in 1985 [19], short, high-intensity laser pulses were made available. Such laser pulses became the most frequently used drivers. In 1995, Modena et al. [20] reported reaching peak accelerating fields of 100 GV/m for acceleration of electrons. In 2004, electron beams with a finite energy spread of a few percent were produced [21–23]. Reducing normalized transverse emittance of the electron bunches with energy of up to 0.25 GeV to 0.2 π mm·mrad was demonstrated [24]. In 2014, acceleration of 6 pC of electrons to 4.2 GeV in 9 cm of plasma, that is, accelerating gradient of about 47 GeV/m, and a final rms energy spread of 6% were demonstrated at the Lawrence Berkeley National Laboratory (LBNL) [25]. This was followed by a further increase in the energy of electrons to 7.8 GeV over a plasma length of 20 cm (peak power of the drive laser pulse is 0.85 PW) [26]. Staging experiments were performed, demonstrating acceleration of electrons in two independent laser-driven stages [27]. Active research is ongoing on the use of the LWFA for generation of electron beams for use in synchrotron radiation sources or FELs [28–30].

Several laser-driven acceleration facilities using multi-PW, tens or hundreds of J laser pulses, are planned to be implemented as a part of the Extreme Light Infrastructure

(ELI) project [31, 32]. Besides from pushing the laser energy frontier, novel high repetition rate laser systems with lower energies are studied for the improvement of the stability of the laser-driven schemes [33].

Overall, the research in LWFA is quite widespread and promising due to the relatively small size and low cost of the facilities, compared to those of the conventional machines.

1.2.2 Particle-driven wakefield acceleration

In 1985, Chen et al. proposed to use a relativistic electron bunch to drive the wakefields [34]. This concept was demonstrated experimentally by Rosenzweig et al. in 1988 at Argonne National Laboratories [35]. In 2007 at SLAC, Blumenfeld et al. [36] showed the doubling of the energy of some witness electrons from 42 GeV to 84 GeV in 85 cm of plasma. This corresponds to the average accelerating gradient of 49 GeV/m. The energy gain of the electrons is comparable to that gained over ~ 3 km of propagation in the conventional accelerator that produced the drive bunch.

Several studies on energy spread minimization [21–23], emittance preservation [37] and efficiency of the acceleration process [38, 39] were performed.

As mentioned earlier, the energy gained by the witness bunch is limited by the energy of the driver. Most of the currently used laser systems provide pulses with up to tens of J of energy, similarly to the available electron beam drivers. Overall, the most common energy limit for these driver types is ~ 100 J. In order to reach higher energy of the witness bunch, having multiple independently-driven synchronous stages is required. This is a very challenging task [40]. Therefore, higher driver energies are desired.

In 2009, Caldwell et al. proposed acceleration of electrons up to 600 GeV in a single-stage 600 m of plasma with a high-energy relativistic proton bunch as a driver [41]. For charged particle bunches, the energy scales with the rest mass of the composing particles. Therefore, the proton bunches could carry quite high energies, tens or hundreds of kJ. For example, the proton bunches produced at the SPS, with an energy of 400 GeV per proton and population of $N_b = 3 \cdot 10^{11}$ particles, carry ~ 19.2 kJ, and the bunches produced at the LHC, with the nominal energy of 7 TeV per proton and $N_b = 1.2 \cdot 10^{11}$ particles, carry ~ 135 kJ. Such proton bunches can in principle drive wakefields for hundreds of meters in a single stage [42]. This is the main motivation for the Advanced Wakefield Experiment (AWAKE) at CERN: to use the SPS-produced proton bunch as driver. In 2018, AWAKE was able to accelerate electron bunches from 19 MeV to 2 GeV in 10 m of plasma [43]. As the bunches produced by the SPS are long (~ 6 cm) compared to the $\lambda_{pe} \sim 3$ mm, in order to effectively drive large-amplitude wakefields, AWAKE relies on self-modulation (SM) of a long proton bunch transforming it into a train of sufficiently short microbunches. In order to obtain reproducible outcome from event to event, SM is seeded, either with a relativistic ionization front (RIF) [44] or with a short electron bunch [45]. More details about the mechanism of SM, the seeding schemes used, their advantages and disadvantages are given in Section 2.3.1, more details about the current AWAKE experimental setup and studies performed – in Chapter 3.

1.3 Hosing in plasma-based acceleration. Motivation and layout of the thesis

In the context of plasma-based acceleration, the beam-plasma system is assumed to be cylindrically symmetric. When an asymmetry is present in the system, e.g., a misalignment between a beam and a plasma column, an asymmetric charge distribution of the beam, a displacement of the beam centroid position, etc., the interaction of the bunch and the plasma electrons becomes non-axisymmetric, both for the bunch and the "walls" of plasma electrons displaced by the bunch, thus also for the wakefields the bunch drives. This results in the centroid positions of the bunch and of the wakefields to oscillate. As the displaced slices of the bunch and the plasma electrons act on each other, a feedback loop is formed, that leads to growth of the centroid position oscillation of both the bunch and the wakefields (for a detailed description of the mechanism see Section 2.3.2). This process is referred to as hosing and its development in a pre-formed plasma channel was first described in the plasma-based acceleration context by Whittum et al. [46]. More generally, hosing is a process that occurs in several other systems and contexts, disguising itself under a different name. For example, in the conventional acceleration, a similar process is called beam breakup (BBU) instability. It develops when the bunch is misaligned with respect to the walls of the accelerating structure. The resulting bunch centroid position offset causes charge accumulation in the metallic structures, leading to the wakefields, that appear in the cavity, to enhance the initial perturbation. An analogous to hosing kink instability occurs in stellar systems [47] and relativistic jets [48, 49], that are the subject of extensive astrophysics research.

Hosing is a detrimental phenomenon in plasma-based acceleration. It can affect both drive and witness bunches, resulting in the decrease of their quality. Moreover, hosing that affects the drive bunch might result in its eventual breakup, limiting the acceleration length. Also, as shown in [50], the wakefields driven by such bunch are no longer axi-symmetric. An on-axis deflecting force component appears, that might result in scattering or loss of the witness bunch. It is therefore important to study and understand hosing, thus, to be able to suppress it, if needed. Hosing was extensively described in theory [46, 50–55] and numerical simulations [56], for both particle bunches and laser pulses. Multiple mitigation strategies were proposed [57–60]. However, at the moment there is little experimental evidence of hosing. The development of hosing was shown experimentally for a laser pulse [61], as well as for a short electron bunch [62]. However, the properties of this process were not extensively studied. At AWAKE, hosing, i.e., the centroid position oscillation of the bunch growing along the bunch and the plasma, was unambiguously observed and described in the dissertation work of Hüther [63]. This work shows that hosing was observed as an instability, that is, the process was not reproducible from event to event and did not develop in a consistent way. The plasma electron density was low, $n_{pe} \approx 0.5 \times 10^{14}$ cm^{-3}, and at higher densities hosing was not observed. Moreover, seeding SM with the RIF was shown to strongly suppress the growth of hosing.

In this thesis, we study hosing induced by misalignment of the seed electron bunch trajectory with respect to that of the proton bunch. We observe, for the first time, hosing that is reproducible from event to event. This reproducibility and somewhat controlled conditions of the development of hosing allow for studying this process with better accuracy and in greater detail, deducing its multiple characteristics in a consistent way, in contrast with the previous works. Hosing develops simultaneously with SM, in the perpendicular planes. We observe hosing at $n_{pe} \approx (1-2) \times 10^{14}$ cm^{-3}, and it might be induced at even higher plasma densities, reaching that of operation ($n_{pe} \approx 7 \times 10^{14}$ cm^{-3}). We note, that we use relatively low plasma densities to be able to observe hosing on the time-resolved images of the bunch obtained by a streak camera, given its time resolution limit. The occurrence of hosing thus becomes more critical for the future applications of AWAKE, if the electron bunch is chosen as a seed for SM. Therefore, the development of hosing and its dependency on the experimental parameters have to be understood.

The structure of the thesis is as follows. In the next chapter, we present an overview of the main theoretical concepts of plasma-based acceleration and of several beam-plasma instabilities, focusing on those particularly relevant to this work. In Chapter 3, we introduce the working principle of the AWAKE experiment and give a short overview of studies performed at AWAKE. We outline the experimental setup, focusing on the components used in the measurements, whose results are presented here. My contributions to the experimental setup, characterization of the streak cameras and corresponding optical lines in terms of the time and spatial resolution determination, are described. We also briefly introduce the planned upgrade of the AWAKE experimental setup and outline the proposals for future applications. In Chapter 4 we first characterize hosing and SM occurring simultaneously. We describe a method to reconstruct the 3D charge density distribution of the proton bunch, that is particularly useful for the detection of hosing developing along with SM. We show the dependency of hosing on the direction of electron-proton beams misalignment. We determine the frequencies of hosing and of SM at two plasma electron densities, $n_{pe} = 0.96 \times 10^{14}$ cm^{-3} and $n_{pe} = 2.03 \times 10^{14}$ cm^{-3}. We study how the development of hosing depends on the variation of certain experimental parameters, such as the electron-proton beams misalignment extent and the proton bunch charge. We compare the experimental results with a theoretical model of a long-beam, early-time regime hosing. Chapter 5 presents the general conclusions of this work, as well as the unanswered questions, and suggests possible future studies. In Appendix A, we show an observation of hosing in the instability regime without SM at the very low plasma electron densities $n_{pe} < 0.5 \times 10^{14}$ cm^{-3} in the direct current (DC) discharge plasma source, that was installed and tested at AWAKE.

Chapter 2

Theory and concepts

In this chapter, we outline the main theoretical concepts of plasma-based acceleration. We define plasma, focusing on its properties that make it possible for a plasma wave, here wakefields, to develop. We provide the main expressions of the linear wakefield theory, which is assumed in the rest of this work. We then describe the theory behind the main beam-plasma instabilities of interest, as well as the methods to control some of the instabilities.

2.1 Plasma and its properties

By definition, a plasma is a quasi-neutral gas of charged and neutral particles which exhibits collective behavior [64]. The first condition, the collective behavior means that the charges in plasma interact, through Coulomb force, not only with their closest neighbors, but also with many other remote charges. Another property of plasma, related to its quasineutrality, is shielding out the electrical potentials that are applied to it. This is referred to as Debye shielding. The measure of this shielding or of the thickness of the sheath, the Debye length, is defined as [64]:

$$\lambda_D = \sqrt{\frac{\epsilon_0 K T_{pe}}{n_{pe} e^2}}, \tag{2.1}$$

where K is the Boltzmann constant and T_{pe} is the plasma electron temperature. The electron temperature is used because the plasma electrons, being more mobile than ions, generally do the shielding by moving, to compensate for the lack of negative charge or to eliminate its surplus. Now, we can define a second condition of a plasma.

The system is considered quasineutral if its dimensions L are much larger than λ_D, that is, whenever a local charge non-neutrality arises, it is shielded out in a distance smaller than L, leaving the rest of the system essentially free of substantial electric fields. This overall leads to another criterion for a gas to be a plasma – to be dense enough, such that $\lambda_D \ll L$.

The Debye shielding outlined above is statistically valid only when there is a sufficient number of plasma particles in the sheath region. That is, the number of particles in the so-called "Debye sphere" has to be much larger than one:

$$N_D = \frac{4}{3} n_{pe} \pi \lambda_D^3 \gg 1. \tag{2.2}$$

That is also a condition for the collective behavior.

The third condition for a gas to be called plasma is for the electrostatic interactions to dominate over particle collisions. That is, the collision period has to be larger than the plasma period, over which plasma oscillations typically occur: $\tau_c \gg \tau_{pe}$, where $\tau_{pe} = 2\pi/\omega_{pe}$.

Overall, these plasma properties enable propagation of the plasma waves and the creation of the wakefields. Lastly, we note that the Debye length is used to characterize plasmas, where thermal equilibrium has been reached, which is not the case in the time scale of interest at AWAKE ($\sim$ ns). Thus, in this thesis we use another characteristic scale, the cold plasma electron skin depth c/ω_{pe}, as it does not depend on the plasma electron temperature and is the measure of the plasma electron oscillation amplitude.

2.2 Linear plasma wakefield theory

Wakefields driven by a charged particle bunch or a laser pulse are described by linear theory, if the created plasma electron density perturbation is small compared to the overall plasma density $\delta n_{pe} \ll n_{pe}$. In the derivations below, we consider a particle bunch. The 2D cylindrical charge distribution of the bunch is given by:

$$n_b(t, r) = n_{b0} n_{b||}(t) n_{b\perp}(r), \tag{2.3}$$

where $n_{b0} = n_b(t = 0, r = 0)$ is the charge density of the bunch, $n_{b||}(t)$ and $n_{b\perp}(r)$ – normalized longitudinal and transverse charge distributions.

The longitudinal and transverse wakefields $W_z(t, r)$ and $W_r(t, r)$ as a function of the radial distance from the bunch propagation axis and the time along the bunch are defined as [65, 66]:

$$W_z(t, r) = \frac{n_{b0} e c}{\epsilon_0} \int_{-\infty}^{t} n_{b||}(t') \cos(\omega_{pe}(t - t'))dt' \cdot R(r) \tag{2.4}$$

and

$$W_r(t, r) = -\frac{n_{b0} e c^2}{\epsilon_0 k_{pe}} \int_{-\infty}^{t} n_{b||}(t') \sin(\omega_{pe}(t - t'))dt' \cdot \frac{dR(r)}{dr}. \tag{2.5}$$

In the equations above, we convert the bunch co-moving variable $\zeta = ct - z$ (z – propagation distance in plasma) from the original expressions into the time along the bunch t, as the time is used in the rest of this thesis. The plasma wavenumber is $k_{pe} = \omega_{pe}/c$, and k_{pe}^{-1} is the cold plasma skin depth. The radial dependency of the longitudinal wakefields $R(r)$ and its derivative $\frac{dR(r)}{dr}$, the radial dependency of the transverse wakefields, are given by:

$$R(r) = k_{pe}^2 K_0(k_{pe} r) \int_0^r r' n_{b\perp}(r') I_0(k_{pe} r')dr' + k_{pe}^2 I_0(k_{pe} r) \int_r^{\infty} r' n_{b\perp}(r') K_0(k_{pe} r')dr' \tag{2.6}$$

and

$$\begin{aligned} \frac{dR(r)}{dr} = 2k_{pe}^2 K_0(k_{pe} r) r n_{b\perp}(r) I_0(k_{pe} r) - k_{pe}^3 K_1(k_{pe} r) \int_0^r r' n_{b\perp}(r') I_0(k_{pe} r')dr' - \\ - k_{pe}^3 I_0(k_{pe} r) \int_r^{\infty} r' n_{b\perp}(r') K_0(k_{pe} r')dr'. \end{aligned}$$

I_0 , I_1 and K_0 , K_1 are the zeroth and first order modified Bessel functions of the first and second kind, respectively. The longitudinal wakefields are maximum on-axis (R(0)), while the transverse wakefields are zero on-axis and have their peak around $r = \sigma_r$ (σ_r – the bunch transverse size).

As already mentioned in Section 1.2, according to linear wakefield theory, in order to effectively drive large-amplitude wakefields, the longitudinal and transverse sizes of the bunch have to satisfy the following conditions [13, 67]:

$$k_{pe}\sigma_t = \sqrt{2}, \tag{2.7}$$

and

$$k_{pe}\sigma_r \leq 1, \text{ or } \sigma_r < k_{pe}^{-1} = c/\omega_{pe}. \tag{2.8}$$

In the context of AWAKE and of the measurements presented here, we consider linear wakefield theory applicable at the plasma entrance, as the proton bunch density is in range $n_{b0} \approx (4.3 - 7.0) \cdot 10^{12}$ cm^{-3}, that is much lower than the plasma electron density $n_{pe} > 0.9 \cdot 10^{14}$ cm^{-3}.

2.3 Beam-plasma instabilities

A beam-plasma system is subject to various instabilities. These instabilities can grow from noise, irregularities or asymmetries in the beam-plasma system. Alternatively, some of them can be externally seeded, that is, their properties can be controlled. We discuss the instabilities particularly relevant for AWAKE and for the study presented here.

2.3.1 Self-modulation instability. Seeding of self-modulation.

Self-modulation (SM) is a transverse axi-symmetric instability that affects a long ($> \lambda_{pe}$) particle bunch propagating in plasma and that transforms it into a train of equally spaced microbunches, separated by the plasma period τ_{pe} (Fig. 2.3.1). The head of the bunch drives initial wakefields (Fig. 2.3.1, top schematic, black arrows), that co-propagate with the bunch and that periodically (at τ_{pe}) focus and defocus the bunch particles, i.e., regions with higher and lower charge density are created. The amplitude of the wakefields is proportional to the charge density, therefore the bunch becomes more focused where the density is already higher, hence further increasing the wakefield amplitude. Regions where the particles are defocused, i.e., the bunch density is lower, drive lower-amplitude wakefields. As the bunch density modulation is at the period of τ_{pe}, the process is resonant and leads to periodic modulation of the bunch density.

The evolution of the bunch envelope in case of SM in the long-beam, early-time

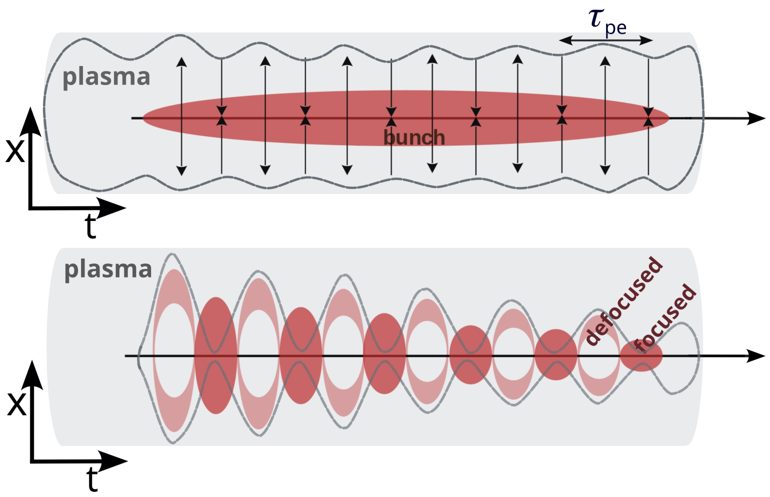

Figure 2.3.1: Schematic of SM development. Top: the bunch (in this example – proton bunch), propagating in plasma, starts driving initial wakefields (black arrows) at its head, causing perturbation in plasma electron density (dashed grey lines), that periodically modulates the bunch density. The regions of the bunch with higher density drive larger-amplitude wakefields, the ones with lower density – lower-amplitude wakefields. The process is therefore resonant and leads to periodic modulation of the bunch density (bottom), transforming it into a train of short microbunches spaced by τ_{pe} (or λ_{pe}).

regime was determined by Schroeder et al. in [68]. The linear regime of interaction ($\delta n_{pe}/n_{pe} \ll 1$) and constant longitudinal and transverse distributions of the bunch were assumed. With initial bunch radius perturbation δr and the time t_0 when the growth of SM starts, such that $r(z, t = t_0) = \delta r \Theta(z)$, where $\Theta(z)$ denotes a Heaviside function, and $r(z = 0, t) = \delta r$, the asymptotic solution of the bunch radius perturbation equation is as follows [68]:

$$r_1 = \delta r \left[\frac{3^{1/4}}{(8\pi^{1/2})} \right] \frac{e^{N_{SM}}}{N_{SM}^{1/2}} \cos(\pi/12 - \omega_{pe}(t - t_0) - N_{SM}/\sqrt{3}), \tag{2.9}$$

where

$$N_{SM} = \frac{3^{3/2}}{4} \left(\nu \frac{m_e}{m_b} \frac{n_{b0}}{n_{pe}} \frac{1}{2\gamma} \left(\frac{\omega_{pe}}{c} \right)^2 z^2 \omega_{pe}(t - t_0) \right)^{1/3}. \tag{2.10}$$

There, N_{SM} stands for the number of exponentiations of SM. In its expression, $\nu = 4I_2(k_{pe}r_0)K_2(k_{pe}r_0)$, m_b is the bunch particle mass and γ is the relativistic factor of the bunch. The N_{SM} describes the growth of the SM along the bunch, through its $\omega_{pe}(t - t_0)$ term, at a given position z along the plasma.

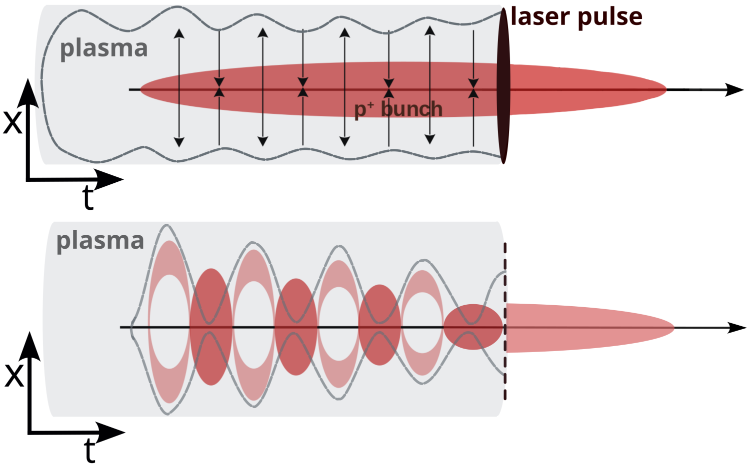

Figure 2.3.2: Schematic of SM seeded with the RIF. Initially the proton bunch propagates in Rb vapor. Short high-intensity laser pulse, placed within the proton bunch, co-propagates with it, ionizing the vapor and thus creating a sharp onset of the beam-plasma interaction within the proton bunch (top). As a result, SM develops in the part of the bunch propagating in plasma (bottom), while the front of the bunch remains unmodulated. SM develops in a reproducible way, since the location and the amplitude of the seed (RIF) are approximately (within the time jitter of the laser pulse and the proton bunch) the same from event to event.

When SM develops as an instability, it grows from irregularities (noise) at the head of the bunch, that drive low-amplitude wakefields. These wakefields differ from event to event, thus, the resulting SM is not reproducible in time or amplitude. In order to control this process, seeding, that is, generating wakefields with amplitude larger than that of the wakefields arising from noise, is introduced. With seeding, the timing and the amplitude of the seed, hence, those of the resulting SM, can be controlled. At AWAKE, two methods of seeding SM, with the relativistic ionization front (RIF) [44] and with the short electron bunch [45] are demonstrated and used.

Figure 2.3.2 demonstrates the principle of seeding SM with the RIF. The proton bunch initially propagates in the Rb vapor, that is used for plasma (see Section 3.1 and Section 3.4). A short, high-intensity ionizing laser pulse (see Section 3.3) is placed within the proton bunch and co-propagates with it, ionizing the Rb vapor and creating a sharp onset of beam-plasma interaction. It serves as the seed for SM, that develops in the part of the bunch propagating in plasma. The part of the bunch propagating in vapor remains unmodulated. Seeded with the RIF, SM was found to be reproducible from event to event, when the RIF is placed $\leq 2\sigma_t$ from the peak of the bunch, with timing variation of $\Delta t/\tau_{pe} \sim 6\%$ [44]. The advantage of this seeding method is, given that the laser pulse and the proton bunch are spatially aligned, that the development of hosing, that grows at the rate similar to that of SM [50] (see next section), is suppressed. The possible disadvantage is that the unmodulated head of the bunch, propagating further along the plasma, e.g., in the second plasma stage, might start modulating and therefore interfering with the already modulated part. Recent study showed, however, that this possible issue may not occur [69].

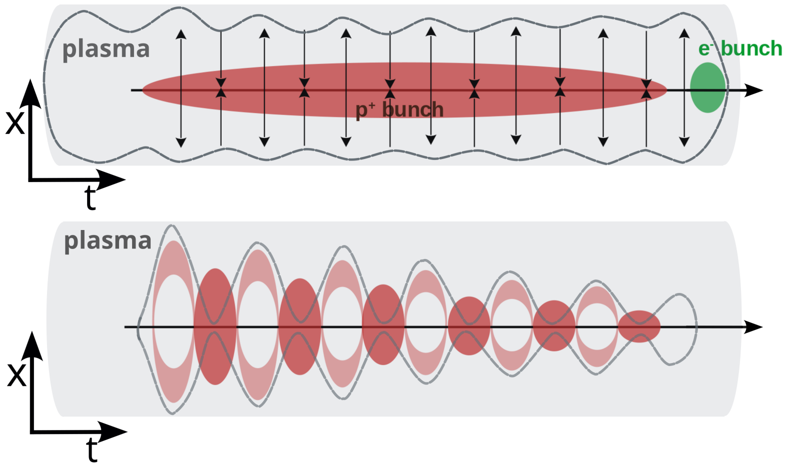

Figure 2.3.3: Schematic of SM seeded with a short electron bunch that propagates ahead of the proton bunch. The electron bunch drives initial wakefields that start the development of the SM of the proton bunch in a reproducible way. With this seeding method, the proton bunch density is fully-modulated.

Another approach to seed SM is to use a short electron bunch that propagates ahead of the proton bunch, in a pre-formed plasma. The electron bunch drives initial wakefields with amplitude exceeding that of the noise wakefields, therefore SM of the proton bunch is reproducible from event to event, with the timing variation of $\Delta t/\tau_{pe} \sim 7\%$ [45], similar to that of seeding with the RIF. When SM is seeded with the electron bunch, its timing can be varied by changing the delay between the proton and the electron bunches, and its amplitude can be varied by varying the electron or the proton bunch charge, that is, its parameters can be controlled and varied independently. Another possible advantage is that the proton bunch is fully-modulated. However, this seeding method strongly relies on spatial and angular alignment of the electron and proton bunch trajectories. When the two trajectories are misaligned, the initial wakefields are not axi-symmetric for the proton bunch, therefore, in addition to SM, hosing develops (see next section). Apart from alignment, possible asymmetries in the shape or the charge distribution of the electron bunch might lead to the development of hosing.

2.3.2 Hosing instability. Hosing induced by an electron bunch.

As mentioned in Section 1.3, when an asymmetry is present in the beam-plasma system, the interaction of the bunch and plasma becomes asymmetric with respect to the bunch propagation and plasma column axes. This leads to the development of hosing. Figure 2.3.4 shows an example of a bunch (an electron bunch is assumed) with an initial centroid position perturbation (top schematic, dashed red line, denoted x_c) entering a uniform plasma. The bunch expels the plasma electrons from its propagation axis. The slice of the bunch that is closer to the expelled "wall" of plasma electrons pushes them, e.g., upwards, while the electrons push this bunch slice downwards. The force that acts on every slice of the bunch, and that is created by every slice of the bunch, is not axi-symmetric. As in case of SM, the bunch and the plasma electrons act back on each other, therefore the centroid position of the bunch x_c couples to the centroid position of the wakefields (or of the global focusing force) x_w. The process continues resonantly, resulting in the oscillation of both centroid positions x_c and x_w. The two oscillations are in counterphase and grow along the bunch and the plasma.

Hosing can be described by a system of differential equations of oscillatory motion for x_c and x_w, respectively [70]:

$$\begin{cases} \Big(\dfrac{\partial}{\partial z^2} + \dfrac{m_e}{m_b}\dfrac{n_{b0}}{n_{pe}}\dfrac{1}{2\gamma}\dfrac{\delta n_{pe}}{n_{pe}}\Big)x_c = \dfrac{m_e}{m_b}\dfrac{n_{b0}}{n_{pe}}\dfrac{1}{2\gamma}\cdot x_\mathrm{w} \\ \Big(\dfrac{1}{c}\dfrac{\partial}{\partial t^2} + k_{pe}^2\Big)x_\mathrm{w} = k_{pe}^2 n_{||}\cdot x_c \end{cases} \tag{2.11}$$

In addition, there is a coupling between the bunch density $n_{||} = r^2(z=0,t)/r^2(t)$ and the harmonic oscillation of plasma electrons ($\delta n_{pe}/n_{pe}$), i.e., wakefields, described as:

$$\Big(\frac{1}{c}\frac{\partial}{\partial t^2} + k_{pe}^2\Big)\frac{\delta n_{pe}}{n_{pe}} = -k_{pe}^2 n_{||}. \tag{2.12}$$

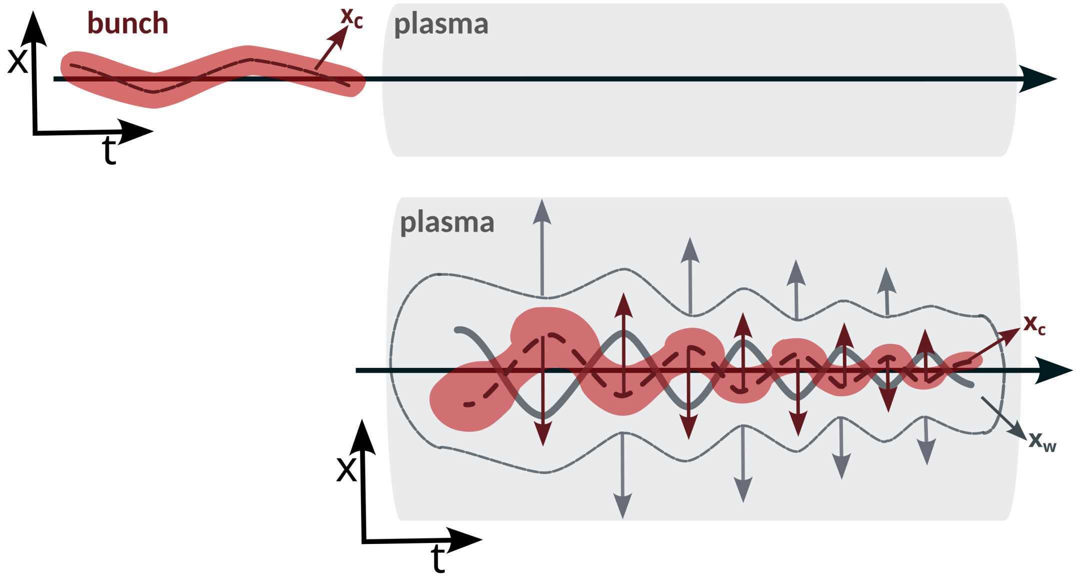

Figure 2.3.4: Schematic of the development of hosing in case of an electron bunch having an initial centroid position perturbation (top). The bunch (here – electron bunch) enters the uniform plasma and expels the plasma electrons (dashed grey lines) However, as some parts of the bunch are closer to the "wall" of expelled plasma electrons, the repelling force between these parts is larger, than in axi-symmetric case. Thus, these parts of the bunch are pushed, e.g., downwards, and the plasma electrons are expelled even more upwards. The process continues resonantly, resulting in the oscillation of the centroid position of the bunch and of the wakefields. These two oscillations are coupled and grow along the bunch and along the plasma (bottom).

Equations 2.11 and 2.12 show that hosing develops due to the coupling of x_c, oscillating at $\sqrt{\frac{m_e}{m_b}\frac{n_{b0}}{n_{pe}}\frac{1}{2\gamma}\frac{\delta n_{pe}}{n_{pe}}}$ in z, and x_{w}, oscillating at k_{pe} in t. The regime of the growth of hosing can be determined from which oscillation of Eqs 2.11 is nearly resonant: when x_{w} oscillates near k_{pe}, hosing grows in the long pulse (beam) regime [70], which is of interest in this work.

The asymptotic solution for the centroid position of the bunch with non-evolving radius in case of hosing is derived in [50]. As for the derivation in case for SM, linear regime of interaction and constant longitudinal and transverse distributions of the bunch are assumed. With initial centroid position perturbation δ_c and the time t_0 when the growth of hosing starts, such that $x_c(z, t = t_0) = \delta_c\Theta(z)$ and $x_c(z = 0, t) = \delta_c$, the asymptotic solution for x_c is as follows [50]:

$$x_c = \delta_c \left[\frac{3^{1/4}}{(8\pi^{1/2})} \right] \frac{e^{N_h}}{N_h^{1/2}} \cos\left(\frac{\pi}{12} - \omega_{pe}(t-t_0) - \frac{N_h}{\sqrt{3}} \right) \tag{2.13}$$

and

$$N_h = \frac{3^{3/2}}{4} \left(\mu \frac{m_e}{m_b} \frac{n_{b0}}{n_{pe}} \frac{1}{2\gamma} \left(\frac{\omega_{pe}}{c} \right)^2 z^2 \omega_{pe}(t-t_0) \right)^{1/3}. \tag{2.14}$$

In the expression of N_h, $\mu = 2I_1(k_{pe}r_0)K_1(k_{pe}r_0)$ represents the effect of the plasma return current. The evolution of the amplitude of x_c oscillation along the bunch is determined by N_h as a function of $(t-t_0)$ at a given z through the $\frac{e^{N_h}}{N_h^{1/2}}$ term. The growth of oscillation starts from the initial perturbation with amplitude δ_c at $z = 0$.

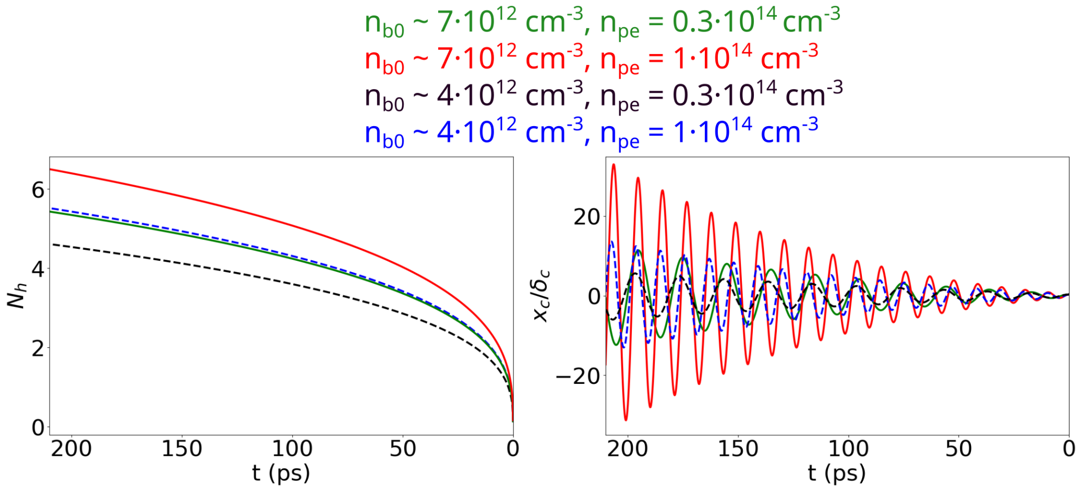

(a) (b)

Figure 2.3.5: (a) Number of exponentiations of hosing N_h along the bunch as a function of the proton bunch density n_{b0} and the plasma electron density n_{pe}. (b) Bunch centroid position oscillation x_c normalized to the initial displacement δ_c as a function of n_{b0} and n_{pe}. Values of n_{b0} and n_{pe} with colors corresponding to those of the curves are given in the legend.

Equations 2.13 and 2.14 are plotted in 2.3.5 for the proton bunch used at AWAKE (for the bunch parameters see Section 3.2 and Section 4.5.2), with two different bunch density values n_{b0} and at two different plasma electron densities n_{pe}, used in the experiments presented here. The number of exponentiations of hosing along the bunch (Fig. 2.3.5(a)) increases with n_{b0} (e.g., dashed blue and solid red lines, n_{pe} is constant), and with n_{pe} (e.g., solid green and red lines, n_{b0} is constant), as also seen from the increase of the x_c oscillation amplitude in Fig. 2.3.5(b). We note that, as

Eqs 2.13 and 2.14 describe asymptotic solutions, the approximation is less accurate when $t \to 0$ or $z \to 0$.

Equations 2.9 and 2.10, that describe SM, and Eqs 2.13 and 2.14, that describe hosing, are quite similar. The two processes have similar growth, i.e., $N_{SM}/N_h = (\nu/\mu)^{1/3}$. When $k_{pe}r_0 = 1$, this yields $N_{SM}/N_h \approx 1.5$. This ratio decreases with n_{pe}, that is, hosing is more likely to develop or dominate over SM at lower n_{pe}.

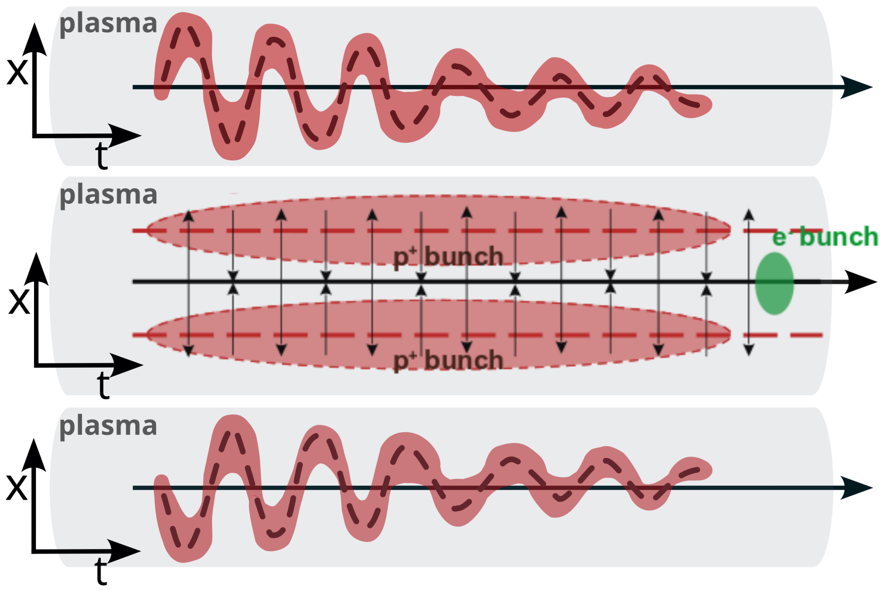

Figure 2.3.6: Schematic of hosing induced by the misalignment between the electron bunch, hence the initial wakefields it drives, with respect to the propagation axis of the trailing proton bunch. The effect of the wakefields is non-axisymmetric for the proton bunch, that results in its centroid position oscillation coupled to the wakefields, hence, to SM. Depending on the the direction of misalignment (e.g., +x → −x), the wakefields force acts on the bunch centroid position in the opposite directions. The x_c oscillation, as a result, is reflected with respect to the bunch propagation axis.

Generally, hosing develops as an instability, that is, this process is neither controlled nor reproducible from event to event. However, it is possible to induce hosing with misalignment of the initial wakefields axis with respect to that of the trailing bunch. At AWAKE, we misalign the trajectory of the electron bunch, that is also used to seed SM (see previous section), with respect to that of the trailing proton bunch (or vice versa). The results obtained in these measurements constitute the main topic of this thesis. When the trajectories of the two bunches are misaligned (Fig.

2.3.6), the initial wakefields are not axi-symmetric at the location of the proton bunch, therefore, not only they result in modulation of the bunch density, but also in periodic oscillation of the bunch centroid position. The centroid position of the bunch in this case is coupled to that of the wakefields, that is, to SM. The two processes thus develop simultaneously, in perpendicular planes, with hosing taking place in the plane of misalignment. Depending on the direction of the electron-proton beams misalignment (e.g., +x→ –x), the wakefields force acts on the proton bunch centroid position in the opposite directions. The resulting oscillation is thus reflected with respect to the bunch propagation axis (Fig. 2.3.6).

We finally note that the development of hosing coupled to SM, which is the case of the results presented here, was also studied in [50]. The numerical solution of the system of equations for centroid position displacement and for radius perturbation of the bunch indicates an asymmetry of the centroid position oscillation with respect to the bunch propagation axis, the presence of higher harmonics and the increase in the amplitude of oscillations, when compared to the case of pure hosing. We nevertheless use the model of pure hosing (Eqs 2.13 and 2.14) for further analysis and comparison with the experimental results, as all the higher-order effects resulting from the coupling could not be clearly and consistently observed in the experiment, except in case of the highest proton bunch charge.

2.3.3 Current filamentation instability

Another instability, that the beam-plasma system is subject to, is current filamentation instability (CFI). As a result, the beam breaks up into narrow and high current density filaments, thus generating or enhancing magnetic fields [71, 72]. Relativistic particles that interact with these magnetic fields emit synchrotron radiation, their trajectories may also be strongly altered, affecting the energy and momentum transport. The condition for CFI to develop is determined by a ratio of the transverse bunch size to the cold plasma skin depth. When the transverse bunch size is smaller than the skin depth $\sigma_r < c/\omega_{pe}$ or $k_{pe}\sigma_r < 1$, the plasma return current flows outside of the bunch and CFI does not develop. However, when $\sigma_r \geq c/\omega_{pe}$, the plasma return current flows through the bunch and CFI might develop. In plasma-based acceleration, given a bunch focused to a specific size, this instability imposes a limit on the maximum plasma density, therefore, on the maximum accelerating gradient.

Similarly to hosing, CFI is an instability common for several systems. It is a subject of research in inertial confinement fusion [73, 74] and astrophysics [75–77]. In plasma-based acceleration, Allen et al. showed the experimental observation of CFI [72]. At AWAKE, filamentation instability was observed by increasing the proton bunch size and varying the plasma electron density [78].

Chapter 3

AWAKE experimental setup

In this chapter, we present an overview of the AWAKE experimental setup. We describe the main components of the experiment, focusing on those of particular importance for this thesis. We conclude with an outlook on the planned upgrade of AWAKE.

3.1 General overview

The Advanced WAkefield Experiment (AWAKE) is an R&D project at CERN whose purpose is to study proton-driven plasma wakefield acceleration [79]. A schematic of the experimental setup is shown in Fig. 3.1.1. A proton bunch (green line) with an energy of 400 GeV per particle is delivered to the experimental area by the CERN Super Proton Synchrotron.

A laser provides an intense (up to 450 TW/cm^2) pulse (red line), whose trajectory is aligned onto that of the proton bunch. The same laser is used to generate an electron bunch in a photoinjector. This bunch (blue line) is accelerated in the booster cavity and transported to the proton beam line.

When seeding SM with an electron bunch, the laser pulse propagates ahead of the electron and proton bunches, and enters a 10 m-long Rubidium (Rb) vapor source. It provides full, single ionization of the Rb vapor, creating a plasma column of ~ 1 mm radius. The electron bunch propagates in plasma, 20 ps behind the laser pulse, and 600 ps ahead of the proton bunch (on its axis). It drives initial wakefields that transform the trailing proton bunch into a train of microbunches. The microbunches

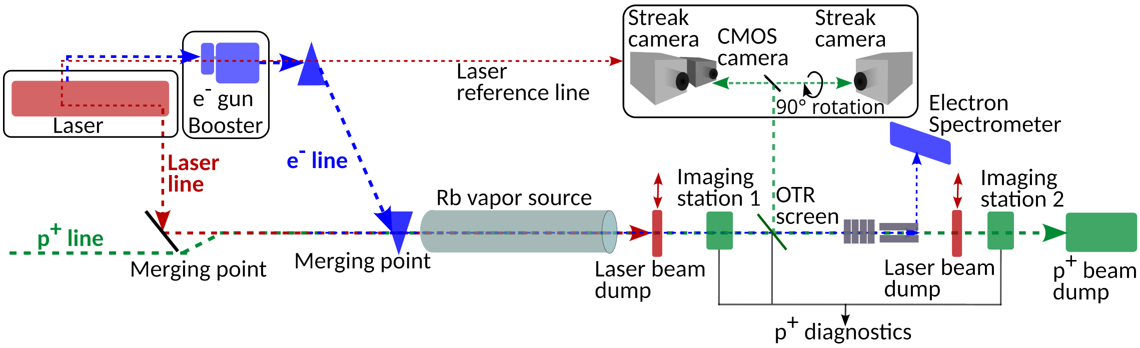

Figure 3.1.1: Simplified schematic of the AWAKE experimental setup (not to scale). Certain diagnostic components of the beam lines, such as beam TV systems (BTVs), beam position monitors (BPMs), and the Rb density measurement diagnostic are not shown.

then resonantly drive large amplitude wakefields that can be used for acceleration (see Section 2.3.1). Alternatively, SM can be seeded with the RIF of the laser pulse placed within the proton bunch (See Section 2.3.1). Finallly, the electron bunch (provided by the same system as the one seeding SM) can be injected into the wakefields driven by the proton bunch, typically near its longitudinal peak, where it can be accelerated.

After the plasma exit and the laser beam dump (Fig. 3.1.1), several diagnostics are in place to measure the properties of the proton bunch, such as its spatio-temporal and transverse structures. The optical transition radiation (OTR) is emitted when protons enter an aluminum-coated silicon wafer (OTR screen). The OTR has the same spatio-temporal structure as that of the incoming bunch (see Section 3.5.1). It is transported, split and imaged onto the entrance slit of two streak cameras that provide time-resolved images of the bunch charge density distribution. A spatial rotation of 90° is applied to one of the OTR signals, thus the images are in two perpendicular planes (x, t) and (y, t) (Fig. 3.1.1). To overcome the jitter of the triggering system, thus, to determine the precise timing of the features on time-resolved images, we use the reference laser pulse (see Section 3.3). It is imaged onto the slit of the streak cameras and serves as a timing reference that allows temporal alignment of images at the sub-ps level [80]. Time-integrated images of the proton bunch charge distribution in its core and halo are obtained at imaging stations 1 and 2. An additional CMOS camera yields a full bunch charge distribution from the same OTR screen that is used with the streak cameras. Both time-resolved and time-integrated imaging systems are the main diagnostics used for this thesis.

The electron spectrometer, positioned after the OTR screen, measures the energy of the electron bunch during acceleration experiments, and thus also the energy it may gain in plasma.

During the experiments performed at AWAKE, SM of a long proton bunch was observed for the first time. The SM frequency, f_{SM}, was confirmed to be close to the plasma electron frequency f_{pe} [81], as expected from theory. When seeded, either with the RIF [44] or with the electron bunch [45], SM was demonstrated to be reproducible from event to event. The effect of linear plasma density gradients on SM was studied [82]. Acceleration of the electron bunch from ~ 18 MeV to ~ 2 GeV in the wakefields driven by the proton bunch was demonstrated [43]. Studies of other instabilities affecting the proton bunch, such as hosing (Section 2.3.2) and CFI (Section 2.3.3), were performed.

3.2 Proton beam line

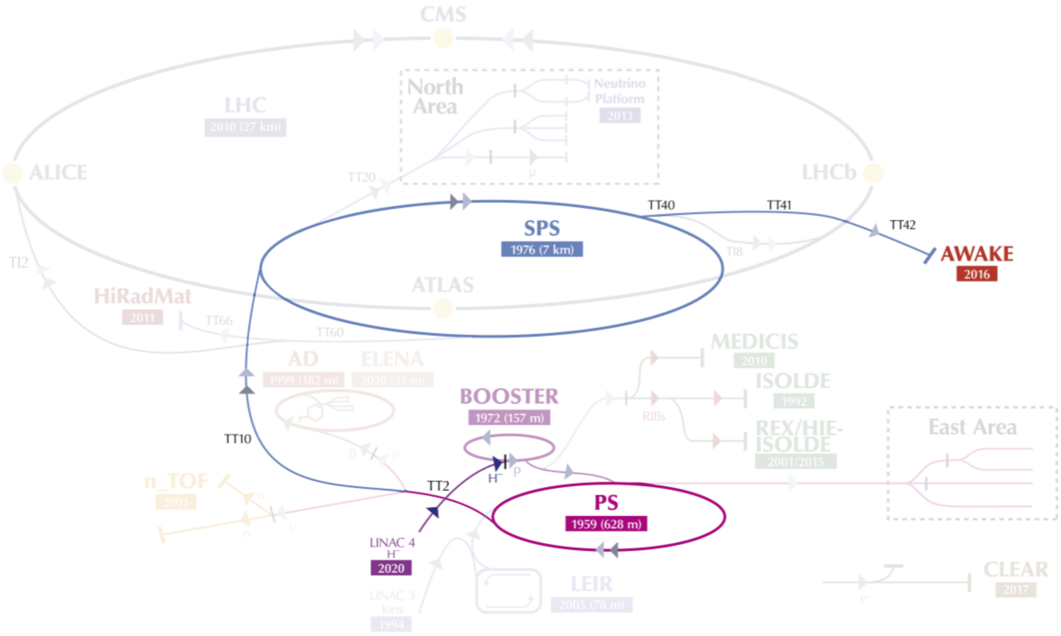

Figure 3.2.1: Schematic of the accelerator complex at CERN taken from [83]. The proton bunches are accelerated to the desired energy in several stages and are then delivered to the AWAKE experiment (shown in dark orange on the right-hand side) by the Super Proton Synchrotron (SPS).

The protons are initially produced by the Linear Accelerator 4 (Linac4) that accelerates negative hydrogen ions (atoms with an additional electron) to 160 MeV (Fig. 3.2.1). The ions are then stripped of their two electrons, leaving only protons, when injected from Linac4 to the Proton Synchrotron Booster (PSB). The PSB accelerates the protons to 2 GeV for injection into the the Proton Synchrotron (PS). The PS further increases the proton energy to 26 GeV. Finally, the protons are injected into the Super Proton Synchrotron (SPS) and are accelerated to 450 GeV, to be injected into the Large Hadron Collider (LHC). Additionally, the SPS provides proton bunches to several experiments, including AWAKE. For AWAKE, a single bunch with population N_b up to 3×10^{11} protons and an energy of 400 GeV per proton is extracted from the SPS and is sent via a transfer line to the experimental area.

In the experimental area, several diagnostics are in place to measure the proton bunch parameters. Beam position monitors (BPMs) determine the position of the bunch in the beam pipe in a non-invasive manner. Beam television systems (BTVs) have a scintillator screen that is inserted into the beam path. The light from the screens is imaged onto a camera. These systems are used for the measurement of the position, shape and size of the bunch. The emittance of the bunch is measured in the SPS with a wire scan method.

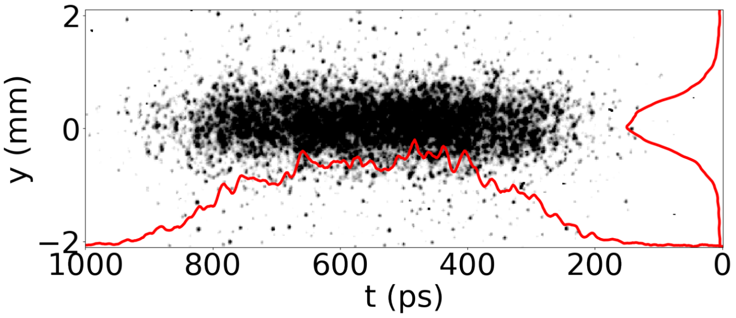

Figure 3.2.2: Time-resolved image of the proton bunch propagating in vacuum. $N_b \approx 1 \cdot 10^{11}$. Longitudinal (time) and transverse profiles are shown as red lines. Time window length is 1 ns.

Both longitudinal and transverse profiles of the proton bunch used at AWAKE are approximately Gaussian (Fig. 3.2.2, red lines). The transverse shape of the bunch is round. For these experiments, the transverse root mean square (rms) waist size, measured on the BTV near the plasma entrance, is $\sigma_{r0} \approx 0.15$ mm when $N_b \approx 1 \cdot 10^{11}$, and $\sigma_{r0} \approx 0.2$ mm when $N_b \approx 3 \cdot 10^{11}$. The longitudinal rms size, determined with the streak camera, is $\sigma_t \approx 220$ ps (Fig. 3.2.2), or, converting to spatial units, $\sigma_z \approx 6.3$ cm. The position jitter of the proton bunch near the plasma entrance, summed in quadrature for x- and y-directions, is around 53 μm. This value is lower than the spatial resolution of the streak camera (see Section 3.5.3) and therefore does not affect further analysis based on averaging of time-resolved images (see Section 4.1).

3.3 Ionizing laser system and electron beam line

The laser of AWAKE is a Titanium Sapphire (Ti:Sa) system produced by Amplitude Systems that relies on the chirped pulse amplification (CPA) technique to generate ultra-short, high-intensity pulses. A detailed description of the laser is given in Ref. [84].

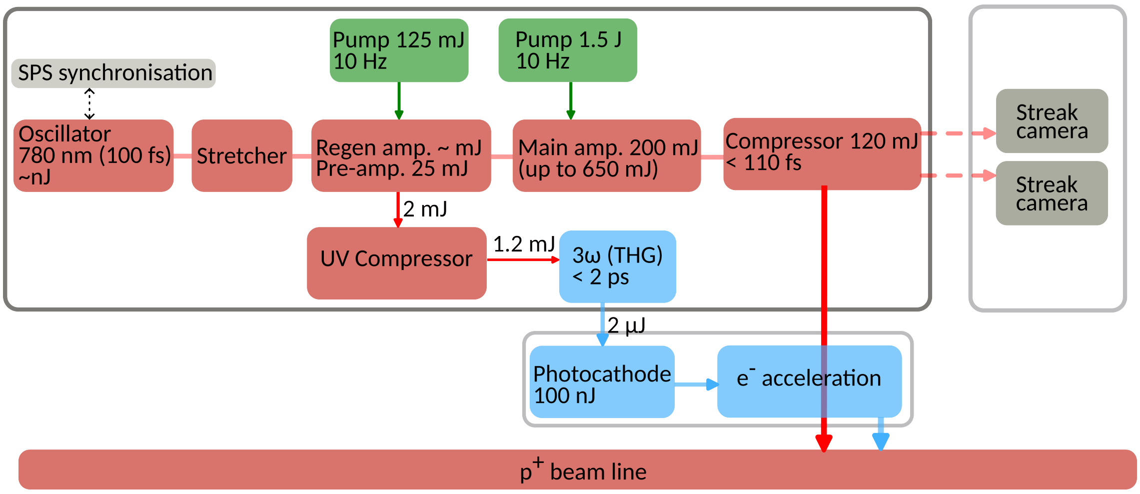

Figure 3.3.1: Schematic of the AWAKE laser system.

A schematic overview of different components and beam lines of the laser system is shown in Fig. 3.3.1. The laser oscillator is an Erbium-doped fiber system with a wavelength $\lambda = 1560$ nm and repetition rate of 88.2 MHz, that provides ~ 1 nJ, 100 fs pulses. The operational wavelength $\lambda = 780$ nm is obtained with second harmonic generation (SHG). The pulses are then sent to a stretcher that introduces a frequency chirp and therefore elongates them from 100 fs to ~ 200 ps. In the regenerative amplifier, pumped by a frequency-doubled 125 mJ Nd:YAG laser, single pulses are picked by a pair of Pockels cells with a repetition rate of 10 Hz, and the pulse energy is increased to ~ 1 mJ. The pulses then enter a multi-pass pre-amplifier, pumped by the same laser as the regenerative amplification stage, where their energy is increased to ~ 25 mJ. In the final multi-pass amplification stage, pumped by a frequency-doubled 1.5 J Nd:YAG laser, the pulses reach an energy of up to 650 mJ. With the current design of the laser beam line used for ionization, the energy of these pulses is attenuated to ~ 200 mJ. They are shortened back to < 110 fs in the vacuum grating compressor and have a final energy of ~ 110 mJ. These pulses are transported to the vapor source where they ionize the Rb vapor to create plasma. Two movable thin-foil laser beam dumps are installed after the vapor source (see Fig. 3.1.1) to dump the laser pulse when diagnostics are present in the beam line.

The reference laser pulse (see Section 3.1) is a bleed-through of the ionizing laser pulse that is collected from a mirror after the compressor. This reference pulse is transported to be imaged onto the slit of the streak cameras, as described in Ref. [80]. This beam line includes a delay stage, so that the relative timing of the reference pulse with respect to the main ionizing pulse can be adjusted.

The laser pulse for the electron bunch generation is collected after the pre-amplification stage (blue blocks, Fig. 3.3.1). It has around 10% of the energy (~ 2 mJ) at that stage. The pulse is sent to an in-air compressor and to a third harmonic generation (THG) stage. From there, the < 2 ps-long pulse with $\lambda = 260$ nm and energy of 2 μJ propagates to a Caesium telluride (Cs_2Te) photocathode. The pulse energy on the cathode is typically limited to ~ 100 nJ. The UV pulse hits the photocathode and extracts the electrons from its material. The electrons are first accelerated to an energy of 5.5 MeV in an RF-gun and then to 20 MeV in a booster. The resulting electron bunch typically has a rms duration of 2-6 ps, a charge of 100 pC to 1 nC (in the experiments presented here – 225 pC), a normalized rms emittance of 2 mm·mrad (rms) and a final energy of 18.9 MeV. This bunch is transported to the main beam line. Several diagnostics are present to measure the shape, position and charge, such as BTVs, BPMs and a Faraday cup. The position jitter of the bunch measured near the plasma entrance, summed in quadrature for x- and y-directions, is around 34 μm. The relative timing between the ionizing laser pulse and the electron bunch can be adjusted with an optical delay stage.

3.4 Vapor source

The vapor source (Fig. 3.1.1) is a major component of the AWAKE experiment, where plasma is created. It consists of a 10 m-long tube with an expansion volume at each end. Rb is used as a medium for the plasma because of its relatively low ionization potential of 4.18 eV, that allows for ionization with a relatively low intensity laser pulse. Rb is evaporated into the system in an adjustable temperature range 150° C – 230° C, that is, the possible plasma density range is $(0.5 - 10) \times 10^{14}$ cm^{-3}. A heat exchanger allows for a uniform (better than 0.2% uniformity [85]) vapor and thus plasma density. Additionally, linear plasma density gradients up to 20% between the two ends of the source can be set. The vapor density length product, from which the density value is extracted, is measured at each end of the vapor source with fiber-based, white-light interferometers [86] to better than 0.5% accuracy [87].

3.5 Streak cameras

3.5.1 OTR and streak camera working principle

A charged particle passing through a transition between two materials with different dielectric constants causes emission of transition radiation [88]. It is emitted in forward direction in a cone with opening angle $1/\gamma$ (forward radiation), with γ being the Lorenz factor of the particle, and simultaneously reflected by the surface of the transition material (backward radiation). Transition radiation has a broad spectrum, and its part in the visible light spectrum is referred to as OTR. To observe the evolution of the proton bunch in time after the propagation in plasma, we detect backward OTR emitted when the bunch enters the OTR screen. The OTR is prompt, and the number of emitted photons is proportional to the number of particles entering the screen [89]. It is then transported via an optical line and is imaged onto the entrance slit of two streak cameras.

The working principle of the streak cameras (Hamamatsu Photonics, model C10910-05) is shown in Fig. 3.5.1. The light passes through the slit and reaches a photocathode, where it is converted into a number of electrons proportional to the number of incoming photons. The electrons are accelerated in the mesh and propagate through a transverse electric field between two sweep electrodes. A temporally varying sweep

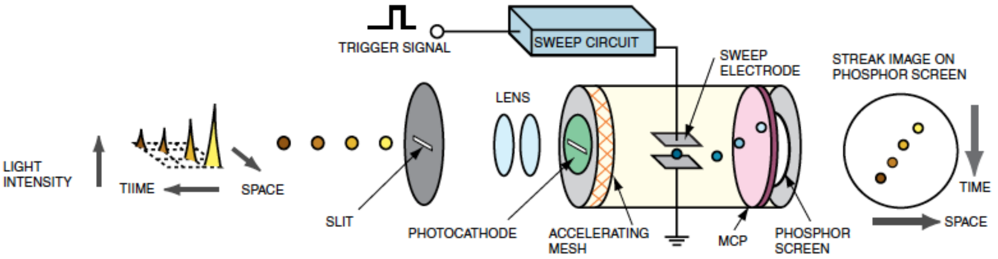

Figure 3.5.1: Working principle of a streak camera. Taken from [90].

voltage, synchronized to the timing of the incoming photons, deflects the electrons by an angle depending on their arrival time. The electrons separated in time thus get separated in space and enter a micro-channel plate (MCP), where they are multiplied before being sent onto a phosphor screen. There electrons are converted back to light. A CMOS camera (16 bit) gathers an image representing, in case of results presented here, the distribution of protons in space and time. We note that the slit width used in the measurements (20 μm) is smaller than the proton bunch size at the OTR screen ($\sigma_{r,OTR} > 480$ μm). Thus, transverse slice of the bunch is imaged and the light intensity in the images is proportional to the bunch charge density. The image has the time axis of 512 px and the spatial axis of 672 px. The possible time windows of the data acquisition are between 73 ps and 50 ns.

Time axis linearization

As mentioned above, in order to obtain the distribution of light over time, the sweep voltage is applied to convert time separation of clusters of electrons in the streak tube into space separation along one of the axes of the resulting image. Since this applied voltage is not linear, the time axis of the streak camera image is also nonlinear, that is, the time range per pixel is not constant along the image (Fig. 3.5.2, black line). This nonlinearity affects the frequency analysis of the streak camera data, since the discrete Fourier transform (DFT) algorithm relies on equidistant sampling.

We therefore linearize the images with an interpolation algorithm. The original pixel counts are re-distributed from a non-linear grid onto a linear one, while preserving the number of counts. Figure 3.5.2 shows the time range per pixel before (black line) and after (blue line) the linearization for three streak camera time windows that are used in this thesis. This procedure is applied to all the streak camera data presented

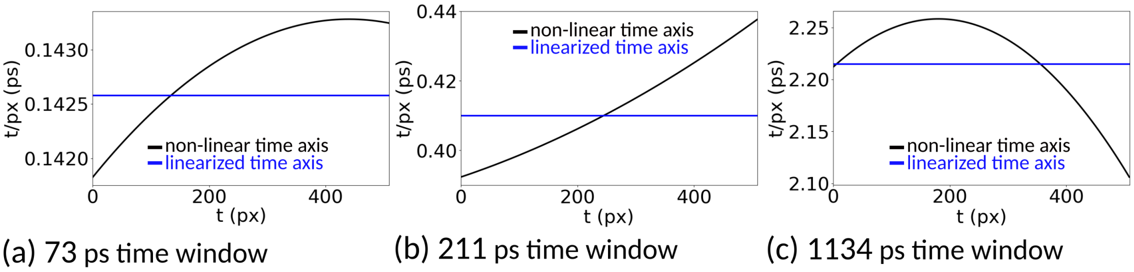

(a) 73 ps time window (b) 211 ps time window (c) 1134 ps time window

Figure 3.5.2: Time axis of the streak camera before (black line) and after (blue line) linearization. Horizontal axis represents the time axis in pixels, vertical axis – time range per pixel. Time window of the streak camera is: (a) 73 ps, (b) 211 ps and (c) 1134 ps.

here.

Background subtraction

All the streak camera images have a background that affects the results of the analysis, e.g., alters bunch centroid position, and therefore has to be subtracted. The background mainly consists of a bias level of the CMOS camera, readout and hot pixel noise. This background is uniform and is independent from the parameters of the streak camera such as MCP gain, time window or slit width. An example of a streak camera background image is given in Fig. 3.5.3(a). A corresponding histogram showing the distribution of number of counts per pixel is displayed in Fig. 3.5.3(b). The pixels of this image have the count value with rms variation of 409 ± 7. In order to reduce the noise added to the data after background subtraction (see Fig. 3.5.3(c)), eight images are averaged to obtain the final background distribution of 408 ± 3 counts per pixel, respectively. This distribution is subtracted from all the data presented in this work.

In the presence of the proton bunch, due to its interaction with the material of diagnostics inserted in the beam line, an additional source of background arises. This radiation background is randomly distributed and results in appearance of clusters of bright pixels across the image, therefore it cannot be properly subtracted. In the analysis of the data, a median filter is applied to obtain smoother curves. The average number of counts of this background constitutes 5 – 8% of the average proton bunch signal value.

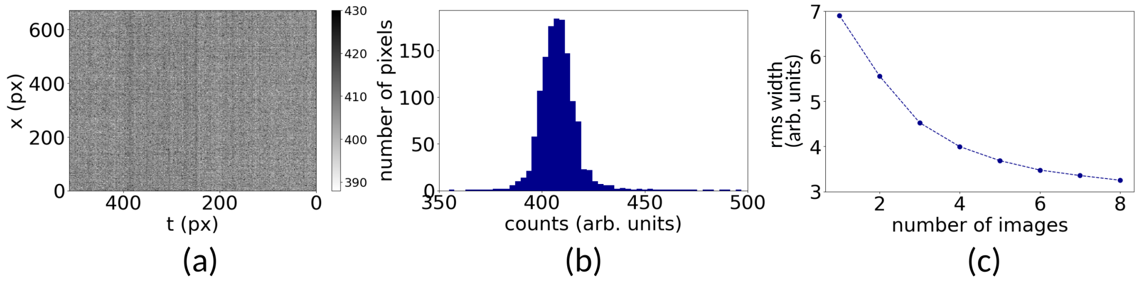

Figure 3.5.3: (a) An example of a time-resolved image, where no signal is being present, that shows the background of the CMOS camera embedded into the streak camera system. The background is uniform and constant in time. (b) Distribution of number of counts per pixel of (a). (c) Rms variation of the number of counts per pixel as a function of number of averaged background images. Eight images are averaged in order to obtain final background distribution.

3.5.2 Time resolution measurement

In order to maximize the light yield on the streak camera images, while preserving the time resolution and keeping the noise level low, we determine optimal operational parameters of the camera. These parameters are the entrance slit width and the MCP gain. Increasing the slit width leads to higher light intensity, however, this results in a decrease in the time resolution of the camera, due to imaging of the slit itself and conversion of its width into time, and to possible space-charge effects in the streak tube. The light intensity on the image, as well as the noise, increase with MCP gain, but an effect on the time resolution is not expected. We measure the time resolution of the streak camera as a function of the slit width and the MCP gain. The ranges of these parameters that were used can be found in Tables 3.5.1 and 3.5.2.

For time-resolved measurements, we use the $\sim$ 110 fs-long reference laser pulse (see Section 3.3), that is much shorter than the expected time resolution (0.81 ps, [91]). Therefore, the measured pulse length would determine the resolution limit. We image this pulse in the time window of 73 ps. We note that the time resolution decreases with the increase of the time window, since each pixel of the image corresponds to a larger time range. We define the time resolution as a full width at half-maximum (FWHM_t) of the longitudinal (time) profile of the laser pulse.

Figure 3.5.4(a) shows two time-resolved images of the reference laser pulse, with a slit width of 10 μm (top image) and of 200 μm (bottom image). The MCP gain is

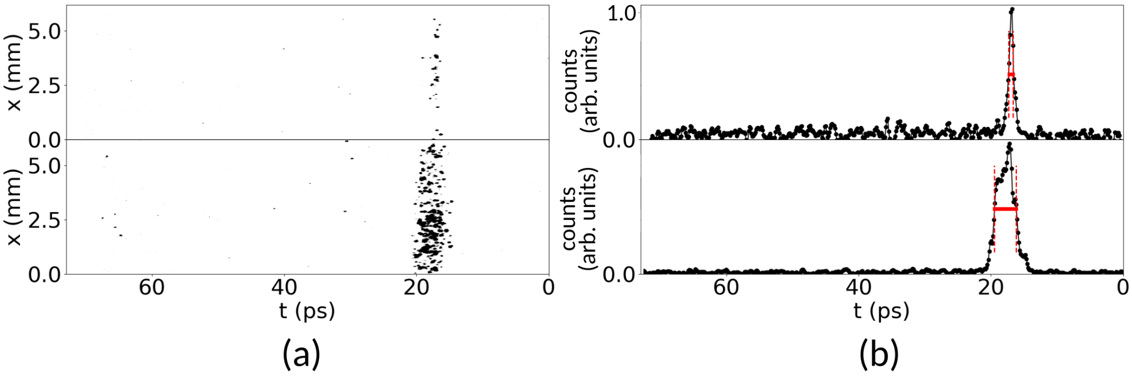

Figure 3.5.4: (a) Time-resolved single images of a reference laser pulse with the duration of 110 fs. The time window length is 73 ps. The slit width of the streak camera is: top image – 10 μm, bottom image – 200 μm. The MCP gain is equal to 30 and is constant for this data. Images have the same color scale. (b) Black line – corresponding temporal profiles of the laser pulse for these two values of the slit width. The FWHM of the profiles is represented by the red dashed and solid lines.

30 and is the same for these images. The images show that the light yield and the measured temporal width of the signal increase with slit width. This can be also observed on the corresponding temporal profiles of the pulse that are shown in Fig. 3.5.4(b) (black line) and their FWHM$_t$ (red line).

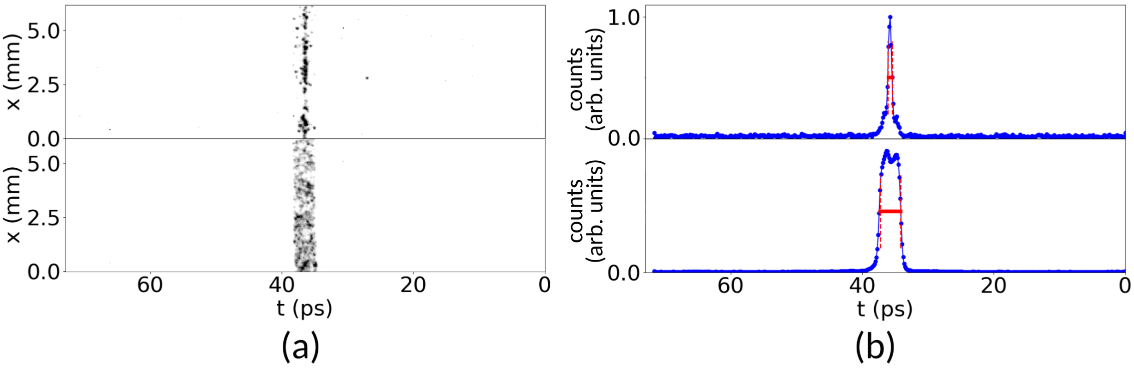

Figure 3.5.5: (a) Time-integrated single images of the entrance slit of the streak camera illuminated by a uniform blue light source. The slit width of the streak camera is (as in Fig. 3.5.4): top image – 10 μm, bottom image – 200 μm. The MCP gain is equal to 30 and is constant for this data. Images have the same color scale. (b) Blue line – longitudinal profiles of the illuminated slit corresponding to images in (a). The FWHM of the profiles is visualized with the red dashed and solid lines. We note that the horizontal axis is converted into time units for convenience.

In order to determine the minimum resolution at a given slit width, we image the slit itself, illuminated by a uniform blue light source. We note that this measurement is time-integrated, but we convert the horizontal axis into the time axis of the 73 ps window. Similarly to Fig. 3.5.4, we show two time-integrated images of the slit with the width of 10 μm (Fig. 3.5.5(a), top image) and of 200 μm (Fig. 3.5.5(a), bottom image). The MCP gain is set to 30 and is not varied, as in the time-resolved measurements. Corresponding longitudinal profiles and their FWHM$_t$ are shown in Fig. 3.5.5(b).

Slit width [μm]	10	20	30	50	75	100	125	150	175	200
Laser pulse FWHM$_t$, [ps]	1.05	1.21	1.23	1.63	1.88	2.25	2.42	2.53	3.01	2.98
Slit FWHM$_t$, [ps]	0.63	0.70	0.87	1.20	1.68	2.16	2.60	2.87	3.11	3.08

Table 3.5.1: The range of the slit width values and corresponding average FWHM$_t$ of the reference laser pulse and of the illuminated slit (black and blue points of Fig. 3.5.6). The conversion factor for the time axis is 0.14 ps/px.

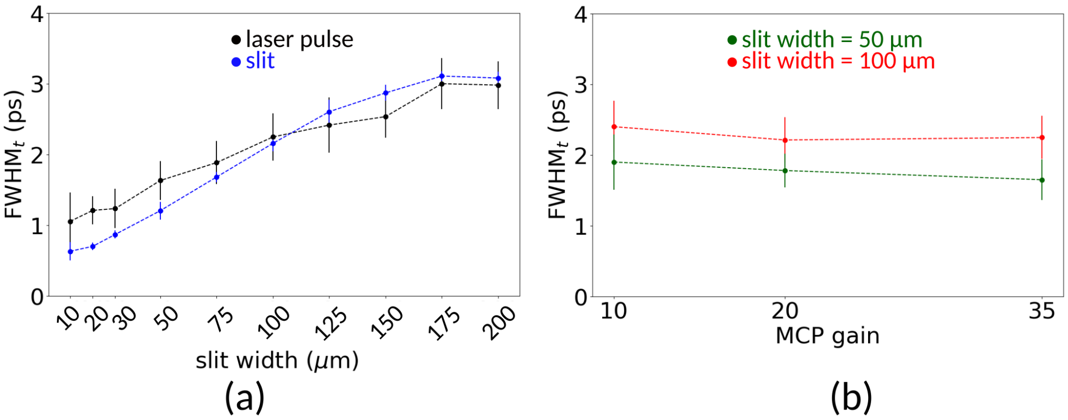

Figure 3.5.6: (a) Average FWHM$_t$ of the reference laser pulse (black points) and of the slit illuminated with the uniform blue light (blue points) as a function of the slit width. (b) Average FWHM$_t$ of the reference laser pulse as a function of the MCP gain, measured with the slit widths of 50 (green points) and 100 (red points) μm. The FWHM$_t$ of the laser pulse is obtained by averaging 20 time-resolved images. The duration of the time window is 73 ps. The measurement of the illuminated slit is time-integrated: the obtained values are converted into the time units for convenience. These values are averages of 5 images. The error bars represent rms variations of the measurements.

Figure 3.5.6(a) shows the FWHM$_t$ of the reference laser pulse averaged over 20 events (black points), and that of the slit illuminated with the uniform light, averaged over five events (blue points). Error bars represent rms variations of the measurements.

With the smallest slit width (10 μm), the intensity of the incoming light of the laser pulse is low, which leads to larger variation in the data and the measurement being less reliable. With the widths of 20 and 30 μm the FWHM$_t$ remains essentially the same. This could be identified as the resolution limit. The FWHM$_t$ increases with slit widths larger than 30 μm, except at largest values (175 and 200 μm), possibly due to the non-uniform illumination. The FWHM$_t$ of the illuminated slit represents the minimal time resolution possible at a given width. These values are therefore expected to be lower than the ones obtained with the laser pulse. This is confirmed in the measurements within the rms variations of the data (blue line, Fig. 3.5.6(a)). The slit FWHM$_t$ increases with the width, except the largest width value (200 μm). Overall, we conclude that for the best time resolution the streak camera has to be operated with the slit width of 20 or 30 μm. The slit width of 20 μm is used in the experiments presented in this thesis.

MCP gain	10	20	35
Slit width [μm]	50		
Laser pulse FWHM$_t$, [ps]	1.90	1.78	1.65
Slit width [μm]	100		
Laser pulse FWHM$_t$, [ps]	2.39	2.21	2.25

Table 3.5.2: The average FWHM$_t$ of the reference laser pulse as a function of the slit width and of the MCP gain (green and red points of Fig. 3.5.6).

We vary the MCP gain, another parameter that affects the light intensity, with the slit widths fixed at 50 and 100 μm. The results (Fig. 3.5.6(b)) show that, as expected, the FWHM$_t$ of the laser pulse (that is, the time resolution) is essentially the same within the rms variations in the range of the MCP gain values from 10 to 35, with both slit widths. We therefore assume that further increasing the MCP gain does not affect the time resolution. In the experiments presented here, MCP gain of 40 is used.

3.5.3 Spatial resolution measurement

We measure the spatial resolution of the optical system used with the streak camera, to determine how well can the spatial features be resolved. We illuminate the USAF 1951 target with the uniform blue light source and image it in the plane of the OTR screen, then transport the image to the streak camera. For the resolution measurement, we use third subgroup of lines in group zero (1.26 line pairs per mm) of the target. The profile of the lines (time-integrated imaging, slit width of 200 μm and MCP gain of 30) obtained by summing the signal in a narrow ($\sim 90\mu$m) range is shown in Fig. 3.5.7(a) (red line). We define a square-shaped signal corresponding to the lines (black line), and, assuming Gaussian response of a point light source, we convolve it with a Gaussian function. We determine the modulation transfer function (MTF) of the signal (Fig. 3.5.7(b), red line), and of the result of convolution (Fig. 3.5.7(b), green dashed line) as a function of the response function rms σ_{Gauss}.

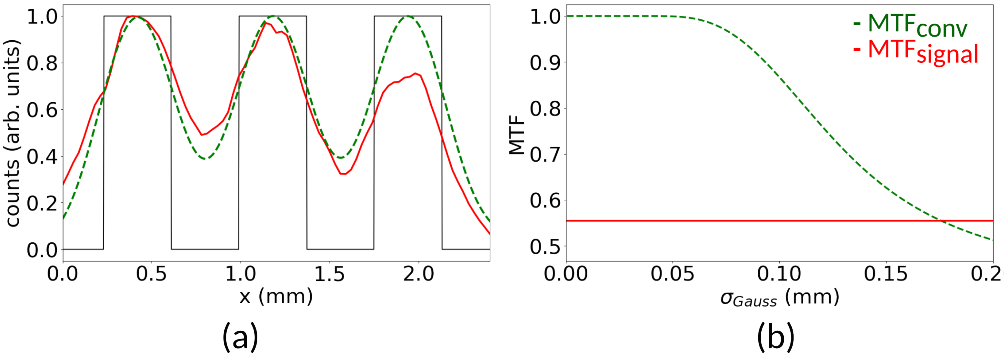

Figure 3.5.7: (a) Red line – the signal of the illuminated USAF target lines summed in a narrow ($\sim 90\mu$m) range, black line – corresponding square-shaped signal representing "ideal" lines, green dashed lines – convolution of the square-shaped signal and a Gaussian function representing a point light source that matches the MTF of the signal. The rms of this function defines the spatial resolution of the optical system. (b) Green dashed line – MTF of the convolution of the Gaussian function and the square-shaped signal (as in (a)) as a function of σ_{Gauss}, red line – MTF of the measured signal. The spatial resolution is the σ_{Gauss} at the intersection of these lines.

Spatial resolution is defined as a σ_{Gauss}, where the MTF of the convolution matches that of the signal. Given that the MTF of the signal is ~ 0.55, we find the spatial resolution $\sigma_{Gauss} \approx 0.18$ mm.

3.6 Upgrade and possible applications of AWAKE

To accelerate an electron bunch with an energy spread and emittance sufficiently low for high-energy physics applications, the AWAKE experimental setup will be upgraded (Fig. 3.6.1, no diagnostics is shown) [92].

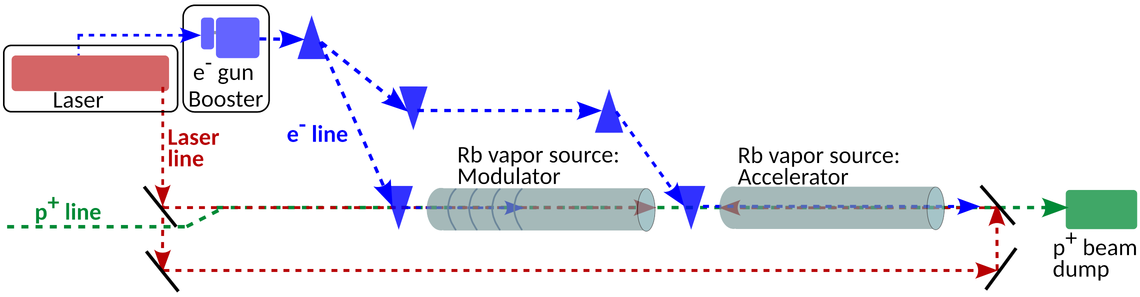

Figure 3.6.1: Schematic of the AWAKE experimental setup after the upgrade (not to scale). Diagnostics is not shown.

Two Rb vapor sources will be used, both 10 m-long. The first source (modulator) allows for a density step, variable in height and location along the plasma, and will be used for seeding SM of the proton bunch. The density step allows to preserve the wakefields for longer distance at a large fraction of the maximum amplitude [93]. The second source (accelerator) is similar to the one used for the experiments presented here. The witness electron bunch will be on-axis injected into it, thus, into the wakefields of the fully-modulated proton bunch.

The studies will focus on the preservation of incoming normalized emittance, low energy spread and matching of the electron bunch to the focusing force of the ion column.

Multiple proposals for applications of AWAKE in the field of high-energy physics are outlined in [94]. The electron bunches, that will be produced at AWAKE, will have tens or even hundreds of GeV energy and transverse emittance below 10 mm·mrad. The repetition rate of the current proton drivers is limited, limiting the resulting luminosity. Thus, applications, that are not critically dependent on the luminosity, are considered. These are, e.g., a dark photon search experiment, where such photons would be produced from electron bunches interacting with a fixed solid target. The electron bunches at AWAKE will have higher population than currently available in the experiments [95], allowing for expansion of the search. Another possible application is a study of the strong-field quantum electrodynamics (QED), colliding electron bunches with high-intensity laser pulses. Finally, an electron-proton collider is considered [96]. A proton bunch, produced by the LHC, will be used as a driver, to accelerate electron bunches to 3 TeV. These will be collided with the counter-propagating 7 TeV proton bunches, produced by the LHC, allowing for the center-of-mass energy of 9 TeV. In this collider, a new regime in deep inelastic scattering and, generally, in quantum chromodynamics (QCD), could be studied.

Chapter 4

Experimental results

This chapter presents the main experimental results of the thesis. In order to characterize hosing and SM, we define the bunch centroid position and the longitudinal on-axis profile as a function of time along the bunch. We then introduce hosing and SM occurring simultaneously as a result of misalignment of initial wakefields driven by the electron bunch. We observe the two processes either with the two streak cameras capturing perpendicular planes, or with a method that allows for reconstruction of the 3D distribution of the proton bunch. We perform frequency analysis of the two processes at two plasma densities. For this, we use the discrete Fourier transform (DFT), as well as the continuous wavelet transform (CWT). We show that bunch centroid position oscillation in case of hosing and modulation in case of SM are at frequencies similar to each other and to that of plasma electrons, as expected from theory. We demonstrate that the development of hosing depends on the direction of misalignment between the two bunches. When the electron bunch is misaligned to the opposite side of the proton bunch axis, the resulting centroid position oscillation is reflected with respect to the bunch axis. We study the dependency of hosing on the proton bunch charge and misalignment extent. We compare experimental observations of hosing with a theoretical model. We show that there is a good agreement between those, despite certain differences between the experimental conditions and the theoretical assumptions. These measurements represent the most comprehensive characterization of hosing in the context of plasma-based acceleration.

We note that in this chapter the misalignment extent is expressed in units of the cold plasma skin depth c/ω_{pe}.

4.1 Characterization of hosing and SM

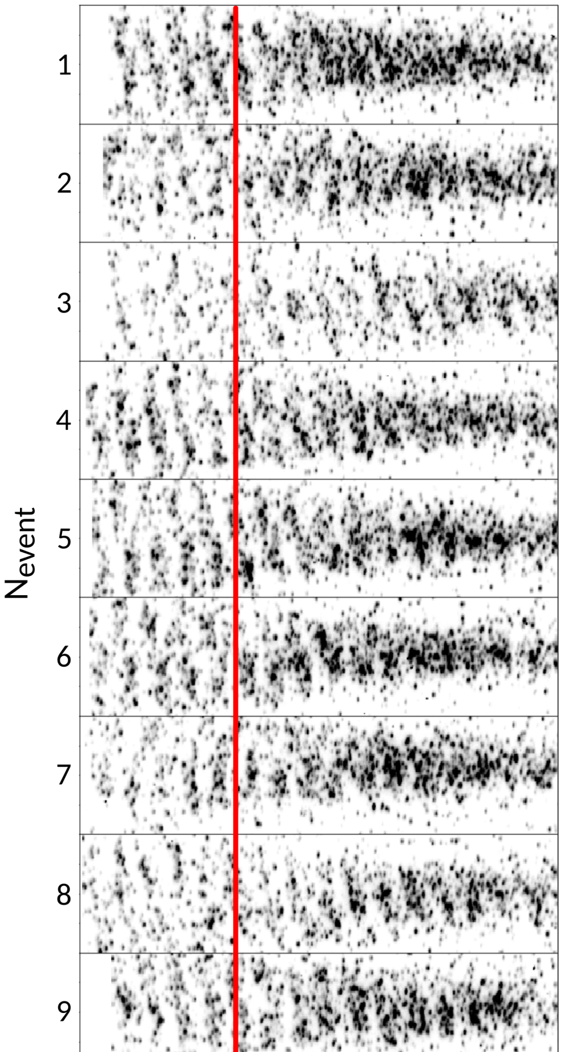

Figure 4.1.1: Waterfall plot of ten consecutive time-resolved images of the proton bunch charge density distribution in case of hosing. The images are aligned in time using the reference laser pulse (red line), then summed and averaged to obtain the final distribution.

We introduce the procedures that will be applied to the time-resolved and time-integrated data for the rest of this chapter. As mentioned in Section 2.3.1 and

Section 2.3.2, when seeded with the electron bunch, both hosing and SM are expected to be reproducible in time from event to event. Therefore, for further analysis we obtain the time-resolved images by summing and averaging over around 10 single events (Fig. 4.1.1) that are aligned in time with the reference laser pulse (not shown, position marked with red line in Fig. 4.1.1). Time t = 0 for all the images presented here is chosen to be 279 ps ($\sim 1.3\sigma_t$) ahead of the the proton bunch longitudinal center. We note that a 1.2×0.07 [ps, mm] median filter is applied to the time-resolved images to obtain smoother centroid position and longitudinal profile curves (the images themselves are shown without filtering).

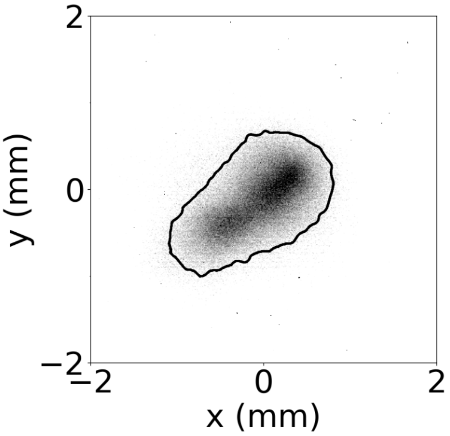

Figure 4.1.2: Time-integrated image of the transverse proton bunch charge distribution in case of hosing (one of the events in Fig. 4.1.1). Median filter is applied to the image. Initially round, the distribution is elongated in the plane of hosing. Black line – 3σ-contour of the distribution.

Time-integrated image of the proton bunch transverse charge distribution corresponding to one of the events in Fig. 4.1.1 is shown in Fig. 4.1.2. We construct the 3σ-contour (at 1% of the maximum intensity) of the distribution (black line) and, for each average time-resolved image, we display a set of corresponding single-event contours. This allows to check for reproducibility of the plane of hosing from event to event. A 0.01×0.01 [mm] median filter is applied to the time-integrated data to reduce the noise and obtain smoother contour curves (image in Fig. 4.1.2 is shown with the filter applied).

4.1.1 Bunch centroid position and longitudinal profile

We define two main characteristics of hosing and SM – the bunch centroid position x_c (y_c) and the modulated longitudinal density profile, respectively. For both, we need to determine the bunch propagation axis and the region of interest (ROI), since the signal is only present in a limited area of the time-resolved images. The propagation axis x_{ax} (y_{ax}) is defined by the position of the peak (average) of a Gaussian fit to the transverse profile of the time-resolved charge density distribution in the $\sim$ 30 ps region at the head of the bunch, where neither SM nor hosing are clearly developed and affect the calculation (not shown on the images). The ROI for the centroid position r_c is defined as a region where the signal value is equal to, or higher than 4% of the maximum, that is approximately ±1.5 or ±3 mm around the bunch propagation axis, depending on the maximum amplitude of the x_c oscillation (larger with higher proton bunch charge). Considering larger ROI does not lead to any significant change in the centroid position calculation. Limiting ROI is also needed to avoid unwanted signal from the reference laser pulse, positioned at the top of each image. The longitudinal bunch density profile in case of SM is determined within the bunch core radius r_m. The bunch core is defined as the transverse rms size of the proton bunch propagating in vacuum, at the OTR screen, determined from time-resolved images. The corresponding $r_m = 0.24$ mm or $r_m = 0.31$ mm, depending on the size of the proton bunch at the OTR screen.

The centroid position of the bunch is defined as:

$$x_c = \frac{\sum\limits_{i=x_{ax}-r_c}^{x_{ax}+r_c} |i \cdot I(t,i)|}{\sum\limits_{i=x_{ax}-r_c}^{x_{ax}+r_c} I(t,i)} - x_{ax} \quad \text{for all t}, \tag{4.1}$$

where $I(t,i)$ – the intensity of the signal in a pixel of the image, t being the time, and i – the space coordinates of the pixel. This calculation is performed for each pixel column along the time axis of the image.

The bunch density profile (modulation) is defined as the signal summed longitudinally (along the time axis) in its respective ROI and normalized:

$$\frac{\sum\limits_{i=x_{ax}-r_m}^{x_{ax}+r_m} I(t,i)}{\max \sum\limits_{i=x_{ax}-r_m}^{x_{ax}+r_m} I(t,i)} \quad \text{for all t.} \tag{4.2}$$

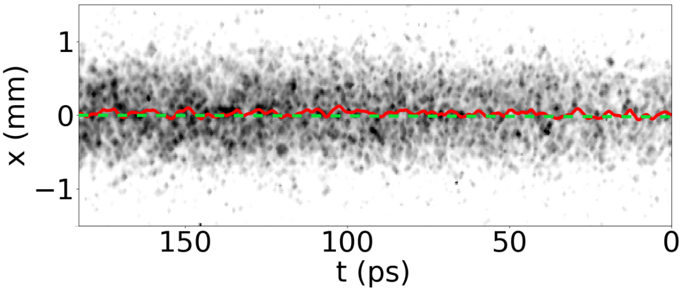

Figure 4.1.3: Averaged time-resolved image of the proton bunch charge density distribution in case of propagation in vacuum. Dashed green line – x_{ax}, solid red line – x_c of the bunch. $Q_p = (14.9 \pm 0.1)$ nC. All images have the same color scale.

We can now apply the above definitions to the data. We begin from introducing the time-resolved charge density distribution of the proton bunch with a charge $Q_p = (14.9 \pm 0.1)$ nC (average value with rms variation of the measurement) propagating in vacuum (Fig. 4.1.3). This distribution is continuous. The x_c of the bunch is shown as a solid red line and evidently exhibits no periodic oscillation, remaining close to the bunch propagation axis (dashed green line).

Next we show experimental observation of hosing and SM developing simultaneously. A corresponding experimental setup is shown in Fig. 4.1.4(a). In order to induce hosing, we introduce a misalignment $\Delta x = (0.95 \pm 0.16)\ c/\omega_{pe}$ of the seed electron bunch trajectory with respect to the proton bunch propagation axis, in the x-direction of the streak camera coordinate system. The Δx is the difference between the two averaged bunch position values, corresponding to the aligned and offset cases, and the error bar represents the position jitter of both the electron and the proton bunches, in both x- and y-directions, summed in quadrature. The value of Δx is larger than the position jitter of the bunches. The two streak cameras capture images in perpendicular planes. The plasma electron density is $n_{pe} = 0.96 \times 10^{14}$ cm^{-3}. Figure 4.1.4(b) shows typical averaged time-resolved distributions corresponding to the simultaneous occurrence of hosing in the plane of misalignment (x, top image) and of SM in the perpendicular plane (y, bottom image). The processes are reproducible

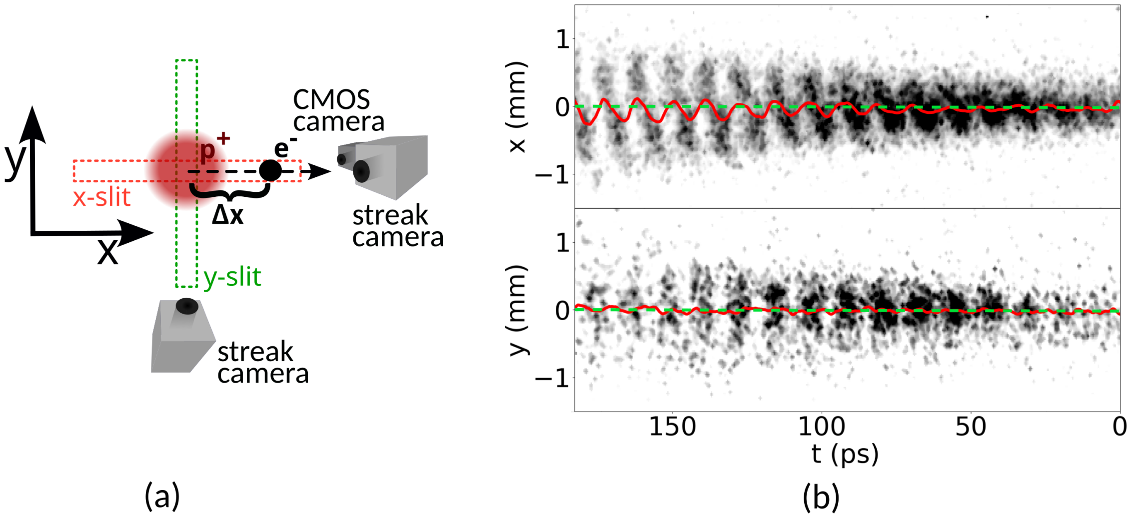

Figure 4.1.4: (a) Illustration of the experimental configuration used for (b). (b) Averaged time-resolved images of the proton bunch ($n_{pe} = 0.96 \times 10^{14}$ cm^{-3}, $Q_p = (14.9 \pm 0.1)$ nC, $\Delta x = (0.95 \pm 0.16)\ c/\omega_{pe}$): top – in the x-plane showing hosing, bottom – in the y-plane – SM. Images have the same color scale. Dashed green line – bunch propagation axis, solid red line – x_c (top) and y_c (bottom).

from event to event, as is seen from the averaged images. Corresponding centroid positions x_c and y_c are displayed with red lines on top of the distributions. The x_c clearly oscillates with growing amplitude (up to 0.28 mm) along the bunch in the plane where hosing occurs. On the contrary, y_c in case of SM, similarly to the propagation in vacuum, remains close to the bunch axis (within ± 0.05 mm) and does not exhibit any periodic pattern. We note that the amplitude of x_c oscillation in case of hosing is ~ 3 times lower than the amplitude of the bunch envelope oscillation (Fig. 4.1.4(b), top), similarly to hosing developing as an instability observed in [63]. The oscillation also exhibits a certain degree of asymmetry with respect to the bunch axis, characteristic of the simultaneous development with SM (more detailed discussion of the asymmetry is given in Section 4.5.2). A comparison of the bunch centroid positions for the data introduced above is shown in Fig. 4.1.5(a), solid grey line – propagation in vacuum, dashed black line – hosing, solid green line – SM.

Figure 4.1.5(b) shows the bunch longitudinal density profiles for the three images in Fig. 4.1.3 and Fig. 4.1.4(b). When the bunch propagates in vacuum (solid grey line), its density is continuous and the intensity of the summed signal increases from head to the longitudinal peak of the bunch, due to its incoming Gaussian distribution.

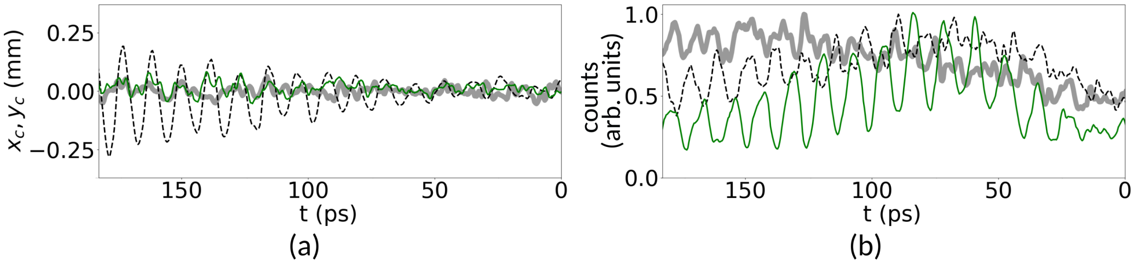

Figure 4.1.5: $Q_p = (14.9 \pm 0.1)$ nC, $n_{pe} = 0.96 \times 10^{14}$ cm^{-3} and $\Delta x = (0.95 \pm 0.16)\ c/\omega_{pe}$ (where applicable). (a) Bunch centroid position in case of propagation in vacuum x_{c0} – solid grey line, SM (y_c) – solid green line, both remaining near the bunch axis, and hosing (x_c) – dashed black line, exhibiting a clear oscillation growing along the bunch. (b) Bunch longitudinal density profile obtained in the bunch core radius, color scheme is the same as in (a). The signal is continuous in case of bunch propagation in vacuum, while there is a pronounced modulation in case of both hosing and SM.

In case of hosing (dashed black line) and SM (solid green line), there is a clear modulation of the distribution. After propagation in plasma, the intensity of the signal is generally higher close to the head of the bunch, due to global focusing, and then decreases, as more protons become defocused and leave the region around the axis. The depth of modulation in case of hosing is lower than that of SM, as the sum includes both parts of the oscillation, above and below the bunch axis. For the same reason the second harmonic can be observed in the signal (e.g., from 60 ps). We note that, in order to include the effect of the second harmonic, we use larger ROI for this profile, than the one used for SM.

4.1.2 Plane of hosing development

Hosing manifests itself not only as a centroid oscillation in time, but also as an elongation of the (initially round) bunch transverse time-integrated profile. This elongation corresponds to the plane where hosing occurs. In order to establish this plane for the data shown above (Fig. 4.1.4(b)), we use the time-integrated images of the proton bunch charge distribution. We determine the 3σ-contours for every event, as shown in Fig. 4.1.2. The resulting set of single-event contours corresponding to the data in (Fig. 4.1.4(b)) is shown in Fig. 4.1.6(a, black lines). The elongation of the contours is evident, compared to the event where no plasma is present (green line), and also reproducible from event to event, that is, hosing develops in approximately the same plane.

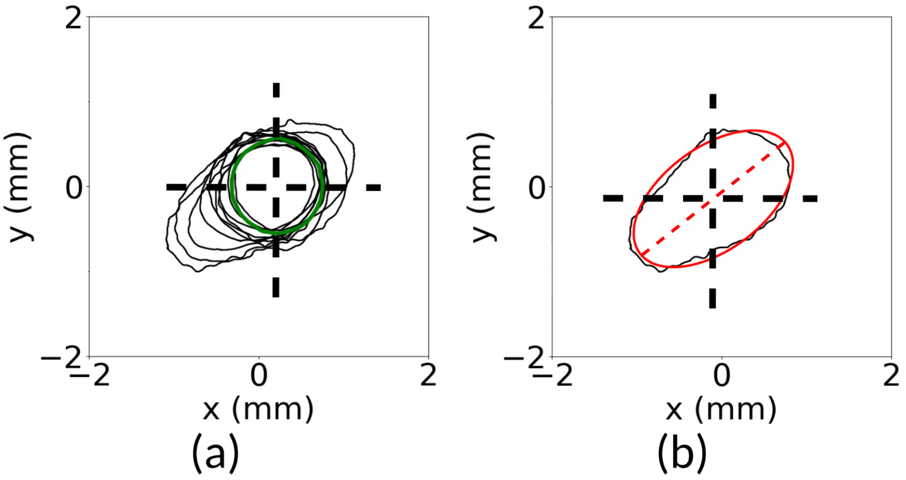

Figure 4.1.6: $Q_p = (14.9 \pm 0.1)$ nC, $n_{pe} = 0.96 \times 10^{14}$ cm^{-3} and $\Delta x = (0.95 \pm 0.16)$ c/ω_{pe} (where applicable). (a) Black lines – single-event time-integrated proton bunch charge distributions of the data shown in Fig. 4.1.4(b) represented as 3σ-contours. The elongation of the contours indicates the plane of hosing development. Green line – contour of the bunch propagating in vacuum. (b) Red line – an example of a least squares fit of an ellipse to a contour of the proton bunch charge distribution (black line). The major axis (dashed red line) defines the plane of hosing development.

The precisely determine the plane of hosing, we perform a least squares fit of an ellipse to each single-event contour, as shown in Fig. 4.1.6(b, red line). The major axis of the ellipse corresponds to the plane of hosing (dashed red line). We note that, as visible in Fig. 4.1.6, the plane of hosing, that is, the plane of the electron bunch misalignment, does not coincide with the assumed x-plane, but is different by an average of ∼ 27.5°. The possible reasons are discussed in more details in Section 4.3.

4.2 3D charge density distribution of the proton bunch

As shown in Fig. 4.1.4, in order to observe hosing and SM developing simultaneously, we use two streak cameras gathering images in the two perpendicular planes. Here, we present a method, that takes advantage of the reproducibility of the results, to observe the two perpendicular planes of the proton bunch with one streak camera. This method allows to reconstruct a 3D charge density distribution of the proton bunch

[97]. In the measurement presented here, $n_{pe} = 0.96 \times 10^{14}$ cm^{-3}, $Q_p = (46.5 \pm 0.6)$ nC and $\Delta x = 1.03 \pm 0.18$ c/ω_{pe}.

Under normal operation conditions, the image of the OTR is centered on the entrance slit of the streak camera to obtain the slice of the distribution around the bunch propagation axis. In order to observe the bunch in the plane perpendicular to the plane of the slit (here – x) we offset the OTR perpendicularly with respect to the slit, thus we obtain images of the proton bunch charge density at different transverse positions across its distribution (Fig. 4.2.1(a)). In the experiment, we change the OTR position on the slit with the last reflecting mirror of the optical transport line in front of the streak camera.

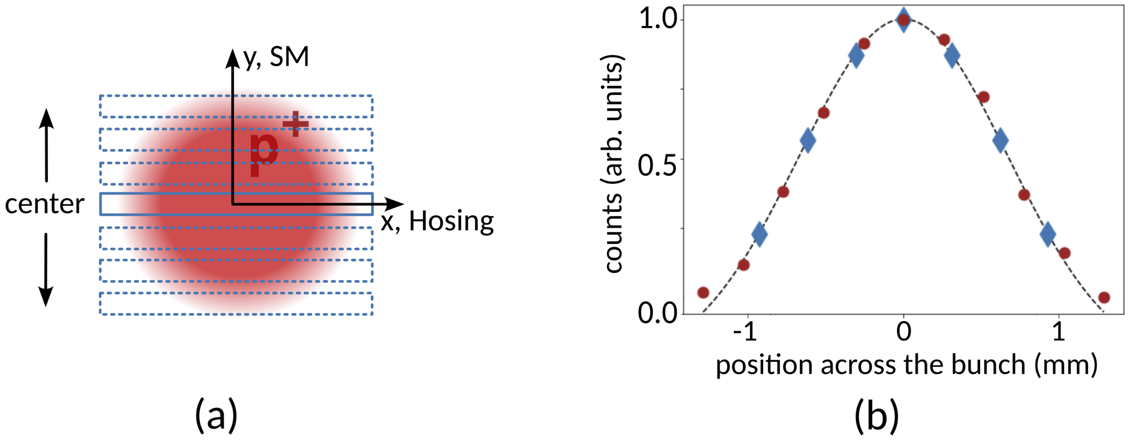

Figure 4.2.1: (a) Schematic of the scanning procedure. We vary the OTR position with respect to the entrance slit of the streak camera, that is equivalent to the change of the slit position across the transverse proton bunch distribution. Blue rectangles indicate various slit positions. (b) Average sum of counts of the time-integrated proton bunch charge density distribution as a function of the position across the bunch. Red points – data, dashed black line – Gaussian fit, blue diamonds – positions across the bunch, where the slices are obtained.

The distance between the mirror and the slit is ~ 0.95 m, and the maximum OTR offset introduced is ~ 0.93 mm. The variation of the proton bunch OTR position on the streak camera slit does not alter the measured duration of the bunch. We can therefore consider the variation of the OTR position with respect to the slit as equivalent to the change of the slit position across the transverse proton bunch distribution (blue rectangles, Fig. 4.2.1(a)).

We determine the central position of the proton bunch OTR on the slit and locate

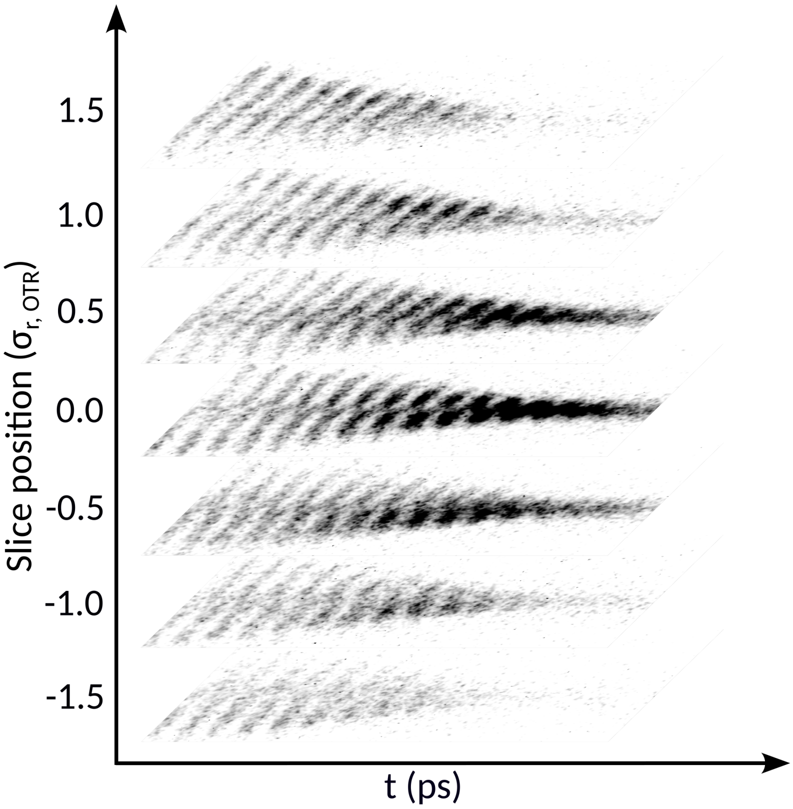

Figure 4.2.2: Slices of the averaged time-resolved proton bunch charge density distribution obtained across the bunch, arranged vertically as a function of the position across the bunch and aligned in time. The intensity of the distribution is the highest in the central slice, decreasing towards the edges of the distribution, due to its Gaussian shape.

the edges of its distribution by varying the mirror angle and obtaining corresponding images of the time-integrated charge density distribution (produced without streaking). We plot the average summed signal (Fig. 4.2.1(b), red points) as a function of the position across the bunch. As already mentioned in Section 3.2, the transverse proton bunch distribution is Gaussian, therefore we perform a Gaussian fit (black dashed line). We use the mirror angular offset corresponding to the maximum value of the Gaussian as the initial position. The rms size of the proton bunch at the OTR screen is $\sigma_{r,OTR} \approx 0.62$ mm (with $Q_p \approx 46.5$ nC). We vary the mirror angle so that we record sets of bunch slices every 0.31 mm or $\sim 0.5\ \sigma_{r,OTR}$ (blue diamonds). This step size is also larger than the spatial resolution of the system.

We start the measurement from the central position of the proton bunch OTR on

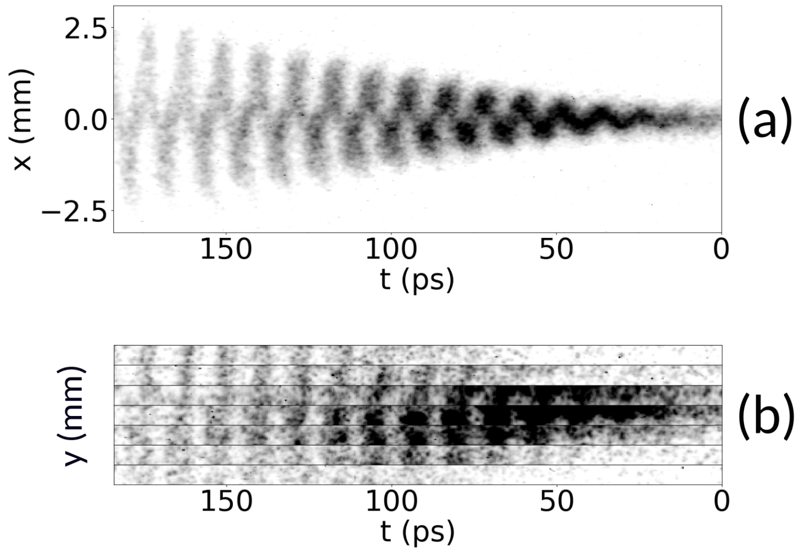

Figure 4.2.3: (a) Time-resolved proton bunch charge density distribution containing an averaged sum of all the slices in Fig.4.2.2. Hosing is induced in the x-plane (plane of the slit of the streak camera). (b) Waterfall plot containing ~ 0.4 mm-wide line-outs of the slices below the bunch propagation axis. The line-outs are arranged vertically like the slices themselves (Fig. 4.2.2) and are aligned in time. The result shows the SM developing in the plane perpendicular to hosing.

the slit. We vary the mirror angle in a way described above to obtain three slices above and three slices below the central (Fig.4.2.1(b), blue diamonds). The slices are obtained by averaging ten single events, as all the data shown in this chapter. Figure 4.2.2 shows the slices arranged vertically as a function of the position across the bunch and aligned in time. The intensity of the proton bunch charge density distribution is the highest in the central slice, decreasing towards the edges of the distribution, due to its Gaussian transverse shape. We then sum and average all the slices to obtain a 2D distribution in the plane of the streak camera slit (x-plane, Fig. 4.2.3(a)). Additionally, to mimic the view of the perpendicular plane, we obtain a waterfall plot of the slices. For better visualization and since we acquired only seven slices of the bunch, instead of showing 1 px-wide line-outs of each slice, we select a narrow (~ 0.4 mm) region near the bunch propagation axis on the same side of it for all the slices (here – below the axis) and arrange these line-outs vertically (aligned in time), as is done the slices themselves in Fig. 4.2.2. The resulting combination (Fig. 4.2.3(b)), obtained by recording images in the plane of hosing, shows the microbunch-like structure, indicating the presence of SM in the perpendicular plane (y-plane).

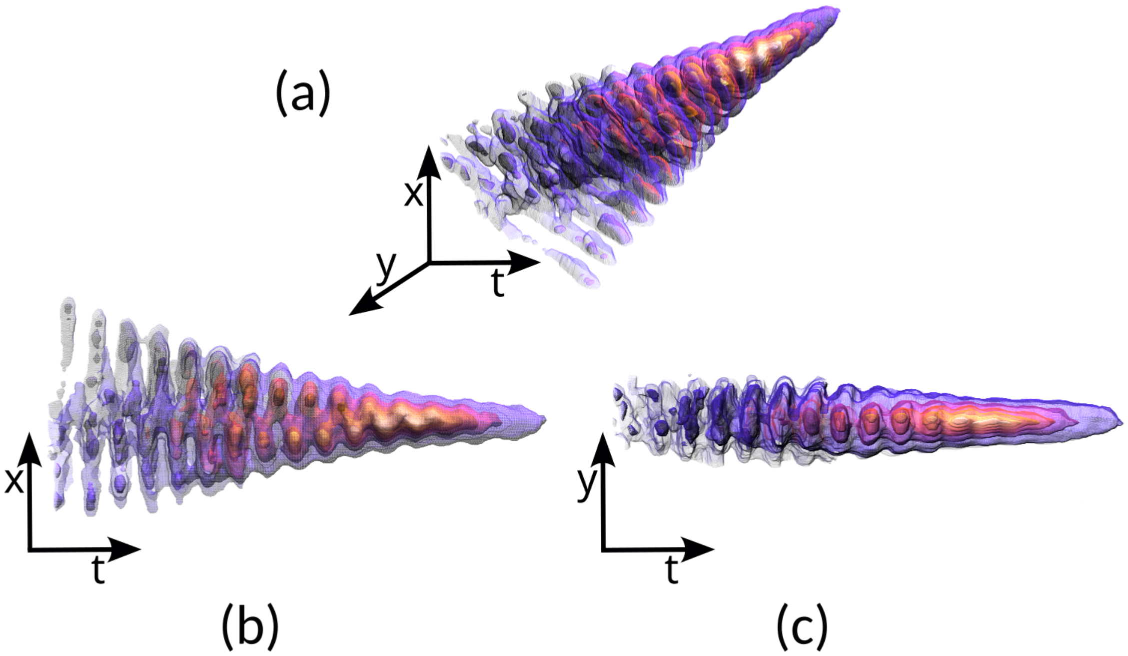

Figure 4.2.4: A 3D proton bunch charge density distribution. (a) Isometric view. Hosing is induced in the x-plane (b), SM develops in y-plane (c).

A 3D proton bunch charge density distribution is reconstructed with the use of the MayaVi scientific data visualizer [98]. It is based on the interpolation between the slices placed in order (as in Fig. 4.2.2) in a linear rectangular grid. Figure 4.2.4 shows the isometric view (a), as well as the x- and y-projections((b) and (c)) of the obtained distribution. The two projections clearly show hosing and SM developing in the perpendicular planes. We note that a 6.6 × 0.3 [ps, mm] median filter was applied to all the slices in order to extensively smoothen the distribution.

4.3 Dependence of hosing on the misalignment direction

Another characteristic of hosing that develops in the induced regime is its dependency on the direction of misalignment, e.g., ± x (Fig.4.3.1(a)). When the electron bunch is misaligned to the opposite side of the proton bunch axis ($+\Delta x \rightarrow -\Delta x$), the wakefield force that acts on each temporal slice of the proton bunch reverses direction (see Fig. 2.3.6). We therefore expect the resulting x_c oscillation to be reflected with respect to the bunch propagation axis.

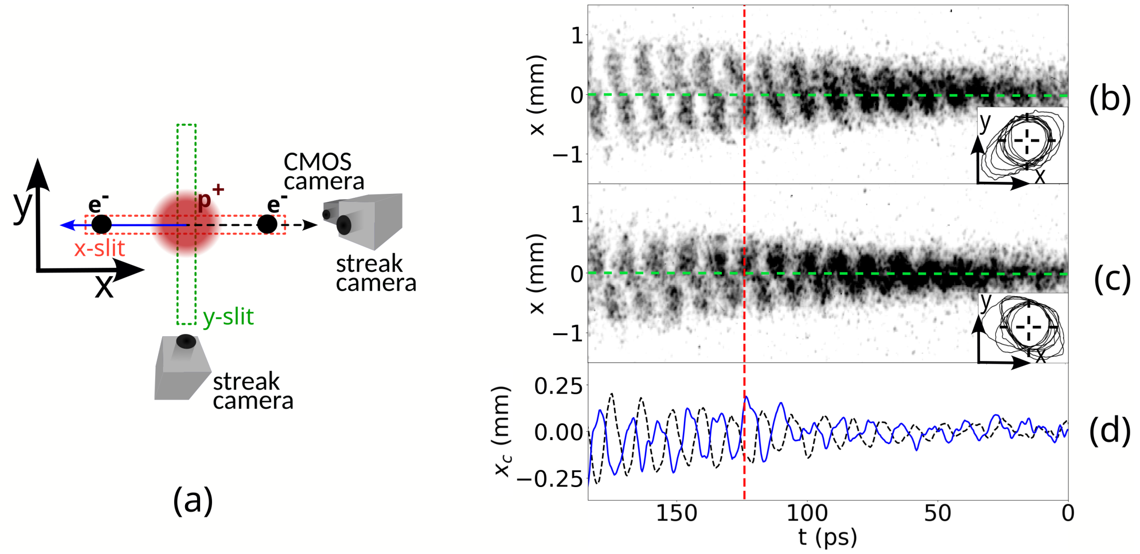

Figure 4.3.1: (a) Experimental configuration for the results presented in (b) –(d). Right hand side – averaged time-resolved images ($n_{pe} = 0.96 \times 10^{14}$ cm^{-3}, $Q_p = (14.9 \pm 0.1)$ nC) with (b) $\Delta x = (0.95 \pm 0.16)\ c/\omega_{pe}$ and (c) $\Delta x = (-0.93 \pm 0.18)\ c/\omega_{pe}$. Images have the same color scale. The reflection of the x_c oscillation is visible, e.g., at $t \approx 124$ ps (dashed red line): the x_c displacement is (a) below and (b) above the bunch axis (x = 0). (d) x_c oscillation curves: dashed black line – top image, solid blue line – bottom image. Insets (b) and (c): single-event 3σ-contours of time-integrated bunch charge distribution.

This reflection is clearly visible on the images in Figs. 4.3.1(b) (same as Fig. 4.1.4(b), top image), (c), and on the corresponding $x_c(t)$ curves (Fig. 4.3.1(d), e.g., at $t \approx$ 124 ps, dashed red line).

Alignment in position and angle between the two particle beams with significantly different parameters is one of the main challenges in these experiments. Single-event 3σ-contours of the proton bunch transverse charge distribution are shown in insets of Fig. 4.3.1(b) and (c). They show that the direction of elongation is in the general direction of misalignment, i.e., x-direction, but with an angle of $26° - 28°$ with respect to it. The contours show that reversing the direction of misalignment ($+\Delta x \rightarrow -\Delta x$) produces a reflection of the angle from $+27.5°$ (inset of Fig. 4.3.1(b)) to 180°–26.2° (inset of Fig. 4.3.1(c)). This indicates a possible angular misalignment in the vertical plane between the trajectories of the two bunches. This misalignment might also be the cause of the different amplitudes of the x_c oscillation in Fig. 4.3.1(d), since the amplitude depends on the misalignment extent Δx (discussed in Section 4.5.1). The accuracy of the available diagnostics was not sufficient to correct this misalignment. Simulation results [63] indicate that the time-resolved images nevertheless retain the main characteristics of both hosing and SM (as in Fig. 4.1.4(b)), even when the observation plane is different from the hosing plane by angles similar to those observed in the experiment.

4.4 Frequency of hosing and SM

We determine the frequencies of the $x_c(t)$ oscillation for hosing (f_H) and of the modulation for SM (f_{SM}) at two plasma densities, $n_{pe} = 0.96 \times 10^{14}$ cm^{-3} (see Figs. 4.1.4(b) and 4.1.5), and $n_{pe} = 2.03 \times 10^{14}$ cm^{-3} (Fig. 4.4.1).

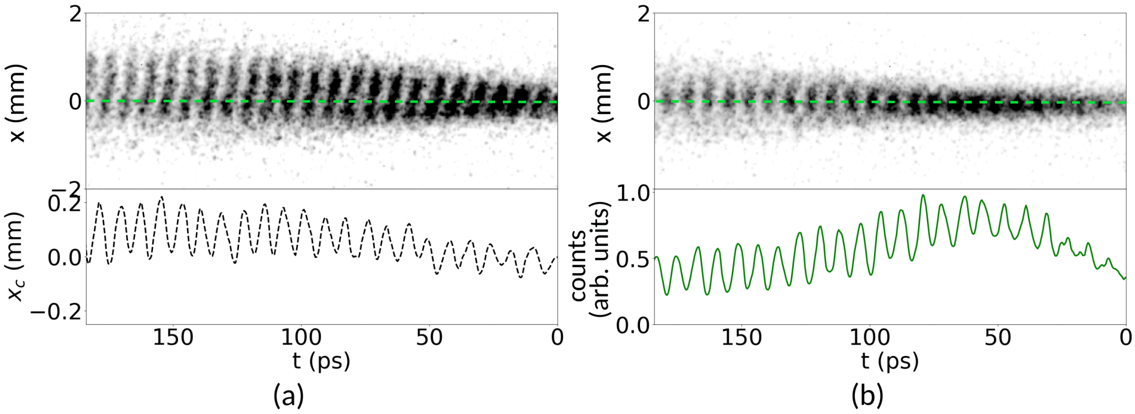

Figure 4.4.1: Averaged time-resolved images ($n_{pe} = 2.03 \times 10^{14}$ cm^{-3}, Q_p = (17.1 ± 0.2) nC) of the proton bunch charge distribution in case of hosing (a) with its respective x_c (dashed black line), and in case of SM (b) with the corresponding longitudinal profile (solid green line). These images are two different sets of events and were obtained in the same (x) plane. We note that SM data of (b) was obtained by misaligning the electron bunch in the y-plane.

The values of Q_p are similar for these measurements, Q_p = (14.9 ± 0.1) nC when $n_{pe} = 0.96 \times 10^{14}$ cm^{-3} and Q_p = (17.1 ± 0.2) nC when $n_{pe} = 2.03 \times 10^{14}$ cm^{-3}. To the lowest order, we expect the frequencies not to depend on the bunch charge. In Fig. 4.4.1(a), $\Delta x = (0.49 \pm 0.15)$ c/ω_{pe}, that is, hosing is induced in the plane of the streak camera slit (x-plane), in (b) $\Delta y = (1.01 \pm 0.17)$ c/ω_{pe}, that is, hosing is induced in the y-plane, perpendicular to that of the streak camera slit. We therefore observe SM in (b). We compare f_H and f_{SM} with the plasma electron frequency f_{pe}, that is determined from the measurements of n_{pe} with the following formula:

$$f_{pe} = \frac{1}{2\pi}\sqrt{\frac{n_{pe}e^2}{\epsilon_0 m_e}}. \tag{4.3}$$

We expect these three frequencies to be similar, since the electron bunch drives initial wakefields, that seed SM and hosing, at f_{pe}.

4.4.1 Discrete Fourier transform

We perform the DFT of the x_c oscillation and of the modulation, for both averaged data and single events. We note that, due to the limited duration of the signals, their corresponding power spectrum is not a δ-function, but a sinc function, since it is convolved with a Fourier transform of the square time window (sinc) function imposed by the streak camera. To find the position of the frequency peak in the spectrum, we set a lower limit on frequency of 30 GHz, to exclude low frequency components originating from the envelope of the signal and not corresponding to the x_c oscillation or modulation. We apply zero padding to the signal, such that its length is equal to 2^n. We use n = 14, as further increasing n does not improve the accuracy of frequency determination. The zero-padded signal length is therefore 16384 px. We note however that zero padding does not enhance the frequency resolution of the DFT, but rather increases the interpolation density between the sample points, that is, improves the precision in finding the position of an isolated peak in the power spectrum.

The DFT power spectra of the averaged x_c oscillation and modulation in the range of (0–180) GHz, as well as the peak frequency values are shown in Fig. 4.4.2, (a) for $n_{pe} = 0.96 \times 10^{14}$ cm^{-3}, and (b) for $n_{pe} = 2.03 \times 10^{14}$ cm^{-3}. Dashed black line corresponds to x_c oscillation in case of hosing, solid green line – to modulation curve of SM. The peak frequency values of hosing and SM are in a good agreement.

The average frequency values of the single-event x_c oscillation f_H and modulation f_{SM} are shown along with f_{pe} in Fig. 4.4.3. Error bars represent rms variations of the data. At $n_{pe} = 0.96 \times 10^{14}$ cm^{-3} (a), $f_{pe} = (87.99 \pm 0.18)$ GHz, $f_H = (86.76 \pm$

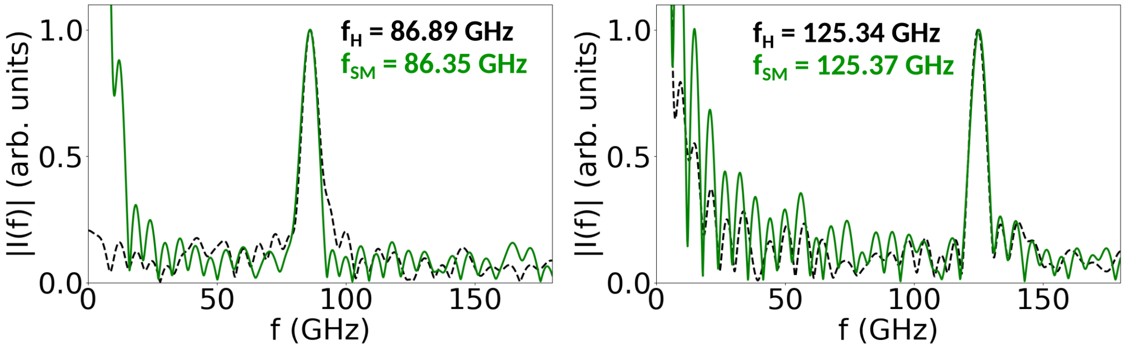

(a) (b)

Figure 4.4.2: DFT power spectra of averaged hosing x_c oscillation (dashed black line) and SM longitudinal profile (modulation, solid green line) and corresponding peak values f_H and f_{SM}. (a) $n_{pe} = 0.96 \times 10^{14}$ cm^{-3}, (b) $n_{pe} = 2.03 \times 10^{14}$ cm^{-3}.

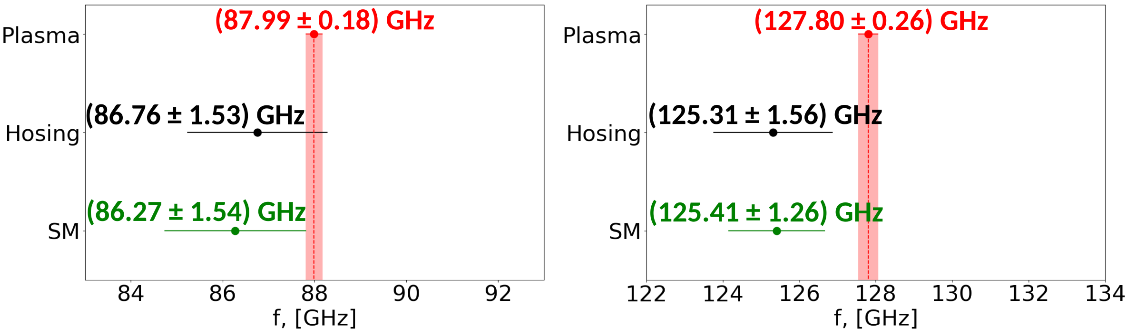

(a) (b)

Figure 4.4.3: Plasma electron frequency (red point), average single-event frequencies of x_c (hosing, black point) and modulation (SM, green point). Error bars represent rms variations of the data. (a) $n_{pe} = 0.96 \times 10^{14}$ cm^{-3}, (b) $n_{pe} = 2.03 \times 10^{14}$ cm^{-3}.

1.53) GHz and $f_{SM} = (86.27 \pm 1.54)$ GHz. Both f_H and f_{SM} are $\sim 1.7\%$ lower than f_{pe}, but are nevertheless similar within the rms variation of the measurement. At $n_{pe} = 2.03 \times 10^{14}$ cm^{-3}, $f_{pe} = (127.80 \pm 0.26)$ GHz, $f_H = (125.31 \pm 1.56)$ GHz and $f_{SM} = (125.41 \pm 1.26)$ GHz. As with the lower plasma density, both f_H and f_{SM} are lower, by $\sim 2\%$, than f_{pe}, however, overall comparable. The possible reasons for that are a discrepancy in the n_{pe} measurement, or, as was shown with numerical simulations [99], the evolution of the wakefields and of the bunch modulation along the plasma, resulting in the modulation frequency to be close to, but not equal to f_{pe}. Similar behavior was observed also at lower $n_{pe} \approx 0.5 \times 10^{14}$ cm^{-3}) [63]. The values of f_H and f_{SM} obtained by averaging single-event values are practically identical to the ones obtained from the averaged dataset.

Overall, we conclude that, as expected, $f_H \approx f_{SM} \approx f_{pe}$ at both plasma densities.

4.4.2 Continuous wavelet transform

In order to assess whether, due to the evolution of the wakefields and of the bunch discussed in [99], there is the evolution of frequency along the bunch that could be determined from the time-resolved images, we perform the CWT on the same signals as in the previous section. We choose the complex Morlet wavelet (complex sine wave tapered by a Gaussian) as mother function for the transform, due to its similarity to the signals of interest and smooth (Gaussian) shape [100, 101]. The central frequency ω_0 (or the number of oscillations within the envelope, see example in Fig. 4.4.4) of the wavelet sets a trade-off between the time and the spectral resolution of the transform and is found through an optimization procedure, such that lower ω_0 value clearly reduces the accuracy of the frequency determination, and higher value results in less time information available, while not significantly improving the frequency determination. We find $\omega_0 = 8$. The set of widths of the daughter wavelets is found from corresponding set of signal frequencies of interest. Zero padding can also be applied to the signal in order to obtain "finer" frequency bins, and is set to n = 13 for this analysis.

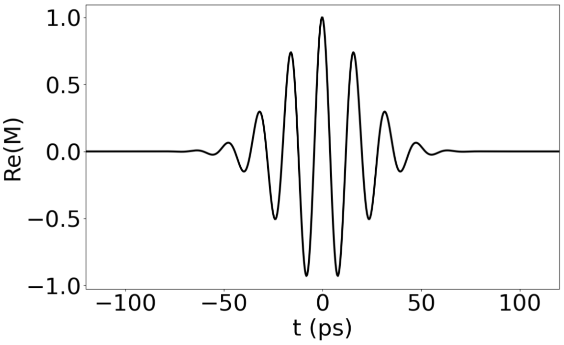

Figure 4.4.4: The real part of the Morlet wavelet function. This part provides the information about the wavelet in the time domain. The central frequency ω_0 represents the number of oscillations within the function itself and is equal to 8 in this example.

An example of the wavelet energy spectrum of the averaged x_c oscillation (data shown in Fig. 4.1.4(b, top image)) is displayed in Fig. 4.4.5, with intensity scaling according to the significance of a given frequency at a given time. This distribution has the highest intensity at $t > 100$ ps, when the oscillation is well-developed.

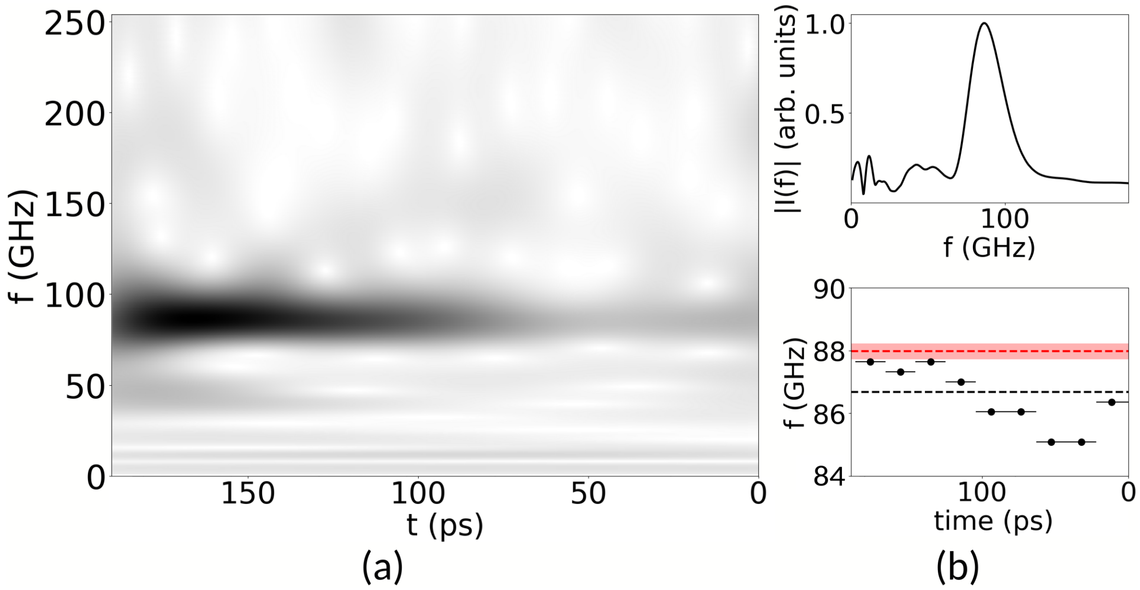

Figure 4.4.5: (a) Wavelet energy spectrum of the averaged x_c oscillation (data in Fig. 4.1.4(b), top) as a function of time and frequency. The intensity scales with the importance of a given frequency at a given location. (b) Top: sum of the signal in (a) along the frequency axis (transverse). The peak is identified at 86.68 GHz. Bottom: black points – frequency values obtained by summing the signal as in the top plot, but in 20-ps time slices, error bars indicate the time slice edges, dashed black line – overall frequency (from the top plot), dashed red line and red area – f_{pe} and corresponding rms uncertainty. $n_{pe} = 0.96 \times 10^{14}$ cm^{-3}.

No significant frequency harmonics or shifts in time are observed. The sum of (a) along the frequency axis is shown in (b, top plot). The peak $f_H = 86.68$ GHz is similar to the result obtained with the DFT. We determine the frequency along the bunch (time) in 20 ps slices (b, bottom plot, black points), and show that, while initially lower than the f_H determined from the whole time window (dashed black line, value from the top plot), with a minimum of $\sim$ 85.08 GHz, the frequency slightly increases after t = 100 ps, to a maximum of $\sim$ 87.64 GHz, where it almost matches the f_{pe} (red dashed line). However, the frequency (of SM, and therefore of hosing) is expected to decrease due to the dephasing between the wakefields and the microbunch structure [99]. We determine the significance of the observed trend below.

As with the DFT, we perform the CWT of the single-event x_c oscillation for hosing and modulation curves for SM (for the same data). We determine the frequency along

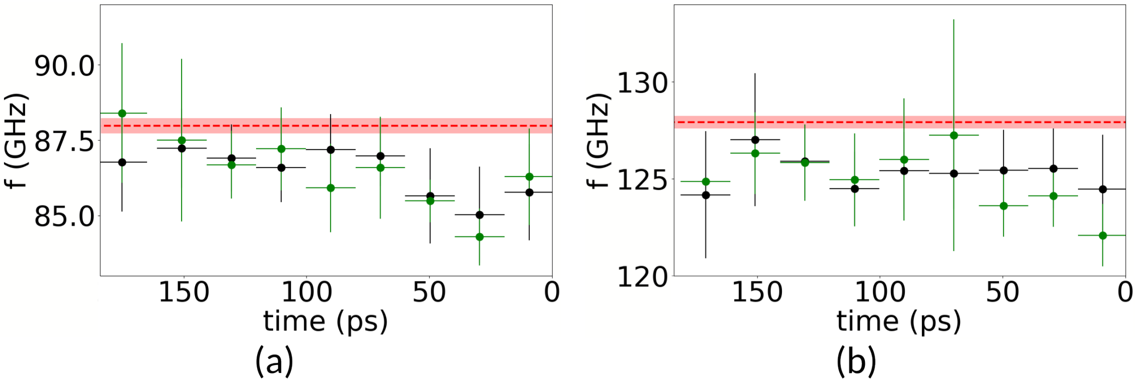

Figure 4.4.6: Plasma electron frequency (dashed red line) and corresponding rms variation (red area), average single-event frequencies of x_c (hosing, black points) and modulation (SM, green points) as a function of time. Error bars in frequency represent rms variations of the data, in time – the time bin size. (a) $n_{pe} = 0.96 \times 10^{14}$ cm^{-3}, (b) $n_{pe} = 2.03 \times 10^{14}$ cm^{-3}. Overall, the data does not show any significant or consistent trend in time.

time, as in Fig. 4.4.5(b, bottom plot). The results, obtained by averaging single-event frequency values, with the respective rms variations, with $n_{pe} = 0.96 \times 10^{14}$ cm^{-3} (Fig. 4.4.6(a)) show that, while there might be a trend for the frequency to slightly increase towards the end of the bunch, it mostly remains within the variations of the measurement. With $n_{pe} = 2.03 \times 10^{14}$ cm^{-3}, we observe no clear trend, the measurements agree within the respective uncertainties. We therefore conclude that no distinct evolution in time of the frequencies of hosing or SM could be determined from the time-resolved images.

Finally, we conclude that the frequencies f_H and f_{SM} obtained with the CWT are close to f_{pe}: $f_H \approx f_{SM} \approx f_{pe}$. This is expected, as hosing and SM are induced by the electron bunch that drives wakefields at f_{pe}.

4.5 Experimental parameters scan

In this section, we study how changes in certain experimental parameters affect the development of hosing, in particular, its amplitude. We determine whether the experimental results agree with the theoretical findings outlined in Section 2.3.2 (Eqs 2.13 and 2.14). All the measurements presented here are performed at $n_{pe} = 0.96 \times 10^{14}$ cm^{-3}.

4.5.1 Variation of electron-proton beams misalignment extent

The evolution along the plasma of transverse initial wakefields driven by the low energy electron bunch with parameters similar to that of the experiment was obtained from numerical simulations [102]. The amplitude of the wakefields as a function of the distance from the bunch axis reaches the peak before $\Delta x = 0.1\ c/\omega_{pe}$ and then monotonically decreases (Fig. 4.5.1). The effect of these wakefields on the centroid position of proton bunch x_c therefore depends on its position with respect to wakefields axis, i.e., on the misalignment extent Δx between the two bunches. Simulation results also indicate that, due to the low electron bunch energy (~ 20 MeV), this bunch drives wakefields of significant amplitude only over the first 2–3 m of plasma.

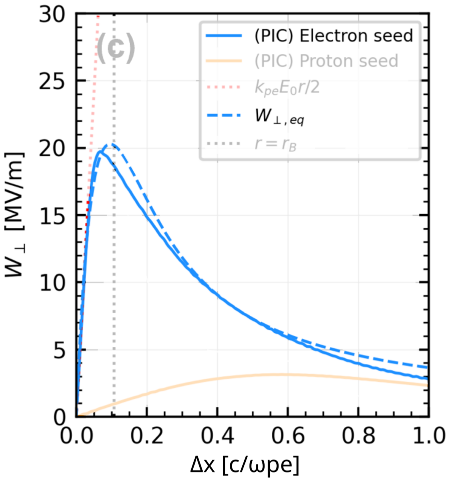

Figure 4.5.1: Amplitude of the transverse wakefields driven by a short low energy electron bunch (with parameters similar to those of the experiment) as a function of distance from the bunch axis (solid blue line, simulation results) [102]. The amplitude peaks at the distance from the axis of $< 0.1c/\omega_{pe}$ and then gradually decreases.

We perform the measurements varying Δx and thus the amplitude of initial wakefields, keeping the other experimental parameters constant ($Q_p = (14.9 \pm 0.1)$ nC). The smallest Δx value is chosen to be larger than the average position jitter of the two bunches (error bar in all Δx values).

Averaged time-resolved images of the proton bunch charge density distribution are shown in Fig. 4.5.2, with misalignment extent increasing from (a) $\Delta x = (0.53 \pm 0.15)\ c/\omega_{pe}$ to (b) $\Delta x = (0.95 \pm 0.16)\ c/\omega_{pe}$ (same as Fig. 4.1.4(b)) to (c)

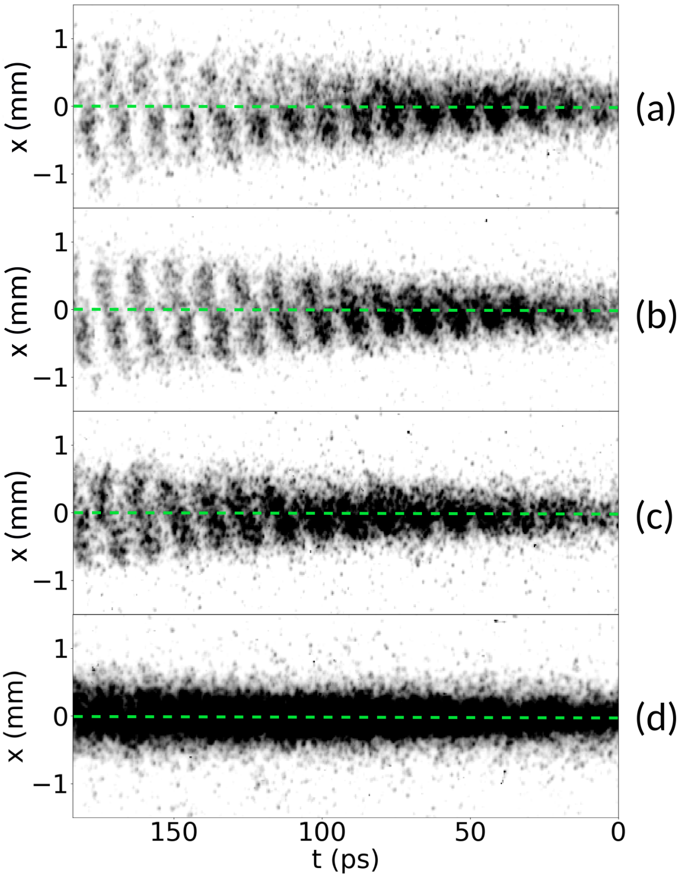

Figure 4.5.2: Averaged time-resolved images of the proton bunch ($Q_p = (14.9 \pm 0.1)$ nC) with (a) $\Delta x = (0.53 \pm 0.15)\ c/\omega_{pe}$, (b) $\Delta x = (0.95 \pm 0.16)\ c/\omega_{pe}$, (c) $\Delta x = (1.47 \pm 0.16)\ c/\omega_{pe}$, (d) $\Delta x = (2.61 \pm 0.17)\ c/\omega_{pe}$. Images have the same color scale. Bunch axis is shown with dashed green line.

$\Delta x = (1.47 \pm 0.16)\ c/\omega_{pe}$ to (d) $\Delta x = (2.61 \pm 0.17)\ c/\omega_{pe}$. In (a) to (c), one can observe a decrease in the amplitude of the bunch envelope oscillation with increasing Δx, in particular at $t > 150$ ps. With the largest misalignment extent (d), the level of the seed wakefields is not strong enough to induce either hosing or SM. Therefore, SM develops in the instability regime: no clear microbunch structure is observed after averaging the data, that is, the process is no longer reproducible from event to event. Moreover, the intensity of the distribution is higher all along the bunch ((c) and (d)) with larger Δx, indicating that there is less overall effect of the wakefields. The bunch distribution remains close to the propagation axis, and, as the streak camera yields the charge density and not the charge, and the amount of light is limited by the entrance slit, the less the bunch evolves under the effect of the wakefields (staying mostly focused), the more light the streak camera captures.

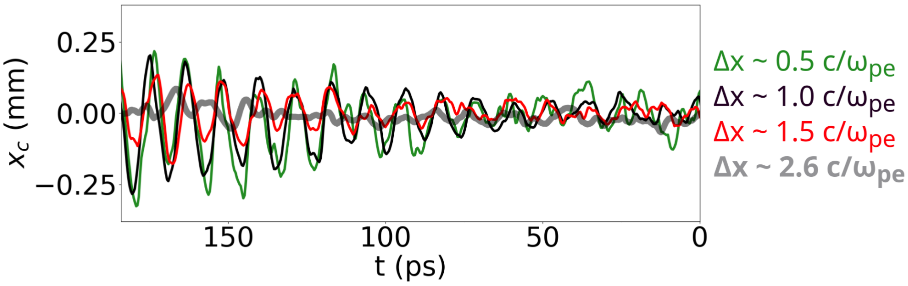

Figure 4.5.3: Proton bunch centroid position $x_c(t)$ ($Q_p = (14.9 \pm 0.1)$ nC). $\Delta x = (0.53 \pm 0.15)\ c/\omega_{pe}$ – green line, $\Delta x = (0.95 \pm 0.16)\ c/\omega_{pe}$ – black line, $\Delta x = (1.47 \pm 0.16)\ c/\omega_{pe}$ – red line, $\Delta x = (2.61 \pm 0.17)\ c/\omega_{pe}$ – grey line.

Corresponding x_c curves (Fig. 4.5.3) confirm the observations outlined above. The amplitude of x_c oscillation decreases as Δx increases ($\Delta x > 0.5\ c/\omega_{pe}$). Measured at $t \approx 163$ ps, it is $x_c \approx 0.198$ mm when $\Delta x \approx 0.5\ c/\omega_{pe}$ (green line), $x_c \approx 0.173$ mm when $\Delta x \approx 1.0\ c/\omega_{pe}$ (black line) and $x_c \approx 0.108$ mm when $\Delta x \approx 1.5\ c/\omega_{pe}$ (red line). With $\Delta x \approx 2.61\ c/\omega_{pe}$, no oscillation is observed, that is, the effect of the seed wakefields is insufficient to induce hosing. When not induced, hosing is only observed as an instability at much lower plasma densities $n_{pe} < 0.5 \times 10^{14}$ cm^{-3} [63]).

4.5.2 Variation of the proton bunch charge. Asymmetry of the bunch centroid displacement

We furthermore study the dependency of hosing amplitude on the proton bunch charge Q_p (or density n_{b0}), keeping other parameters constant. Theory (see Eq. 2.14 and [50]) suggests that the number of exponentiations of hosing N_h, or the growth rate, increases with n_{b0}, i.e., with Q_p. We note that n_{b0} varies less than Q_p due to the change in the transverse emittance and, hence, transverse size of the bunch at the plasma entrance σ_{r0}. We calculate n_{b0} from the proton bunch population N_b and corresponding measured σ_{r0} (for values see Section 3.2) as:

$$n_{b0} = \frac{N_b}{(2\pi)^{3/2}\sigma_{r0}^2\sigma_z}. \tag{4.4}$$

We also remind that the measurement of x_c is performed not in plasma (as in [50]), but after 3.5 m of propagation of the protons from the plasma exit to the OTR screen. Therefore the values of x_c and thus N_h that we calculate tend to overestimate those in plasma.

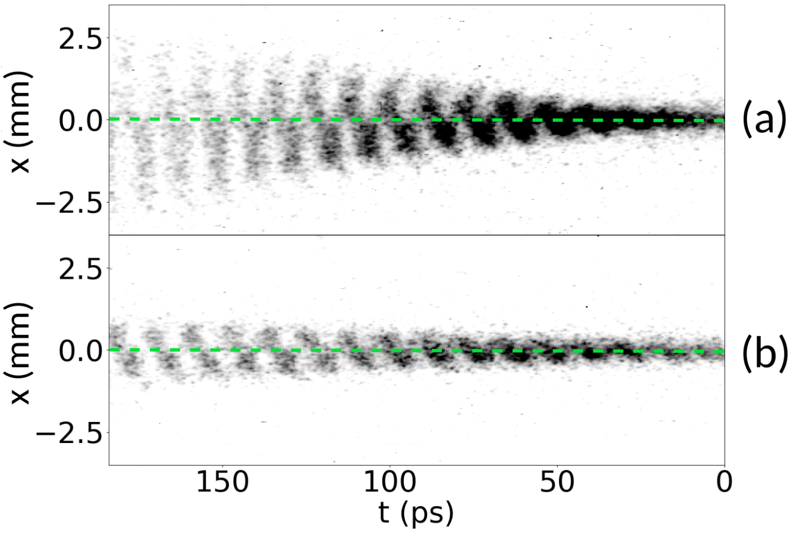

Figure 4.5.4: Averaged time-resolved images of the proton bunch charge density distribution ($\Delta x \approx 1\ c/\omega_{pe}$). (a) $Q_p = (46.5 \pm 0.6)$ nC ($n_{b0} = (7.0 \pm 0.9) \times 10^{12}$ cm^{-3}), (b) $Q_p = (14.9 \pm 0.1)$ nC ($n_{b0} = (4.3 \pm 0.2) \times 10^{12}$ cm^{-3}). Images have the same color scale. The extent of the bunch envelope oscillation is ~ 2 times higher with higher Q_p.

Averaged time-resolved images of the proton bunch charge density distribution (Fig. 4.5.4) clearly show that, with $Q_p = (46.5 \pm 0.6)$ nC, that is, $n_{b0} = (7.0 \pm 0.9) \times 10^{12}$ cm^{-3} (a), the amplitude of envelope oscillation is higher than with $Q_p = (14.9 \pm 0.1)$ nC, that is, $n_{b0} = (4.3 \pm 0.2) \times 10^{12}$ cm^{-3} (b). We note that (b) shows the same data as in Fig. 4.1.4(b), but with the vertical scale adjusted for the visual comparison with (a). For (a), $\Delta x = 0.95 \pm 0.16\ c/\omega_{pe}$, for (b) $\Delta x = 1.03 \pm 0.18\ c/\omega_{pe}$, that is, the two misalingment extent values are approximately the same.

Corresponding x_c oscillation curves show that with $Q_p \approx 46.5$ nC, the amplitude of hosing is on average 2.1 times higher (Fig. 4.5.5, red line) than with $Q_p \approx 14.9$ nC (black line).

Furthermore, with higher Q_p we observe a clear asymmetry of the x_c oscillation with respect to the bunch axis. In order to quantify this asymmetry, we integrate the area between the x_c curve and the bunch axis (0, 0) separately for $x_c < 0$ and $x_c > 0$. We

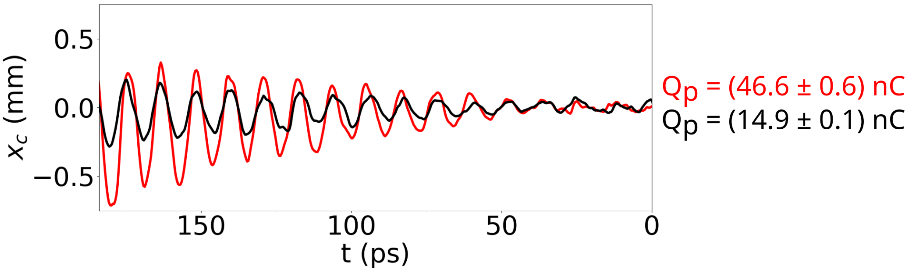

Figure 4.5.5: Proton bunch centroid position $x_c(t)$. $\Delta x \approx 1\ c/\omega_{pe}$. $Q_p = (46.5 \pm 0.6)$ nC ($n_{b0} = (7.0 \pm 0.9) \times 10^{12}$ cm^{-3}) – red line, $Q_p = (14.9 \pm 0.1)$ nC ($n_{b0} = (4.3 \pm 0.2) \times 10^{12}$ cm^{-3}) – black line.

then define the asymmetry as:

$$A_{\pm} = \frac{|A_{>0} - A_{<0}|}{A_{>0} + A_{<0}}. \tag{4.5}$$

The value of $A_{\pm} = 0$ indicates than no asymmetry is present, $A_{\pm} = 1$ – that the data is fully asymmetric (above/below the bunch axis). With $Q_p \approx 46.5$ nC, $A_{\pm} \approx 0.40$, while with $Q_p \approx 14.9$ nC, $A_{\pm} \approx 0.21$. Generally, with lower Q_p, $A_{\pm}$ is in range from 0.02 to 0.32 and remains mostly low. Reference [50] shows that coupling between hosing and SM developing simultaneously (as is the case in the experiment) generates such an asymmetry. The strength of the coupling and the resulting asymmetry depends on, e.g., initial seed amplitudes for hosing and SM. These parameters are not measured in the experiment and differ in kind (wakefields driven by the electron bunch) from the ones in the theory (initial centroid and envelope perturbations). It is therefore difficult to draw conclusions and provide comparison of the experimental data with the theoretical findings. However, the data with higher Q_p seems to reflect the effect and its trend.

4.6 Comparison of a theoretical model of hosing with experimental results

We compare theoretical predictions of a model of long-beam, early-time regime hosing [50] and experimental results. The corresponding equations from [50] for x_c (Eq. 2.13) and N_h (Eq. 2.14) and their descriptions are given in Section 2.3.2. We use these equations to determine whether the experimental results retain some characteristics of the theoretical model.

Generally, not all the assumptions used to derive Eqs 2.13 and 2.14 are verified in the experiments whose results are presented here. We check whether at least some of the key assumptions are satisfied. In the experiment, the proton bunch has an approximately Gaussian transverse and longitudinal distributions, as opposed to constant distributions in [50]. However, as mentioned in [50], N_h weakly depends on the initial transverse bunch distribution.

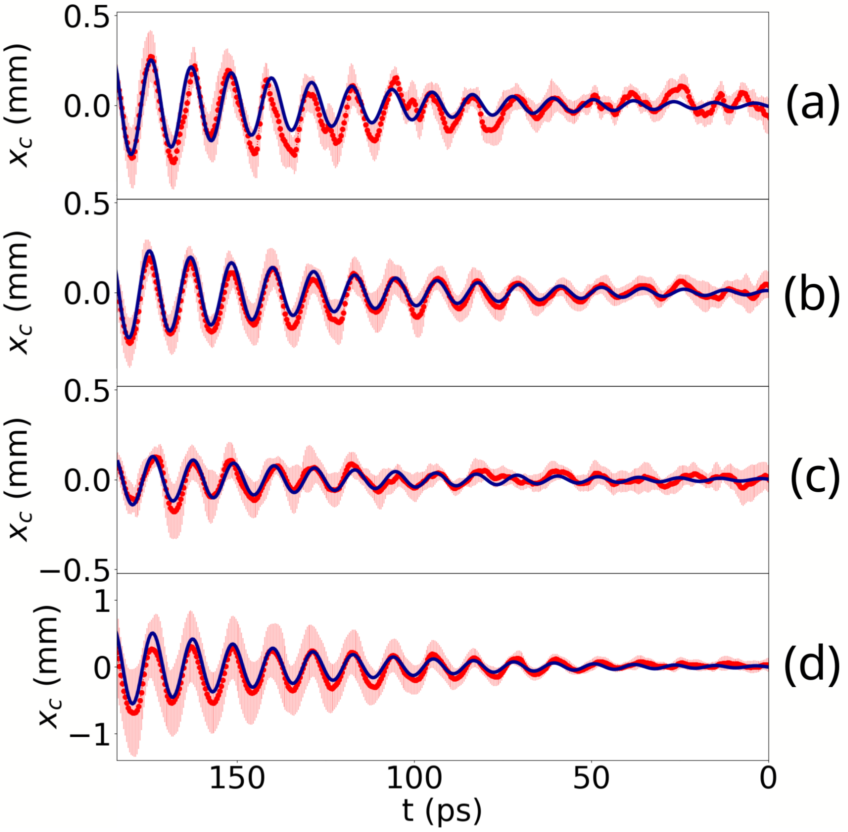

Figure 4.6.1: Centroid position $x_c(t)$ along the bunch ($n_{pe} = 0.96 \times 10^{14}$ cm^{-3}): dotted red line – average of 10 single events, red bars – rms variation of the events, solid blue line – result of the fit of Eq. (1). (a) to (c): $Q_p = (14.9 \pm 0.1)$ nC and $n_{b0} = (4.3 \pm 0.2) \times 10^{12}$ cm^{-3}. (a) $\Delta x = (0.53 \pm 0.15)\ c/\omega_{pe}$, (b) $\Delta x = (0.95 \pm 0.16)\ c/\omega_{pe}$, (c) $\Delta x = (1.47 \pm 0.16)\ c/\omega_{pe}$. (d) $Q_p = (46.5 \pm 0.6)$ nC and $n_{b0} = (7.0 \pm 0.9) \times 10^{12}$ cm^{-3}, $\Delta x = (1.03 \pm 0.18)\ c/\omega_{pe}$. Note larger vertical scale on (d) than on (a) to (c).

The effect of the plasma return current is low in the experiment, since the bunch transverse size is smaller than the plasma skin depth: $\sigma_{r0} < 0.4\ c/\omega_{pe}$ and $\mu \approx 0.91$. The ratio between the bunch and the plasma electron densities is $n_{b0}/n_{pe} \leq 0.07 \ll 1$, as in [50]. The ratio between the wavebreaking field E_{WB} and the amplitude of the initial wakefields driven by the electron bunch in similar experimental conditions is $E_{init}/E_{WB} \ll 1$ [103]. The experimental normalized propagation distance in plasma is $D = \sqrt{\frac{m_e}{m_b}\frac{n_{b0}}{n_{pe}}\frac{1}{2\gamma}}z \leq 3.9$ ($z = 10$ m), while $D \leq 1.1$ in [50]. The observation time range $t - t_0 > D/\omega_{pe}$, as in [50]. In the experiment, the induced hosing grows from the amplitude of the initial wakefields, i.e., $\delta_c = 0$ at $z = 0$. However, after a short propagation distance in plasma, the bunch acquires a x_c oscillation from the wakefields driven by the electron bunch. The experimental conditions are therefore similar to those in [50].

We perform a nonlinear least squares fit of Eq. 2.13 to the experimental x_c oscillation curves (Fig. 4.6.1, data shown in Figs 4.5.2 and 4.5.4). The initial parameters t_0 and δ_c cannot be obtained in the experiment and are therefore free parameters of the fit. The other parameters ($n_{pe}, n_{b0}, \gamma, z, \mu$) are determined from the measurements.

Figure 1	(a)	(b)	(c)	(d)
Experimental parameters				
Proton bunch charge Q_p [nC]	14.9 ± 0.1	14.9 ± 0.1	14.9 ± 0.1	46.5 ± 0.6
Misalignment extent Δx [c/ω_{pe}]	0.53 ± 0.15	0.95 ± 0.16	1.47 ± 0.16	1.03 ± 0.18
Results of the fit				
Initial x_c oscillation amplitude δ_c [μm]	12.5	11.3	6.9	11.6
Initial time t_0 [ps]	3.2	2.5	8.4	3.0
Goodness of the fit R^2	0.68	0.92	0.78	0.84
Other results				
Bunch centroid position x_c [$t \approx 163$ ps][mm]	0.198	0.173	0.108	0.306
Number of exponentiations N_h [$t \approx 163$ ps]	4.89	4.85	4.87	5.46

Table 4.6.1: Columns from left to right, for the data and the results of the fit shown in Fig. 4.6.1 ($n_{pe} = 0.96 \times 10^{14}$ cm^{-3}): experimental parameters Δx and Q_p, fit parameters δ_c and t_0 and the goodness of the fit R^2. Bunch centroid position x_c calculated at $t \approx 163$ ps and corresponding number of exponentiations N_h (using δ_c determined from the fit).

The results of the fit (δ_c, t_0) are given in Table 4.6.1. The goodness of the fit parameter R^2 for all the data is in range from 0.68 to 0.92, that is, the agreement between the model and the data is generally good, as also seen in Fig. 4.6.1.

Table 4.6.1 shows that, when varying Δx (Fig. 4.6.1(a) to (c)), δ_c decreases with increasing Δx. This is expected, as the amplitude of the initial wakefields decreases with increasing Δx (that is, with the distance from the wakefields axis [102]), in the range of Δx considered (see Section 4.5.1). Differences in the amplitude of x_c

oscillation in Fig. 4.6.1(a) to (c) are due to the change in δ_c, since N_h in these three cases is essentially the same. When increasing Q_p and keeping $\Delta x \approx 1\ c/\omega_{pe}$ (Fig. 4.6.1(d), $Q_p \approx 46.5$ nC, and Fig. 4.6.1(b), $Q_p \approx 14.9$ nC), δ_c does not vary significantly (Table 4.6.1). This is consistent with the amplitude of the initial wakefields driven by the electron bunch being independent of Q_p. The increase in Q_p, and therefore n_{b0}, leads to the increase in N_h (Eq. 2.14, see also Section 4.5.2). Therefore the amplitude of x_c oscillation starting from the same δ_c is higher for the data shown in Fig. 4.6.1(d) with $Q_p \approx 46.5$ nC than for the one in Fig. 4.6.1(b) with $Q_p \approx 14.9$ nC.

Overall, the ratio between δ_c and the transverse bunch size at the plasma entrance r_{b0} is $\delta_c/\sigma_{r0} \leq 0.06$. The linear regime approximation thus remains valid for the experimental results. Fit results indicate that the values of t_0 do not vary significantly (< 6 ps or $< 1/f_{pe} \approx 11$ ps) in these measurements.

The growth of the amplitude of hosing is determined from the maximum experimental value of x_c oscillation at $t \approx 163$ ps and δ_c obtained from the results of the fit. It is $x_c[t \approx 163\ \text{ps}]/\delta_c \approx 26.3$ with $Q_p \approx 46.5$ nC, close to the growth of the transverse wakefield amplitude that was shown in [104] for similar experimental conditions in case of SM. This goes along with the theoretical predictions for hosing and SM to have similar growth rates (e.g., [50]). The N_h values (at $t \approx 163$ ps) for all the data presented are shown in the last row of Table 4.6.1. The typical value of N_h is around 5.

Overall, we conclude that the experimental data retains the main characteristics of the theoretical model of Ref. [50] for the development of hosing, though quantitative comparison remains difficult.

Chapter 5

Conclusions and outlook

In this thesis, we have shown for the first time that hosing of a long, relativistic proton bunch propagating in an over-dense plasma can be induced and thus observed in a reproducible way. Hosing is induced by relative misalignment between the trajectory of a short electron bunch, hence the wakefields it drives, and that of the following proton bunch. In this configuration, hosing develops simultaneously with self-modulation (SM), in perpendicular planes. Hosing manifests itself as an oscillation of the proton bunch centroid position that, due to its resonant coupling to the wakefields, grows along the bunch and plasma. The centroid position in case of SM has no periodic pattern and remains close to the bunch propagation axis. With no electron bunch, SM develops as an instability and no hosing is observed, indicating that the seed wakefields indeed induce hosing. We observe hosing and SM developing simultaneously with the two streak cameras that yield time-resolved images in the perpendicular planes. Additionally, we introduce a method to reconstruct the time-resolved 3D proton bunch charge density distribution. With this method, we are indeed able to reproduce the two perpendicular planes of the bunch and, thus, to clearly observe the two processes of interest. The electron bunch drives wakefields at the plasma electron frequency f_{pe}, therefore the frequency of hosing f_H is close to that of SM, f_{SM}, both close to f_{pe}, measured at two plasma densities, $n_{pe} = 0.96 \times 10^{14}$ cm^{-3} ($f_{pe} = (87.99 \pm 0.18)$ GHz) and $n_{pe} = 2.03 \times 10^{14}$ cm^{-3} ($f_{pe} = (127.80 \pm 0.26)$ GHz). The development of hosing depends on the direction of misalignment, that is, when the direction is reverted (e.g.,$+x \rightarrow -x$), the centroid position oscillation is reflected with respect to the bunch propagation axis. The amplitude of hosing decreases with increasing misalignment extent Δx, for $\Delta x > 0.5\ c/\omega_{pe}$ (c/ω_{pe} – cold plasma skin depth). When $\Delta x > 2.5\ c/\omega_{pe}$, SM develops as an instability and no hosing is observed. When not induced by a sufficient level of seed wakefields, hosing was only observed as an instability, at low plasma densities $n_{pe} \approx 0.5 \times 10^{14}$ cm^{-3}. The amplitude of hosing increases with the proton bunch charge Q_p (fixed Δx), as predicted by theoretical findings. We find good general agreement between the experimental data and a theoretical model of long-beam, early-time regime hosing [50], despite certain differences between the assumptions of the model and experimental conditions. Overall, the measurements, whose results are described in this thesis, represent the most comprehensive characterization of hosing in the context of plasma-based acceleration.

The study presented here took place at the AWAKE experiment at CERN. The ultimate goal of this experiment is to become an accelerator that provides electron bunches with tens of GeV of energy, with focus on particle physics applications. This requires the proton bunch to drive wakefields for a long distance (tens or hundreds of meters) and the accelerated witness bunch to have sufficiently high quality. Oscillation of the proton bunch centroid position, i.e. hosing, significantly alters the distribution of the bunch and the structure of the wakefields. That may result in a decrease in acceleration length and in appearance of an on-axis deflecting force, leading to scattering or loss of the witness bunch. Therefore, if it developed, hosing would have to be mitigated. We note that, when not induced, hosing was not observed at plasma densities higher than $n_{pe} \approx 0.5 \times 10^{14}$ cm^{-3}. Seeding SM with the relativistic ionization front was shown to strongly suppress hosing. When the electron bunch is used for seeding, hosing is observed (as shown in this thesis) at the plasma densities of up to $n_{pe} = 2.03 \times 10^{14}$ cm^{-3}, and may be induced at even higher densities, reaching that of operation. If the electron bunch seeding scheme is chosen for the future accelerator, studies on the tolerances in alignment have to be done, optimal electron bunch parameters have to be found and the conditions for stable operation have to be determined. The development of hosing will be studied with the new Rubidium vapor source that allows for imposing a plasma density step, that was shown (with numerical simulations) to suppress hosing [60]. Lastly, as an instability, hosing can develop not only at f_{pe}, but at any frequency (or wavelength λ_{pe}). Long-wavelength hosing was not consistently observed in the experiments, however, limited data, as well as simulation results have already shown this effect. It might be therefore interesting to investigate whether this type of hosing develops, especially in the longer plasmas.

Bibliography

[1] H. Wiedemann, Particle accelerator physics (Springer Cham, 2015).

[2] R. Van de Graaff, “A 1,500,000 volt electrostatic generator”, Phys. Rev. **38**, 1919 (1931).

[3] J. D. Cockcroft, E. T. S. Walton, and E. Rutherford, “Experiments with high velocity positive ions.—(i) further developments in the method of obtaining high velocity positive ions”, Proc. R. Soc. Lond. A **136**, 619–630 (1932).

[4] S. Myers, The LEP Collider, from design to approval and commissioning, John Adams’ memorial lecture, Delivered at CERN, 26 Nov 1990 (CERN, Geneva, 1991).

[5] O. S. Brüning, P. Collier, P. Lebrun, S. Myers, R. Ostojic, J. Poole, and P. Proudlock, LHC Design Report, CERN Yellow Reports: Monographs (CERN, Geneva, 2004).

[6] ATLAS Collaboration, “Observation of a new particle in the search for the standard model higgs boson with the atlas detector at the lhc”, Physics Letters B **716**, 1–29 (2012).

[7] J. T. Seeman, “The Stanford linear collider”, AIP Conference Proceedings **249**, 2035–2081 (1992).

[8] P. Lebrun et al., The CLIC programme: Towards a staged e^+e^- linear collider exploring the terascale: CLIC conceptual design report, CERN Yellow Reports: Monographs (CERN, Geneva, 2012).

[9] M. Benedikt et al., Future Circular Collider – European Strategy Update Documents, tech. rep. (CERN, Geneva, 2019).

[10] R. W. Assmann and J. Grebenyuk, “Accelerator physics challenges towards a plasma accelerator with usable beam quality”, Proceedings of the 5th Int. Particle Accelerator Conf. (IPAC’14), 961–964 (2014).

[11] J. M. Dawson, “Nonlinear electron oscillations in a cold plasma”, Phys. Rev. **113**, 383–387 (1959).

[12] P. Muggli, Beam driven systems, Lecture at the CERN Accelerator School on Plasma Wake Acceleration, 2014.

[13] S. Lee, T. Katsouleas, R. Hemker, and W. B. Mori, "Simulations of a meter-long plasma wakefield accelerator", Phys. Rev. E **61**, 7014–7021 (2000).

[14] E. Esarey, C. B. Schroeder, and W. P. Leemans, "Physics of laser-driven plasma-based electron accelerators", Rev. Mod. Phys. **81**, 1229–1285 (2009).

[15] T. Tajima and J. M. Dawson, "Laser electron accelerator", Phys. Rev. Lett. **43**, 267–270 (1979).

[16] Y. Kitagawa et al., "Beat-wave excitation of plasma wave and observation of accelerated electrons", Phys. Rev. Lett. **68**, 48–51 (1992).

[17] F. Amiranoff et al., "Observation of modulational instability in nd-laser beat-wave experiments", Phys. Rev. Lett. **68**, 3710–3713 (1992).

[18] C. E. Clayton, K. A. Marsh, A. Dyson, M. Everett, A. Lal, W. P. Leemans, R. Williams, and C. Joshi, "Ultrahigh-gradient acceleration of injected electrons by laser-excited relativistic electron plasma waves", Phys. Rev. Lett. **70**, 37–40 (1993).

[19] D. Strickland and G. Mourou, "Compression of amplified chirped optical pulses", Optics Communications **55**, 447–449 (1985).

[20] A. Modena et al., "Electron acceleration from the breaking of relativistic plasma waves", Nature **377**, 606–608 (1995).

[21] J. Faure et al., "A laser–plasma accelerator producing monoenergetic electron beams", en, Nature **431**, 541–544 (2004).

[22] C. G. R. Geddes et al., "High-quality electron beams from a laser wakefield accelerator using plasma-channel guiding", en, Nature **431**, 538–541 (2004).

[23] S. P. D. Mangles et al., "Monoenergetic beams of relativistic electrons from intense laser–plasma interactions", Nature **431**, 535–538 (2004).

[24] R. Weingartner et al., "Ultralow emittance electron beams from a laser-wakefield accelerator", Phys. Rev. ST Accel. Beams **15**, 111302 (2012).

[25] W. P. Leemans et al., "Multi-gev electron beams from capillary-discharge-guided subpetawatt laser pulses in the self-trapping regime", Phys. Rev. Lett. **113**, 245002 (2014).

[26] A. J. Gonsalves et al., "Petawatt laser guiding and electron beam acceleration to 8 gev in a laser-heated capillary discharge waveguide", **122**, 084801 (2019).

[27] S. Steinke et al., “Staging of laser-plasma accelerators”, Physics of Plasmas **23**, 056705 (2016).

[28] H.-P. Schlenvoigt et al., “A compact synchrotron radiation source driven by a laser-plasma wakefield accelerator”, en, Nature Physics **4**, 130–133 (2008).

[29] M. Fuchs et al., “Laser-driven soft-X-ray undulator source”, en, Nature Physics **5**, 826–829 (2009).

[30] A. R. Maier et al., “Water-Window X-Ray Pulses from a Laser-Plasma Driven Undulator”, en, Scientific Reports **10**, 5634 (2020).

[31] D. Margarone et al., “Elimaia: a laser-driven ion accelerator for multidisciplinary applications”, Quantum Beam Science **2**, `10.3390/qubs2020008` (2018).

[32] D. Doria, M. Cernaianu, P. Ghenuche, D. Stutman, K. Tanaka, C. Ticos, and C. Ur, “Overview of ELI-NP status and laser commissioning experiments with 1 PW and 10 PW class-lasers”, Journal of Instrumentation **15**, C09053 (2020).

[33] Y. Pfaff et al., “Nonlinear pulse compression of a 200 mJ and 1 kW ultrafast thin-disk amplifier”, Opt. Express **31**, 22740–22756 (2023).

[34] P. Chen, J. M. Dawson, R. W. Huff, and T. Katsouleas, “Acceleration of electrons by the interaction of a bunched electron beam with a plasma”, Phys. Rev. Lett. **54**, 693–696 (1985).

[35] J. B. Rosenzweig et al., “Experimental observation of plasma wake-field acceleration”, Phys. Rev. Lett. **61**, 98–101 (1988).

[36] I. Blumenfeld et al., “Energy doubling of 42 GeV electrons in a metre-scale plasma wakefield accelerator”, Nature **445**, 741–744 (2007).

[37] V. Shpakov et al., “First emittance measurement of the beam-driven plasma wakefield accelerated electron beam”, Phys. Rev. Accel. Beams **24**, 051301 (2021).

[38] M. Litos et al., “High-efficiency acceleration of an electron beam in a plasma wakefield accelerator”, en, Nature **515**, 92–95 (2014).

[39] S. Zhou, J. Hua, W. An, W. B. Mori, C. Joshi, J. Gao, and W. Lu, “High efficiency uniform wakefield acceleration of a positron beam using stable asymmetric mode in a hollow channel plasma”, Phys. Rev. Lett. **127**, 174801 (2021).

[40] C. A. Lindstrøm, “Staging of plasma-wakefield accelerators”, Phys. Rev. Accel. Beams **24**, 014801 (2021).

[41] A. Caldwell, K. Lotov, A. Pukhov, and F. Simon, "Proton-driven plasma-wakefield acceleration", en, Nature Physics **5**, 363–367 (2009).

[42] A. Caldwell and K. V. Lotov, "Plasma wakefield acceleration with a modulated proton bunch", Physics of Plasmas **18**, 103101 (2011).

[43] AWAKE Collaboration, "Acceleration of electrons in the plasma wakefield of a proton bunch", Nature **571**, 363–367 (2018).

[44] F. Batsch et al. (AWAKE Collaboration), "Transition between Instability and Seeded Self-Modulation of a Relativistic Particle Bunch in Plasma", Phys. Rev. Lett. **126**, 164802 (2021).

[45] L. Verra et al. (AWAKE Collaboration), "Controlled growth of the self-modulation of a relativistic proton bunch in plasma", Phys. Rev. Lett. **129**, 024802 (2022).

[46] D. H. Whittum, W. M. Sharp, S. S. Yu, M. Lampe, and G. Joyce, "Electron-hose instability in the ion-focused regime", Phys. Rev. Lett. **67**, 991–994 (1991).

[47] R. M. Kulsrud, J. W. K. Mark, and A. Caruso, "The hose-pipe instability in stellar systems", en, Astrophysics and Space Science **14**, 52–55 (1971).

[48] O. Bromberg, C. B. Singh, J. Davelaar, and A. A. Philippov, "Kink instability: evolution and energy dissipation in relativistic force-free nonrotating jets", The Astrophysical Journal **884**, 39 (2019).

[49] J. Davelaar, A. A. Philippov, O. Bromberg, and C. B. Singh, "Particle acceleration in kink-unstable jets", The Astrophysical Journal Letters **896**, L31 (2020).

[50] C. B. Schroeder, C. Benedetti, E. Esarey, F. J. Grüner, and W. P. Leemans, "Coupled beam hose and self-modulation instabilities in overdense plasma", Phys. Rev. E **86**, 026402 (2012).

[51] E. P. Lee, "Resistive hose instability of a beam with the Bennett profile", Phys. Fluids **21**, 1327–1343 (1978).

[52] K. J. O'Brien, "Theory of ion-hose instability", J. Appl. Phys. **65**, 9–16 (1989).

[53] D. H. Whittum, "Transverse two-stream instability of a beam with a Bennett profile", Phys. Plasmas **4**, 1154–1159 (1997).

[54] P. Sprangle, J. Krall, and E. Esarey, "Hose-modulation instability of laser pulses in plasmas", Phys. Rev. Lett. **73**, 3544–3547 (1994).

[55] G. Shvets and J. S. Wurtele, "Instabilities of short-pulse laser propagation through plasma channels", Phys. Rev. Lett. **73**, 3540–3543 (1994).

[56] C. Huang, W. Lu, M. Zhou, C. E. Clayton, C. Joshi, W. B. Mori, et al., "Hosing instability in the blow-out regime for plasma-wakefield acceleration", Phys. Rev. Lett. **99**, 255001 (2007).

[57] J. Vieira, W. B. Mori, and P. Muggli, "Hosing instability suppression in self-modulated plasma wakefields", Phys. Rev. Lett. **112**, 205001 (2014).

[58] T. J. Mehrling, C. Benedetti, C. B. Schroeder, E. Esarey, and W. P. Leemans, "Suppression of beam hosing in plasma accelerators with ion motion", Phys. Rev. Lett. **121**, 264802 (2018).

[59] G. Loisch, M. Gross, C. Koschitzki, O. Lishilin, A. M. de la Ossa, J. Osterhoff, and F. Stephan, "Towards experimental investigation of hosing instability mitigation at the PITZ facility", J. Phys.: Conf. Ser. **1596**, 012003 (2020).

[60] M. Moreira, P. Muggli, and J. Vieira, "Mitigation of the onset of hosing in the linear regime through plasma frequency detuning", Phys. Rev. Lett. **130**, 115001 (2023).

[61] M. C. Kaluza et al., "Observation of a long-wavelength hosing modulation of a high-intensity laser pulse in underdense plasma", Phys. Rev. Lett. **105**, 095003 (2010).

[62] A. Del Dotto et al., "Experimental observation of the transition between hose and self-modulation instability regimes", Phys. Plasmas **29**, 100701 (2022).

[63] M. J. Hüther, "Direct Observation of the Hosing Instability of a Long Relativistic Proton Bunch in the AWAKE Experiment", PhD Thesis (Technical University Munich, 2020).

[64] F. F. Chen, Introduction to Plasma Physics and Controlled Fusion (Springer International Publishing, Cham, 2016).

[65] R. Keinigs and M. E. Jones, "Two-dimensional dynamics of the plasma wakefield accelerator", The Physics of Fluids **30**, 252–263 (1987).

[66] Y. Fang, "Resonant excitation of plasma wakefield", PhD Thesis (University of Southern California, 2020).

[67] W. Lu, C. Huang, M. M. Zhou, W. B. Mori, and T. Katsouleas, "Limits of linear plasma wakefield theory for electron or positron beams", Physics of Plasmas **12**, 063101 (2005).

[68] C. B. Schroeder, C. Benedetti, E. Esarey, F. J. Grüner, and W. P. Leemans, "Growth and phase velocity of self-modulated beam-driven plasma waves", Phys. Rev. Lett. **107**, 145002 (2011).

[69] L. Verra et al., "Development of the self-modulation instability of a relativistic proton bunch in plasma", Physics of Plasmas **30**, 083104 (2023).

[70] J. Vieira, W. B. Mori, and P. Muggli, "Hosing instability suppression in self-modulated plasma wakefields", Phys. Rev. Lett. **112**, 205001 (2014).

[71] R. Lee and M. Lampe, "Electromagnetic instabilities, filamentation, and focusing of relativistic electron beams", Phys. Rev. Lett. **31**, 1390–1393 (1973).

[72] B. Allen, V. Yakimenko, M. Babzien, M. Fedurin, K. Kusche, and P. Muggli, "Experimental study of current filamentation instability", Phys. Rev. Lett. **109**, 185007 (2012).

[73] M. Honda, J. Meyer-ter-Vehn, and A. Pukhov, "Collective stopping and ion heating in relativistic-electron-beam transport for fast ignition", Phys. Rev. Lett. **85**, 2128–2131 (2000).

[74] Y. Sentoku, K. Mima, P. Kaw, and K. Nishikawa, "Anomalous resistivity resulting from mev-electron transport in overdense plasma", Phys. Rev. Lett. **90**, 155001 (2003).

[75] A. R. Bell, "The acceleration of cosmic rays in shock fronts – I", Monthly Notices of the Royal Astronomical Society **182**, 147–156 (1978).

[76] T. Piran, "The physics of gamma-ray bursts", Rev. Mod. Phys. **76**, 1143–1210 (2005).

[77] A. Bohdan et al., "Magnetic field amplification by the Weibel instability at planetary and astrophysical shocks with high mach number", Phys. Rev. Lett. **126**, 095101 (2021).

[78] L. Verra et al., Current filamentation instability of a relativistic proton bunch in plasma, in preparation.

[79] A. Caldwell, E. Gschwendtner, K. Lotov, P. Muggli, and M. Wing, "AWAKE design report: a proton-driven plasma wakefield acceleration experiment at CERN", Technical Report CERN-SPSC-2013-013 (2013).

[80] F. Batsch, "Setup and characteristics of a timing reference signal with sub-ps accuracy for AWAKE", J. Phys.: Conf. Ser. **1596**, 012006 (2020).

[81] AWAKE Collaboration, “Experimental observation of proton bunch modulation in a plasma at varying plasma densities”, Phys. Rev. Lett. **122**, 054802 (2019).

[82] F. Braunmüller et al. (AWAKE Collaboration), “Proton bunch self-modulation in plasma with density gradient”, Phys. Rev. Lett. **125**, 264801 (2020).

[83] The CERN accelerator complex, layout in 2022, `https://cds.cern.ch/record/2800984/?ln=en`, CERN-GRAPHICS-2022-001.

[84] AWAKE Laser, `https://edms.cern.ch/ui/file/1506630/1.0/AWK-TO-ES-0001-10-00.pdf`, AWK-TO-ES-0001.

[85] E. Öz and P. Muggli, “A novel Rb vapor plasma source for plasma wakefield accelerators”, Nucl. Instrum. Meth. A **740**, Proceedings of the first European Advanced Accelerator Concepts Workshop 2013, 197–202 (2014).

[86] E. Öz, F. Batsch, and P. Muggli, “An accurate Rb density measurement method for a plasma wakefield accelerator experiment using a novel Rb reservoir”, Nucl. Instr. and Meth. in Phys. Res. A **829**, 2nd European Advanced Accelerator Concepts Workshop - EAAC 2015, 321–325 (2016).

[87] F. Batsch, M. Martyanov, E. Öz, J. Moody, E. Gschwendtner, A. Caldwell, and P. Muggli, “Interferometer-based high-accuracy white light measurement of neutral rubidium density and gradient at AWAKE”, Nucl. Instr. and Meth. in Phys. Res. A **909**, 3rd European Advanced Accelerator Concepts workshop (EAAC2017), 359–363 (2018).

[88] V. Ginsburg and I. Frank, “Radiation from a uniformly moving electron passing from one medium to another”, Journ. of Exp. and Theor. Phys. (JETP) **16**, 836–844 (1946).

[89] J. Jackson, Classical Electrodynamics (Wiley, 1999).

[90] Hamamatsu photonics K.K. Guide to streak cameras, `https://www.hamamatsu.com/resources/pdf/sys/SHSS0006E_STREAK.pdf`, 2008.

[91] Hamamatsu streak camera test report, `https://cernbox.cern.ch/s/hlWguTmP2dDPBnj`, 2017.

[92] P. Muggli et al. (AWAKE Collaboration), “Physics to plan AWAKE Run 2”, J. Phys.: Conf. Ser. **1596**, 012008 (2020).

[93] A. Caldwell et al. (AWAKE Collaboration), “Path to AWAKE: Evolution of the concept”, Nucl. Instrum. Methods Phys. Res., Sect. A **829**, 2nd European Advanced Accelerator Concepts Workshop - EAAC 2015, 3–16 (2016).

[94] E. Gschwendtner et al., "The AWAKE run 2 programme and beyond", Symmetry **14**, `10.3390/sym14081680` (2022).

[95] E. Gschwendtner et al. (NA64 Collaboration), AWAKE++: The AWAKE Acceleration Scheme for New Particle Physics Experiments at CERN, tech. rep. (CERN, Geneva, 2018).

[96] A. Caldwell and M. Wing, "VHEeP: a very high energy electron–proton collider", en, The European Physical Journal C **76**, 463 (2016).

[97] T. Nechaeva, L. Verra, G. Zevi Della Porta, and P. Muggli, "A method for obtaining 3d charge density distribution of a self-modulated proton bunch", J. Phys.: Conf. Ser. **2420**, 012063 (2023).

[98] Mayavi: 3D scientific data visualization and plotting in Python, `https://docs.enthought.com/mayavi/mayavi/`.

[99] P. I. Morales Guzmán et al. (AWAKE Collaboration), "Simulation and experimental study of proton bunch self-modulation in plasma with linear density gradients", Phys. Rev. Accel. Beams **24**, 101301 (2021).

[100] M. X. Cohen, "A better way to define and describe Morlet wavelets for time-frequency analysis", NeuroImage **199**, 81–86 (2019).

[101] M. S. Tiscareno and M. M. Hedman, "A review of Morlet wavelet analysis of radial profiles of Saturn's rings", Philos. Trans. Royal Soc. A **376**, 20180046 (2018).

[102] K.-J. Moon, P. Muggli, and M. Chung, "Dominance of the tightly-focused electron seed bunch over the long proton bunch modulation in an over-dense plasma", in Proceedings of the Advanced Accelerator Concepts Workshop, (unpublished) (Nov. 2022).

[103] K.-J. Moon and M. Chung, "Determination of the phase of wakefields driven by a self-modulated proton bunch in plasma", in Proceedings of the IPAC'21, international particle accelerator conference, TUPAB138, 10.18429/JACoW-IPAC2021-TUPAB138 (2021).

[104] M. Turner et al. (AWAKE Collaboration), "Experimental observation of plasma wakefield growth driven by the seeded self-modulation of a proton bunch", Phys. Rev. Lett. **122**, 054801 (2019).

[105] C. Amoedo et al., Proton beam self-modulation instability in a DC discharge plasma source at AWAKE, in preparation.

Acknowledgments

Working in such a large-scale complex facility is never a one-person job. This thesis would not have been possible without the contributions of many people, from AWAKE and all around Max-Planck-Institute for Physics and CERN. I would like to express my particular gratitude to

Dr. Patric Muggli, my day-to-day advisor, for the trust and many opportunities, for being always available and willing to talk, for the support and a lot of patience, for guiding me through my PhD path.

Prof. Dr. Allen Caldwell, my supervisor, for the kindness, trust and support.

Jan Pucek, for being around since my first days in the experiment and greatly facilitating the start of my tunnel life at AWAKE, for being always kind, attentive and giving a helping hand. Also, for being the part of our conference dream-team!

Dr. Lucas Ranc, for the gentleness, endless discussions and hours in the laser room, being there, sharing lots of knowledge and passion about many topics, and for everything beyond work.

Dr. Pablo Morales Guzmán, for keeping a great company in Munich and at the conferences, for understanding, willingness to listen to all my stories and sharing the experiences. And for opening a whole new world of good coffee!

Dr. John Farmer, for the constructive discussions, as well as for the brilliant sense of humor and organizing many informal meetups to have some good time off-work together.

Dr. Eugenio Senes, for helping with all kinds of technical aspects and for being an empathetic listener.

Last, but not least, I would like to thank my family and friends, for their unconditional support and presence, for their eagerness to understand, for their trust and positivity.

Appendices

Appendix A

Observation of hosing at low plasma density in the DC discharge plasma source

As was mentioned previously, in order for AWAKE to become an accelerator facility, its setup has to be upgraded. In particular, to inject the witness bunch into the fully developed wakefields and to increase acceleration length, another plasma source, where acceleration would take place, is needed. Multiple options for such a plasma source are considered. One of them is a direct current (DC) discharge plasma source, where the gas is ionized with an electric arc discharge. The plasma electron density is adjusted by varying the delay between the discharge current and the time of arrival of the proton bunch. An advantage of this source is that the resulting plasma column has a relatively large transverse size, ~ 20 mm, as opposed to ~ 2 mm in case of the laser-created plasma, that is, no issue of alignment between the plasma column and the proton bunch is expected. However, when it comes to having plasmas tens of meters-long, building a single-stage discharge plasma source is technologically challenging. Having several stages stacked together might be thus needed.

The discharge plasma source was installed and tested at AWAKE. The development of hosing, SM and current filamentation instability (CFI) were studied in a single-stage 10 m-long source, filled with either Helium, Argon or Xenon, at various plasma electron densities n_{pe}.

We show the observation of hosing at $n_{pe} < 0.5 \times 10^{14}$ cm^{-3}. We expect hosing to develop as an instability, since in this experiment, unlike elsewhere in the thesis, no seed wakefields can be purposely introduced. Hosing thus starts from the possible irregularities or asymmetry in the bunch centroid position or charge distributions. Hosing might develop along with SM or without it. We expect the growth of hosing to be low, since, as was shown in [50], its growth rate decreases with n_{pe}. Helium at the pressure of 45 Pa and the discharge current of 500 A are used for the plasma. The proton bunch has an elliptical transverse shape, with $\sigma_x = 340$ μm and $\sigma_y = 140$ μm, and a charge of $Q_p = (43.4 \pm 0.7)$ nC. We note that the x-plane and the y-plane, mentioned when describing time-resolved images, are referred to the planes of the streak camera coordinate system (and not the beam coordinate system). Time t = 0 is $\sim 1.5\sigma_t$ ahead of the proton bunch longitudinal center and is the same for all the data presented.

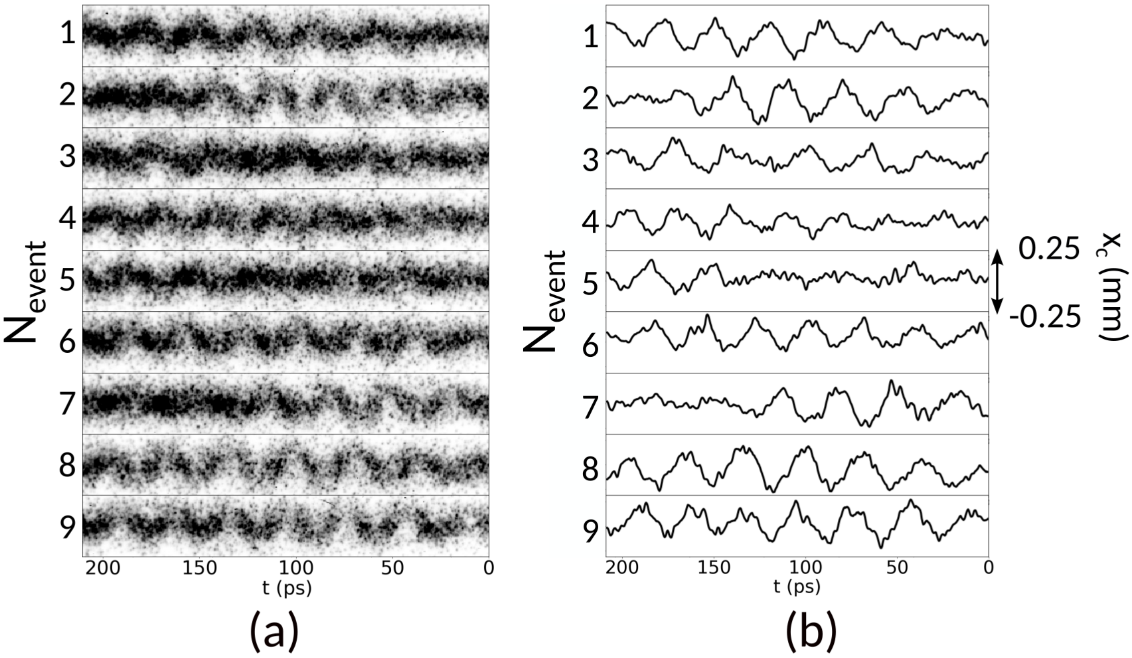

Figure A.0.1: (a) Single-event time-resolved images of the proton bunch charge density distribution in the x-plane. Images have the same color scale. (b) Bunch centroid position x_c corresponding to the events in (a). The vertical axis scale is the same for all the events, with values in range (-0.25, 0.25) mm. The maximum x_c oscillation amplitude in this dataset is ~ 0.23 mm. No significant growth of hosing along the bunch is observed, and in the second and seventh event the x_c oscillation stops after t = 150 ps.

We show the single-event time-resolved images of the proton bunch charge density

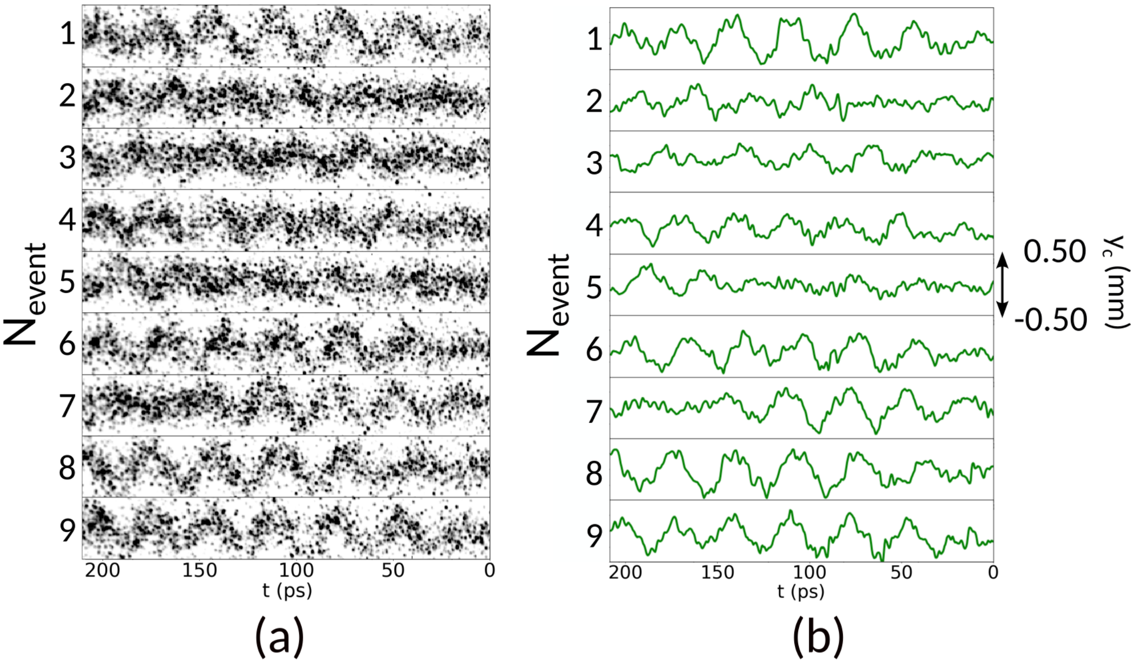

Figure A.0.2: (a) Single-event time-resolved images of the proton bunch charge density distribution in the y-plane, obtained simultaneously with those in Fig. A.0.1. Images have the same color scale. (b) Bunch centroid position y_c corresponding to the events in (a). The vertical axis scale is the same for all the events, with values in range (-0.5, 0.5) mm. The maximum y_c oscillation amplitude in this dataset is $\sim$ 0.49 mm. The amplitude of oscillation is higher than in Fig. A.0.1 due to the plane of the elongation of the proton bunch being closer (within $\sim 28°$) to this plane of the streak camera coordinate system. No significant growth of hosing along the bunch is observed.

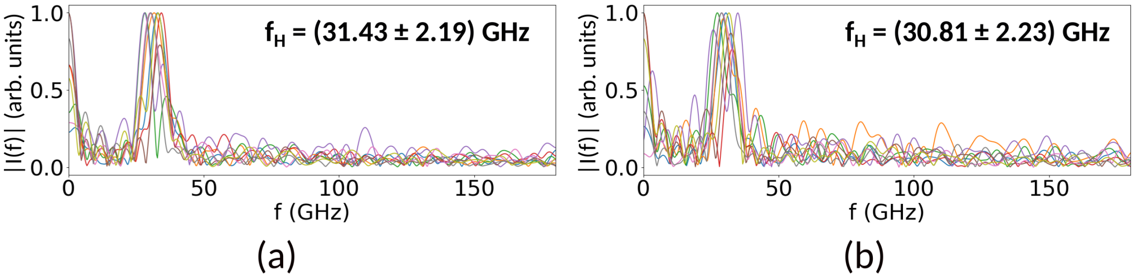

Figure A.0.3: DFT power spectra of the events in Figs A.0.1 (a, x-plane) and A.0.2 (b, y-plane). The average frequency with corresponding rms variation is $f_H = (31.43 \pm 2.19)$ GHz (a) and $f_H = (30.81 \pm 2.23)$ GHz.

distribution, obtained simultaneously in the perpendicular planes of the streak camera coordinate system in Figs A.0.1 (a, x-plane) and A.0.2 (a, y-plane). Corresponding centroid positions x_c and y_c are displayed in Figs A.0.1 (b, x-plane) and A.0.2 (b, y-plane). These figures clearly show some of the characteristics of hosing. As expected, hosing develops as an instability, that is, the process is not reproducible from event to event. Hosing is observed in the two planes, with no SM visible, possibly indicating that no wakefields are present, and the centroid position of the bunch couples to the global focusing force appearing when the bunch enters the plasma and attracts the plasma electrons to its axis. As the growth rate N_h decreases with the plasma electron density n_{pe} [50], we observe no significant growth of the centroid position oscillation along the bunch, and in, e.g., seventh event the oscillation stops after t $=$ 150 ps. However, the oscillation develops along the plasma. The maximum centroid position oscillation amplitude is $x_{c,max} \sim 0.23$ mm in x-plane, and $x_{c,max} \sim 0.49$ mm in y-plane. We note that the x-plane of the streak camera coordinate system is at an angle of 62° with respect to the (longer) x-axis of the proton bunch, therefore the centroid position oscillation has lower amplitude in this plane, as the amplitude is lower along the shorter bunch axis. We estimate the growth of hosing along the bunch with a ratio between the $x_{c,max}$ and the centroid position at t $= 0$, $x_{c,0}$. This ratio is $2 < x_{c,max}/x_{c,0} < 7$ for the events in Figs A.0.1 and A.0.2 and is quite low, compared to, e.g., ~ 26.3 in Section 4.6 (with $n_{pe} = 0.96 \times 10^{14}$ cm^{-3}).

We perform the DFT of the x_c and y_c oscillations as was done in Section 4.4.1. The obtained power spectra for each event are shown in Fig. A.0.3. We find $f_H = 31.43 \pm 2.19$ GHz for x_c and $f_H = (30.81 \pm 2.23)$ GHz for y_c, the two frequencies being essentially the same, as these are the same events captured in perpendicular planes. Measurement of the SM frequency at the same n_{pe} yields $f_{SM} = 31.08 \pm 2.20$ GHz. Therefore, $f_H \approx f_{SM}$ and thus $f_H \approx f_{pe}$. This does not have to be the case, since hosing develops as an instability and is not coupled to SM. However, in all the observations (at AWAKE) so far [63], the f_H is always close to f_{pe}. From the value of f_{SM}, we estimate that $n_{pe} = 0.12 \cdot 10^{14}$ cm^{-3}. The plasma electron density was additionally determined with the interferometry measurement, resulting in $n_{pe} = 0.26 \times 10^{14}$ cm^{-3} [105], that is about 2.2 times higher than the value obtained from the frequencies of SM and hosing. The setup used for the interferometry measurement is insufficient to have a more precise estimate of n_{pe} at this density range, because the phase shift is too small at low densities . We therefore use the f_{SM} as a basis for the n_{pe} determination and for comparison with f_H, since SM can only develop at f_{pe}, and f_{SM} agrees with the interferometry measurements in the range where the precision of these measurements is sufficiently high [105].

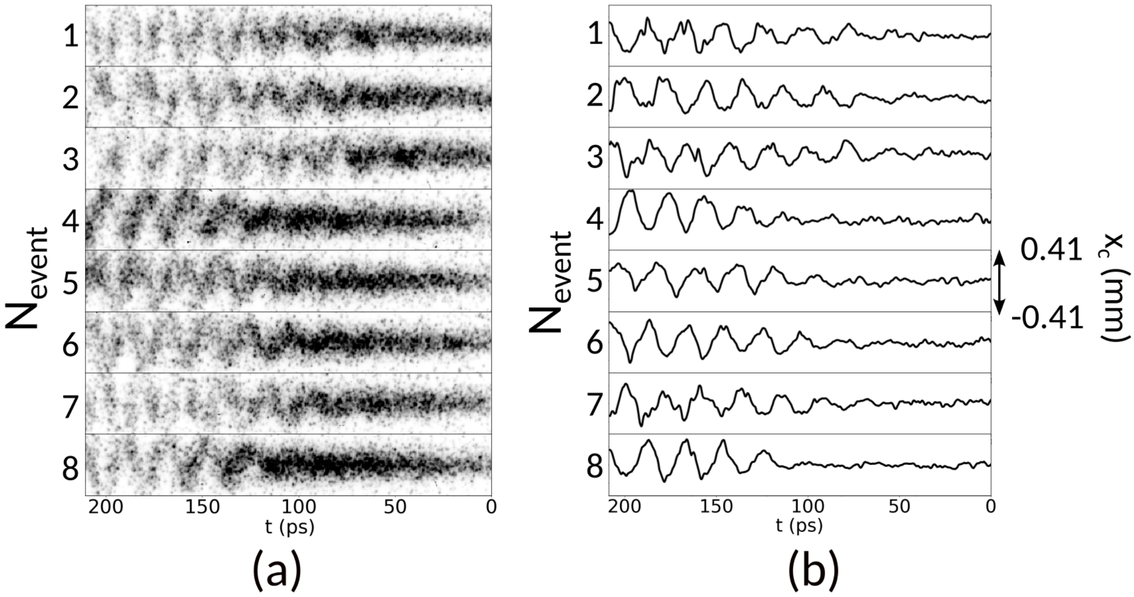

Figure A.0.4: (a) Single-event time-resolved images of the proton bunch charge density distribution in the x-plane. Images have the same color scale. (b) Bunch centroid position x_c corresponding to the events in (a). The vertical axis scale is the same for all the events, with values in range (-0.41, 0.41) mm. The maximum x_c oscillation amplitude in this dataset is ~ 0.39 mm. Growth of hosing along the bunch is clearly observed and the amplitude of x_c oscillation is higher than in Fig. A.0.1, as n_{pe} is higher.

We show that with higher $n_{pe} = 0.26 \times 10^{14}$ cm^{-3} (determined from the corresponding f_{SM} measurement), the bunch is more focused close to its head ($t < 50$ ps, Fig. A.0.4, x-plane) than with lower n_{pe} (Fig. A.0.1) and the growth of hosing along the bunch is clearly visible on the images and corresponding centroid position oscillation curves (Fig. A.0.4). The maximum amplitude of oscillation is ~ 1.7 times higher than in Fig. A.0.1 and is ~ 0.39 mm. Albeit the growth along the bunch is less evident in the y-plane (Fig. A.0.5(b)), the maximum amplitude of the y_c oscillation is ~ 1.2 times higher than in Fig. A.0.2 and is ~ 0.59 mm. The overall larger growth of hosing also corresponds to the lower intensity of the signal on the images (Fig. A.0.5(a)). The estimate of growth along the bunch is $4 < x_{c,max}/x_{c,0} < 15$, that is, higher than with the lower n_{pe}.

The DFT power spectra of the events in Figs A.0.4 and A.0.5 are shown in Fig. A.0.6. The f_H, determined in both planes, are approximately the same, and are

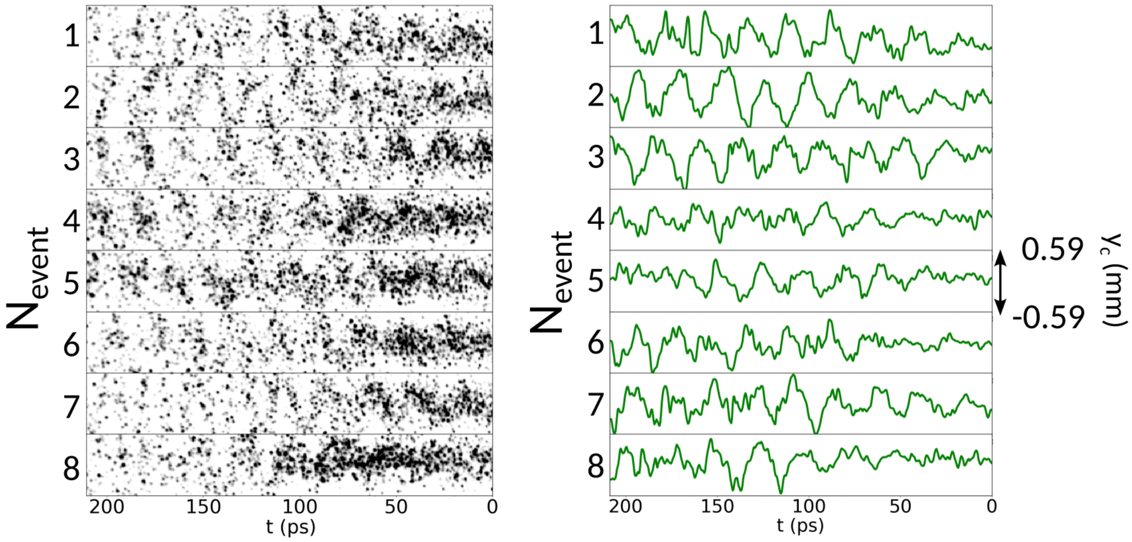

(a) (b)

Figure A.0.5: (a) Single-event time-resolved images of the proton bunch charge density distribution in the y-plane, obtained simultaneously with those in Fig. A.0.4. Images have the same color scale. (b) Bunch centroid position y_c corresponding to the events in (a). The vertical axis scale is the same for all the events, with values in range (-0.59, 0.59) mm. The maximum y_c oscillation amplitude in this dataset is ~ 0.59 mm. The growth along the bunch is pronounced less than in Fig. A.0.4, but the y_c oscillation amplitude is higher than in Fig. A.0.2.

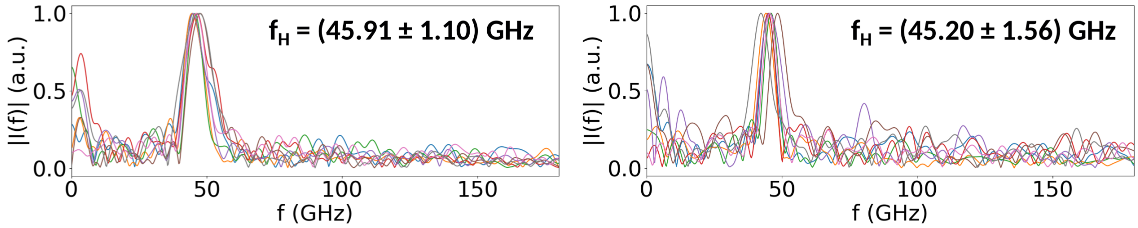

(a) (b)

Figure A.0.6: DFT power spectra of the events in Figs A.0.4 (a, x-plane) and A.0.5 (b, y-plane). The average frequency with corresponding rms variation is $f_H = (45.91 \pm 1.10)$ GHz (a) and $f_H = (45.20 \pm 1.56)$ GHz.

$f_H = (45.91 \pm 1.10)$ GHz and $f_H = (45.20 \pm 1.56)$ GHz. The SM frequency is $f_{SM} = 45.53 \pm 1.38$ GHz, therefore, $f_H \approx f_{SM}$, as is the case with the lower n_{pe}.

Overall, we conclude that hosing is observed at low plasma electron densities $n_{pe} < 0.5 \times 10^{14}$ cm^{-3}, and it develops as an instability. Moreover, it is unambiguously observed in two perpendicular planes, that is, we observe pure hosing, rather than the one coupled to SM. This also means that the growth of this process might be due to the coupling of the bunch centroid position to the global focusing force in plasma. The growth of the centroid position oscillation along the bunch is either not visible (at the lowest plasma electron density) or is pronounced, but still low, as expected from theory. The frequency of hosing is close to that of SM, and, therefore, to that of the plasma electrons, that is, hosing we observe is λ_{pe}-hosing, as might be expected from growth rate determination [60]. These results also highlight the fact that inducing hosing with the electron bunch, as presented in the main text, allowed for better measurements of hosing and for determination of many of its expected characteristics, as opposed to mere observation of the bunch centroid position oscillation.

Appendix B

List of publications

T. Nechaeva, L. Verra, J. Pucek, L. Ranc, M. Bergamaschi, G. Zevi Della Porta and P. Muggli (AWAKE Collaboration), "Hosing of a long relativistic particle bunch in plasma", *accepted in Phys. Rev. Lett.*, arXiv:2309.03785 (2024).

L. Verra, S. Wyler, **T. Nechaeva**, J. Pucek, V. Bencini, M. Bergamaschi, L. Ranc, G. Zevi Della Porta, E. Gschwendtner, P. Muggli (AWAKE Collaboration), “Development of the self-modulation instability of a relativistic proton bunch in plasma”, *Physics of Plasmas* **30** 083104 (2023).

T. Nechaeva, L. Verra, G. Zevi Della Porta and P. Muggli, "A method for obtaining 3D charge density distribution of a self-modulated proton bunch", *J. Phys.: Conf. Ser.* **2420** 012063 (2023).

T. Nechaeva and P. Muggli, "Hosing of a long proton bunch induced by an electron bunch", *Proceedings of the 48th EPS Conference on Plasma Physics* **O2.201** (2022).

L. Verra G. Zevi Della Porta, J. Pucek, **T. Nechaeva**, S. Wyler, M. Bergamaschi, E. Senes, E. Guran, J.T. Moody, M.A. Kedves, E. Gschwendtner, and P. Muggli (AWAKE Collaboration), “Controlled Growth of the Self-Modulation of a Relativistic Proton Bunch in Plasma”, *Phys. Rev. Lett.* **129** 024802 (2022).

F. Braunmüller, **T. Nechaeva** et al. (AWAKE Collaboration), “Proton bunch self-modulation in plasma with density gradient”, *Phys. Rev. Lett.* **125** 264801 (2020).

Glossary

arb. units	arbitrary units	
AWAKE	Advanced Wakefield Experiment	
$A_\pm$	asymmetry of the bunch centroid position oscillation	
BBU	beam breakup instability	
BPM	beam position monitor	
BTV	beam television	
c	speed of light in vacuum	$c = 2.998 \cdot 10^8$ m/s
CERN	European Organization for Nuclear Research	
CFI	current filamentation instability	
CLIC	Compact Linear Collider	
CMOS	complementary metal-oxide-semiconductor	
CPA	chirped pulse amplification	
Cs_2Te	Caesium telluride	
CWT	continuous wavelet transform	
D	normalized propagation distance in plasma	
DC	direct current	
δ_c	initial bunch centroid position displacement	
ΔE_S	energy loss of the particle per turn in a synchrotron	
δr	initial bunch radius perturbation	
Δx	electron-proton beams misalignment extent	
DFT	discrete Fourier transform	
e	electron charge	$e = 1.602 \cdot 10^{-19}$ C
ELI	Extreme Light Infrastructure	
ϵ_0	vacuum permittivity	$\epsilon_0 = 8.85 \cdot 10^{-12}$As/Vm

E_{WB}	wavebreaking field	
FCC	Future Circular Collider	
FEL	free electron laser	
f_H	frequency of hosing	
f_{pe}	plasma electron frequency	
f_{SM}	frequency of self-modulation	
FWHM	full width at half maximum	
γ	Lorentz factor of a particle	
I	intensity of the signal	
I_0	zeroth order modified Bessel function of the first kind	
I_1	first order modified Bessel function of the first kind	
I_2	second order modified Bessel function of the first kind	
k_{pe}	plasma electron wavenumber	
K	Boltzmann constant	$K = 1.380 \cdot 10^{-23}$ J/K
K_0	zeroth order modified Bessel function of the second kind	
K_1	first order modified Bessel function of the second kind	
K_2	second order modified Bessel function of the second kind	
λ_D	Debye length	
λ_{pe}	plasma electron wavelength	
LBNL	Lawrence Berkley National Laboratory	
LEP	Large Electron-Positron Collider	
LHC	Large Hadron Collider	
Linac	linear accelerator	
LWFA	laser wakefield acceleration	
m_b	particle mass	
MCP	micro-channel plate	
m_e	electron mass	$m_e = 9.109 \cdot 10^{-31}$ kg
MTF	modulation transfer function	

μ	term describing effect of plasma return current for hosing
m_0	rest mass of a particle
n_b	bunch density distribution
n_{b0}	initial bunch density
n_{pe}	plasma electron density
N_b	bunch population
N_D	number of particles inside the Debye sphere
Nd:YAG	Neodymium-doped Yttrium Aluminium Garnet
N_h	number of exponentiations of hosing
N_{SM}	number of exponentiations of self-modulation
ν	term describing effect of plasma return current for self-modulation
ω_{pe}	plasma electron angular frequency
OTR	optical transition radiation
PS	Proton Synchrotron
PSB	Proton Synchrotron Booster
PWFA	particle-driven wakefield acceleration
QCD	quantum chromodynamics
QED	quantum electrodynamics
Q_p	proton bunch charge
r	radial coordinate
r_c	region of interest for bunch centroid position determination
r_m	region of interest for bunch longitudinal density profile determination
rms	root mean square
R	radial wakefield component
Rb	Rubidium
$R\&D$	research and development
RIF	relativistic ionization front
ROI	region of interest
r_S	synchrotron radius
σ_{Gauss}	spatial resolution

σ_r	transverse bunch size
σ_{r0}	transverse bunch size at the plasma entrance
$\sigma_{r,OTR}$	transverse bunch size at the OTR screen
σ_t	longitudinal bunch size in the units of time
σ_x	transverse bunch size in x-plane
σ_y	transverse bunch size in y-plane
σ_z	longitudinal bunch size
SHG	second harmonic generation
SLAC	Stanford Linear Accelerator Center
SLC	Stanford Linear Collider
SM	self-modulation
SPS	Super Proton Synchrotron
t	time in the laboratory frame
τ_c	collision period in plasma
τ_{pe}	plasma electron period
t_0	initial time
Θ	Heaviside step function
THG	third harmonic generation
Ti:Sa	Titanium Sapphire
T_{pe}	plasma electron temperature
UV	ultraviolet
W_r	radial wakefield
W_z	longitudinal wakefield
x_{ax}	bunch propagation axis
x_c	bunch centroid position
x_{w}	wakefield centroid position
ζ	bunch co-moving coordinate
z	position along the plasma
3D	three-dimensional

List of Figures

List of Tables